



Title	Observational Study on the Central Subparsec-Scale Structure of Active Galactic Nucleus with Very Long Baseline Interferometer
Author(s)	日浦, 皓一朗
Citation	北海道大学. 博士(理学) 甲第12237号
Issue Date	2016-03-24
DOI	10.14943/doctoral.k12237
Doc URL	http://hdl.handle.net/2115/61697
Type	theses (doctoral)
File Information	Koichiro_Hiura.pdf



[Instructions for use](#)

博士学位論文

Observational Study on the Central Subparsec-Scale Structure of
Active Galactic Nucleus with Very Long Baseline Interferometer

(超長基線干渉計による活動銀河核の
中心サブパーセクスケールの構造に関する観測的研究)

日浦 皓一郎

北海道大学大学院理学院
宇宙理学専攻

平成28年3月

Abstract

Galaxies are fundamental elements of the universe, and consist of stars, gas, dark matter and supermassive black holes (SMBHs). It is important to understand galaxy formation and evolution when clarifying the evolution of universe. It is believed that stars are monotonically formed from gas in galaxies, and that galaxies evolve. However, from recent researches on galaxy formation and evolution, it is suggested that feedback effect that constrains star formation is a key process of galaxy evolution. One of important feedback effects is feedback from active galactic nucleus (AGN).

AGN is a bright source at broad wavelength bands from radio to γ -ray in the galactic center. Typical size of AGN is 10^{-3} less than that of the host galaxy, but AGN shines as brightly as the whole galaxy. This huge energy is come from gravitational energy released by mass accretion onto SMBH residing in the innermost region of AGN. The enormous released energy forms structures such as accretion disk, obscuring torus and jet in the center of AGN. Jets in radio-loud AGNs are relativistic plasma flow, and the size of jet is comparable to that of host galaxy, sometimes beyond host galaxy. Thus, jets play an important role in releasing energy of host galaxy.

Radio galaxies are misaligned radio-loud AGNs, and ideal sources to explore general properties of jets since the misalignment of the jet axis with the line of sight provides a detailed view of the structure in the jet. Radio galaxies have compact radio source, radio core, in the central region, and relatively collimated radio jets extend from radio core. At the edge of jets, shock wave regions called hotspots are formed, and radio lobes extend beyond hotspots. Generally, these structures can be seen beyond 1,000 pc from the galactic center, and a big problem is how such relatively collimated and large structures can be formed and evolved. Observationally, it is known that radio-loud AGNs make up about 10% of the whole AGNs, and most of AGNs do not have radio jets. There is a problem why a part of galaxies show such phenomena. It is necessary to unveil the physics of the vicinity of jet nozzle in order to understand the formation process of radio jet. This jet base can be spatially resolved by very long baseline interferometer (VLBI) in the radio band.

Against this background, I tried to unveil the subparsec-scale radio jet of the radio galaxy 3C 84/NGC 1275 by monitoring time variability of radio jet with the VLBI Exploration of Radio Astrometry (VERA) array. Radio galaxy 3C 84 shows intermittent jet activity, and the radio brightness has increased since 2005. Thus, 3C 84 is one of the best source to study jet properties. Using VERA, Nagai et al. (2010) found that this

activity was ascribed to the central subparsec-scale core, accompanying the ejection of a new bright component. According to the Very Long Baseline Array (VLBA) observation at 43 GHz, Suzuki et al. (2012) found that the new bright component had emerged from a radio core before 2005, and traveled southward following a parabolic trajectory on the celestial sphere. In this study, I present the detailed kinematics of new bright component to reveal its true nature. I investigate kinematics of new bright component in detail from 2007 to 2013 by monitoring the subsequent motion for non-linear trajectory found by Suzuki et al. (2012).

One of results is the apparent speed of new bright component relative to the radio core is almost constant and sub-relativistic ($0.27 \pm 0.02c$) from 2007 October to 2013 December. This property suggests that new bright component may be the head of mini-radio lobe including hotspots, rather than a relativistic knotty component formed as internal shock in underlying continuous jet flow. This result implies that the radio lobe in radio-loud AGNs might be already formed in subparsec-scale jets in the vicinity of SMBHs.

Another result is that new bright component might follow a helical path with a period of about five years thanks to highly-frequent observations. Although I cannot reliably identify the origin causing the wobbling motion because of the insufficient time span of our dataset and the lack of the information of absolute reference position, the motion might reflect the accretion disk precession induced by a spinning SMBH. In order to obtain the robust result, we continue to monitor the subparsec-scale jet of 3C 84 with high resolution phase-referencing VLBI.

As mentioned above, I found that hotspots in radio lobes in radio galaxies might be already formed in subparsec-scale jets close to the central SMBHs. I also found that hotspots in radio lobe may be precessed by a spinning SMBH. These results are achieved by unprecedented highly-frequent observations. It is important that the fact that hotspots might be formed in subparsec-scale jets near the central SMBH can constrains the physical state such as density and velocity in jet base when understanding the formation and evolution of hotspots. Those findings will contribute to constructing more sophisticated theoretical models in the future.

Contents

1	Introduction	7
1.1	Active Galactic Nucleus	7
1.1.1	AGN Zoology	7
1.1.2	Properties of Jets, Lobes and Hotspots	11
1.1.3	Dynamics of Relativistic Jets	14
1.1.4	Formation and Evolution of Radio Sources	18
1.2	Aim of the Dissertation	26
1.3	Review of 3C 84	26
2	Observation and Data Reduction	35
2.1	The VERA observation at 22 GHz	35
2.2	Data calibration and imaging	39
2.3	Gaussian Model Fitting	45
2.4	Positional Accuracy	45
3	Results	53
3.1	Total Intensity Image	53
3.2	Change in Relative Positions of Components	60
3.3	Periodicity Analysis on Wobbling Motion of C3	61
4	Discussion	71
4.1	Why is the Velocity of C3 Remarkably Slow in the Relativistic Jet?	71
4.2	Possible Origin of the Periodic Motion of C3	74
5	Conclusion	81

1

Introduction

1.1 Active Galactic Nucleus

In the universe, it is known that there are various types of galaxies. Galaxies are fundamental elements of the universe, and composed of stars, gas, dark matter and super-massive black holes (SMBHs). It needs to understand galaxy formation and evolution when unveiling the evolution of universe. It is believed that stars are monotonically formed from gas in galaxies, and that galaxies evolve. From recent researches on galaxy formation and evolution, however, it is suggested that feedback effect that constrains star formation is a key process of galaxy evolution. One of important feedback effects is feedback from active galactic nucleus (AGN).

AGN is a bright source at broad wavelength bands from radio to γ -ray in the galactic center in spite of far distance (\sim Gpc). Typical size of AGN is 10^{-3} less than that of the host galaxy, but the luminosity of AGN is comparable to that of a whole galaxy. Nowadays, it is known that AGNs harbor SMBHs of $\sim 10^6 - 10^9 M_{\odot}$ ($1 M_{\odot} = 2.0 \times 10^{33}$ g) in the innermost regions of AGNs. The huge energy is come from gravitational energy released by mass accretion onto SMBH, and the gravity of SMBHs forms various structures such as accretion disk, torus and jet in the central regions of AGNs (see Figure 1.1). Jets in radio-loud AGNs are relativistic plasma flow, and the size of jet is comparable to that of host galaxy, sometimes beyond host galaxy. Thus, jets play an important role in releasing energy of host galaxy, and heat intragalactic gas and prevent star formation. The presence of these structures is proposed or confirmed from theoretical and observational studies (see Figure 1.2).

1.1.1 AGN Zoology

AGNs are classified as various types according to differences of discovery methods. Depending on a ratio of radio luminosity at 5 GHz $L_{5\text{GHz}}$ to optical B-band luminosity L_B , they are divided broadly into two categories; radio-loud AGNs and radio-quiet AGNs (Kellermann et al., 1989). Conventionally, the criterion is $L_{5\text{GHz}}/L_B \approx 10$, and about 15–20% of AGNs are radio-loud AGNs. Difference of radio loudness is thought to arise

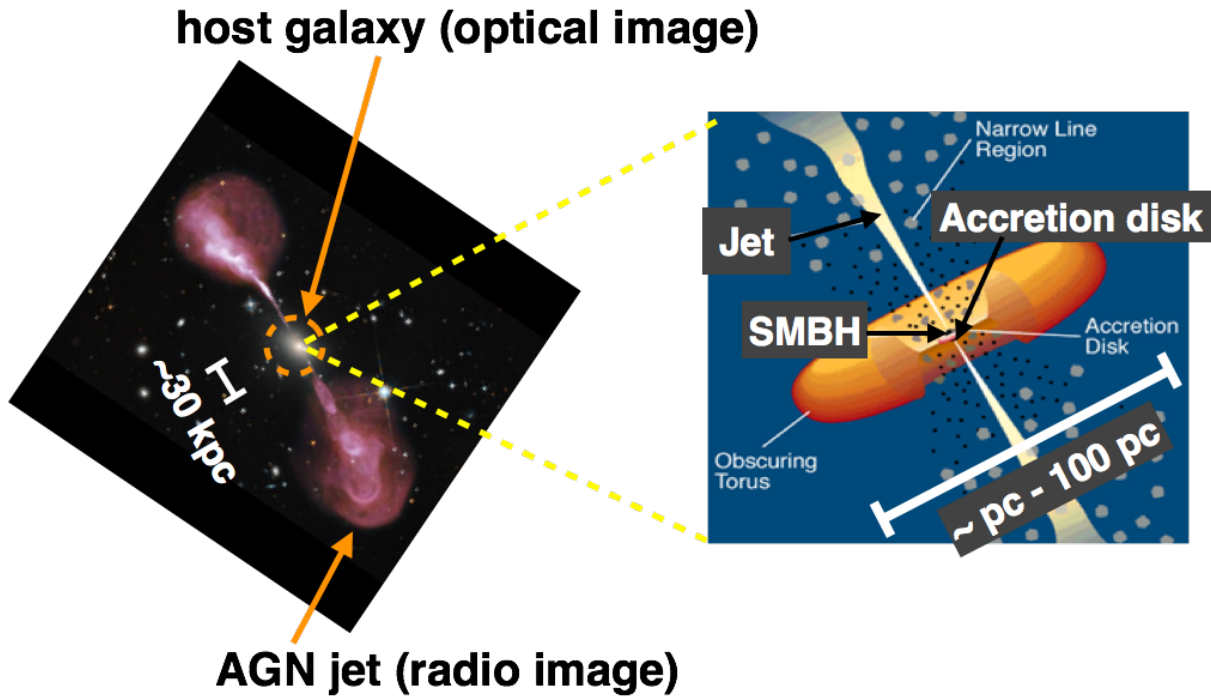


Figure 1.1. Left: An example of AGN jets in radio galaxy Hercules A (3C 348). This image is a composite between optical data from the Hubble Space Telescope (HST) (yellow) and radio data from the VLA at 4–9 GHz band (red). Its host elliptical galaxy is seen at the center in optical data, and AGN jets can be seen toward top left and bottom right from the center of the image in radio data. The galaxy is roughly 10^3 times more massive than our galaxy and harbors a $2.5 \times 10^9 M_{\odot}$ central black hole that is 10^3 times more massive than the black hole in our galaxy. Credit: NASA, ESA, S. Baum and C. O’Dea (RIT), R. Perley and W. Cotton (NRAO/AUI/NSF), and the Hubble Heritage Team (STScI/AURA) (http://www.nasa.gov/mission_pages/hubble/science/hercules-a.html) Right: A schematic view of the unified model of AGN from Urry and Padovani (1995). Typical size of dusty absorbing torus are indicated. In detail, see also Figure 1.2.

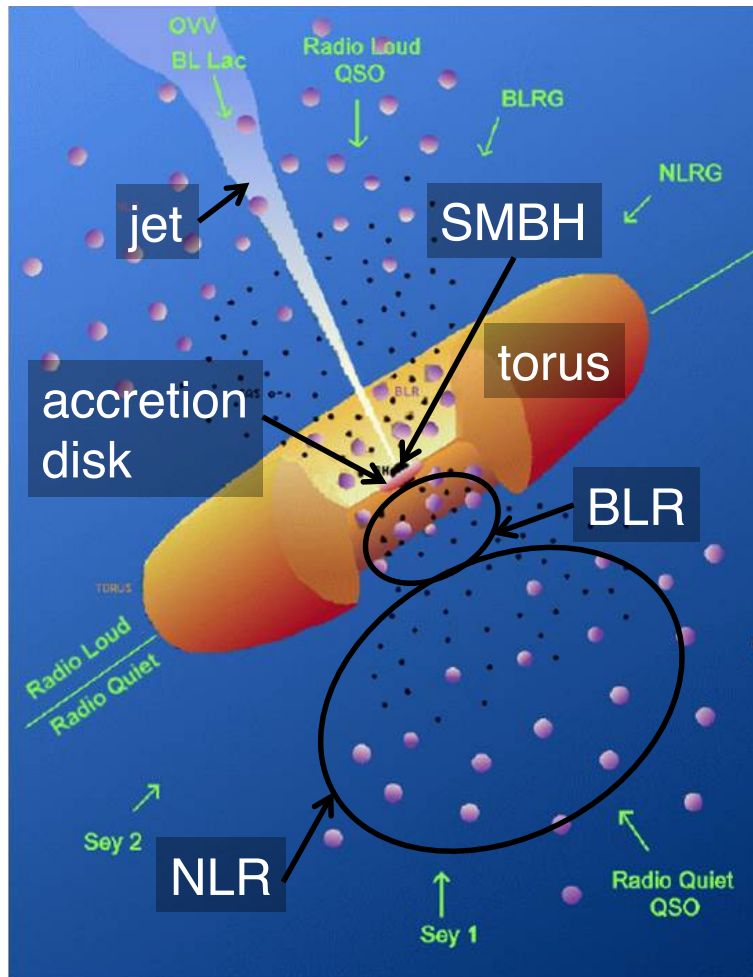


Figure 1.2. A schematic view of the unified model of AGNs from Urry and Padovani (1995). Upper (lower) half of the picture represents the model for radio loud (quiet) AGN. SMBH is located in the central region of AGN, surrounded by accretion disk. For radio loud AGN, jet is ejected perpendicular to accretion disk. Accretion disk is surrounded by broad-line region (BLR) and dusty absorbing torus supplying with gas. Narrow-line region (NLR) extends beyond torus. According to differences of viewing angles to AGN, there are a variety of AGNs apparently.

from the presence of jet. A variety of observational properties of AGNs can be largely explained by the unified model of AGN (Antonucci, 1993; Urry and Padovani, 1995) (see Figure 1.2). The unified model tells us that the apparently various observational properties is due to differences of viewing angles toward AGNs.

Radio-quiet AGN

Generally, radio-quiet AGNs are categorized as Seyfert galaxies, and most of their host galaxies are spiral galaxies. Seyfert galaxies are lower-luminosity AGNs, with B-band magnitude of $M_B > -21.5 + 5 \log h_0$, where h_0 is the Hubble constant in units of $100 \text{ km s}^{-1} \text{ Mpc}^{-1}$ (Schmidt and Green, 1983). According to their properties in optical and ultraviolet (UV) wavelength bands, they are classified into the following two categories.

- Type 1 Seyfert galaxy (Sy1): This class of AGN shows strong continuum emission from far-infrared (FIR) to X-ray, and has emission lines of broad linewidth of $\sim 1,000 \text{ km s}^{-1}$.
- Type 2 Seyfert galaxy (Sy2): This class of AGN shows relatively weak continuum emission, and has emission lines of narrow linewidth of $\sim 100 \text{ km s}^{-1}$.

Osterbrock (1981) introduced type 1.5, type 1.8 and type 1.9 between Sy1 and Sy2. These types of Seyfert galaxies are based on optical spectra, and classified from type 1.5 to type 1.9 according to observability of broad-line region (BLR) (see Figure 1.2). Generally, Seyfert galaxies are categorized into radio-quiet AGNs, but it is known that there are radio-loud Seyfert galaxies showing γ -ray emission (Abdo et al., 2009b).

Radio-loud AGN

- Fanaroff-Riley type 1 radio galaxy (FR1): The morphology of this class of AGN often shows ‘compact’ (spatially unresolved) and ‘extended’ (spatially resolved) structures (see Figure 1.3). Radio emission from these structures mainly arises from synchrotron radiation, but spectral properties of them are different. Generally, a pair of extended structures called radio lobes can be seen and, they are symmetrical with reference to the compact structure called radio core. The extent of radio lobes is sometimes comparable to $\sim \text{Mpc}$. A main difference between radio lobes and cores is that radio lobes are optically thin with respect to synchrotron radiation emitted by themselves, but radio cores are not necessarily optically thin.
- Fanaroff-Riley type 2 radio galaxy (FR2): This class of AGN is radio-brighter than FR1. The morphology of FR2 often exhibits well-collimated structures called jets in addition to radio cores and lobes (see Figure 1.4). Radio jets are emanating from the central radio core and connected to extended lobes.

They often show bending or wiggling structures. Only an approaching jet is often observed due to relativistic beaming effect as we will describe later. The brightness peak is often located at the edge of jets or radio lobes. At the edge of jets, shock wave regions called hotspots are formed, and radio lobes extend beyond hotspots. At hotspots, particle acceleration occurs due to shock wave heating, and then hotspots are bright.

Optical emission lines of FR1 and FR2 exhibit narrow linewidth. Thus, FR1 and FR2 are called narrow-line radio galaxies (NLRGs), and most of host galaxies of them are elliptical galaxies. Radio brightness distribution of FR1 becomes dimmer with distance from radio core. On the other hand, that of FR2 is limb-brightened. The criterion for dividing these classes is radio luminosity $L_{1.4\text{GHz}} = 10^{32} \text{ erg s}^{-1} \text{ Hz}^{-1}$ (Fanaroff and Riley, 1974).

- Broad-line radio galaxy (BLRG): This class of AGN shows continuum emission similar to the properties of type 1 Seyfert galaxy.
- Quasar: Quasars are brightest AGNs, with B-band magnitude of $M_B < -21.5 + 5 \log h_0$. The luminosity of the nuclei exceeds that of host galaxies. The jet of quasar often shows superluminal motion, and only an approaching jet is observed because of relativistic effects. Quasars are divided into two categories: SSRQs (steep spectrum radio quasars) with spectral index ¹ $\alpha \leq -0.5$ and FSRQs (flat spectrum radio quasars) with $\alpha \geq -0.5$. About 90% of quasars are radio-quiet quasars, and they are called QSOs.
- BL Lac objects (BL Lacs): This class of AGN shows highly-polarized and variable strong continuum emission. Some BL Lacs show continuum emission from radio to TeV γ -ray (Costamante and Ghisellini, 2002). The spectra of BL Lacs shows no strong emission and absorption lines.

Since BL Lacs and FSRQs have similarities in showing variability, high polarization and superluminal motion, they are often called blazars.

AGN zoology mentioned above is summarized in Figure 1.5. This diagram is based on unified model of AGN, and the same colored subclasses are intrinsically identical ones, different from viewing angles to them.

1.1.2 Properties of Jets, Lobes and Hotspots

It is known that radio-loud AGNs make up about 10% of the whole AGNs, and that they have relativistic jets. Material composition is not well-known, but it is considered to be electron-positron plasma as well as electron-proton plasma. When some kind of mechanism causes shock wave in jet, particle acceleration occurs and non-thermal particles with power-law energy distribution are formed. These high-energy electrons interact

¹When spectral energy distribution (SED) is expressed as $S_\nu \propto \nu^\alpha$, α is called the spectral index.

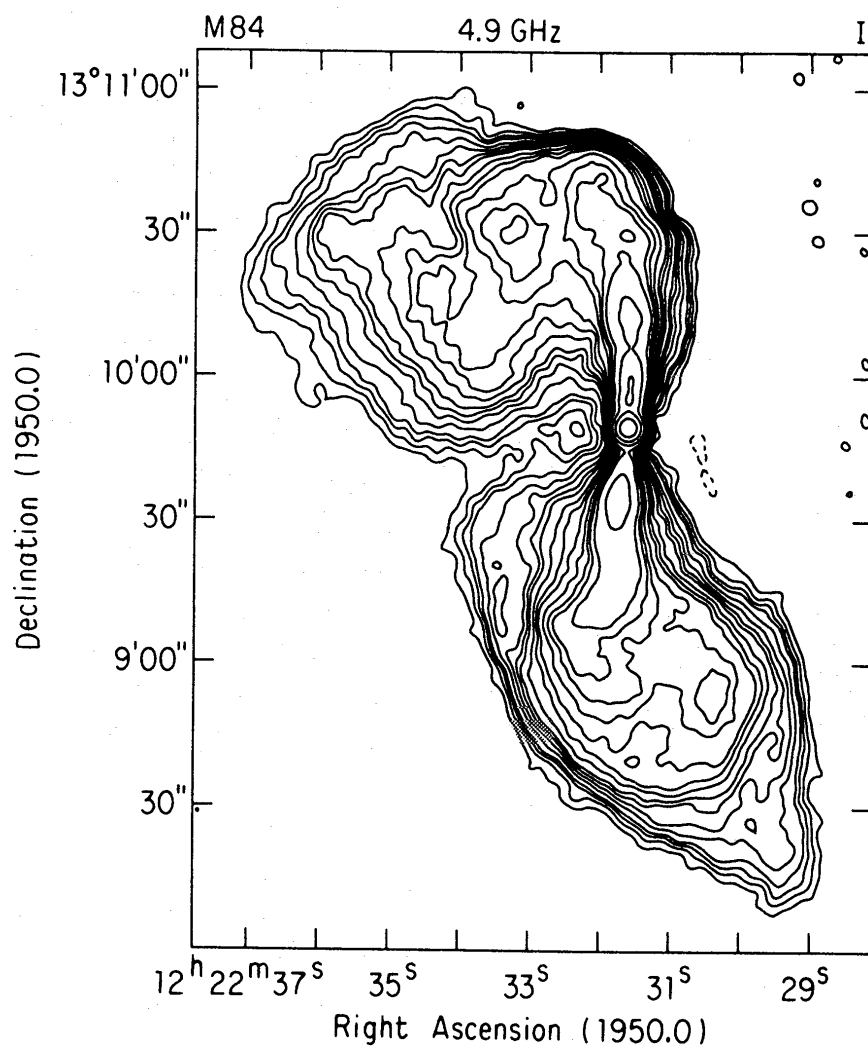


Figure 1.3. Fanaroff-Riley type 1 radio galaxy M84 ($z = 0.0034$) observed with Very Long Array (VLA) at 4.9 GHz from Laing and Bridle (1987). The brightness distribution is edge-dimming.

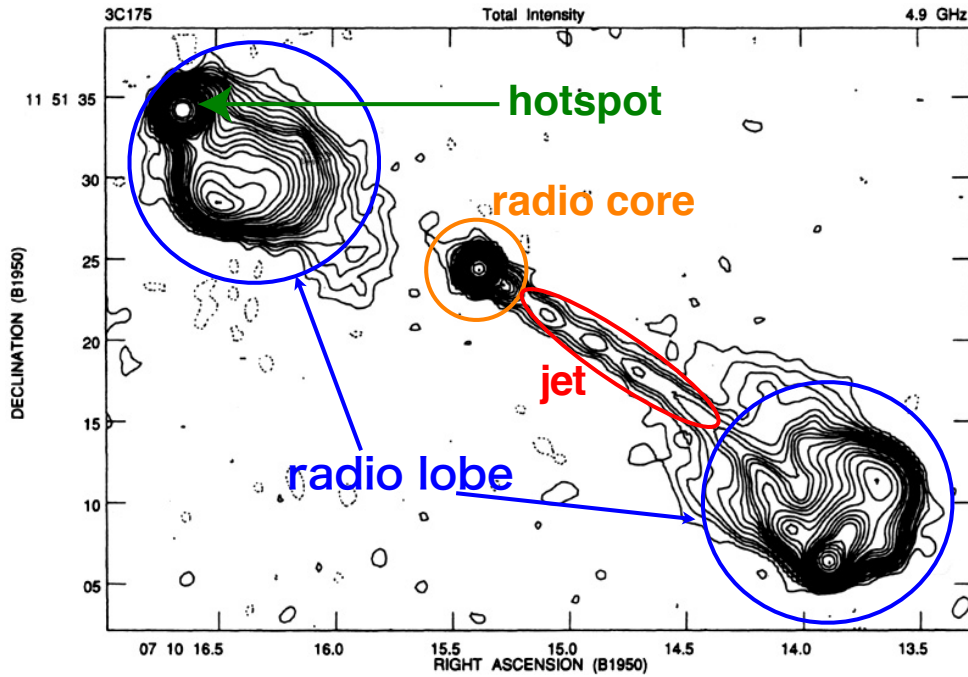


Figure 1.4. Fanaroff-Riley type 2 radio galaxy 3C 175 ($z = 0.77$) observed with VLA at 4.9 GHz from Bridle and Perley (1984). Jet structure bridges a gap between central radio core and radio lobe. Only an approaching jet can be seen due to relativistic beaming effect. The brightness distribution is edge-brightening. Hotspots are seen at the edges of radio lobes.

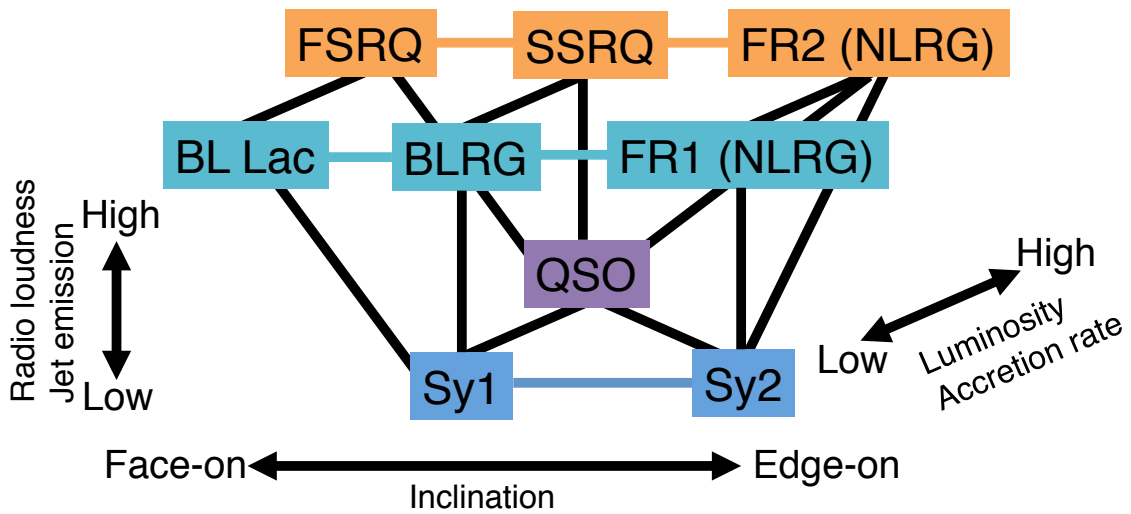


Figure 1.5. A classification diagram of AGN based on the unified model of AGNs. The same colored subclasses are intrinsically identical ones, different from viewing angles to them.

with magnetic field or photons, and then synchrotron radiation or radiation by inverse Compton scattering is emitted, respectively. Kinetic energy of relativistic jets is huge. However, jets cannot be detected in the form of electromagnetic waves unless energy is dissipated by shock wave.

Radio galaxy is believed to be misaligned radio-loud AGNs in the framework of the unified scheme of AGN shown in the previous section. Thanks to misalignment of jets, large-scale (~ 100 kpc) jet structure can be observed. When jet flow collides with dense region of intergalactic gas, electrons are accelerated and bright components called knots in jet shines in the wavelength ranges from radio to X-ray. Emission from jet knots is believed to be mainly synchrotron radiation. This indicates that electrons are accelerated to energy of 10-100 TeV.

After relativistic jets dissipate an inhomogeneous energy by ‘internal’ shock wave in the vicinity of the central engine, average flow speed still remains relativistic and propagates away. At the tip of relativistic jet, collisions with ambient medium form shock wave. This type of shock is called ‘outer’ shock wave. Interaction of jets with ambient medium differs according to the ratio between particle density of jets and that of ambient medium. When particle density of jets is relatively high, jets behave as mass points and propagate at fast speed. On the other hand, jets are decelerated strongly at the tips of jets when particle density is relatively low. Observed spherical shapes of radio lobes indicate that particle density in jets are very low. Numerical studies have confirmed that the jet is composed of lower mass density particles compared with that of the ambient medium (e.g., Norman et al., 1982).

Brighter regions called hotspots are formed at the tips of relativistic jets in radio galaxies, and they are believed to be located at the shock wave (see Figure 1.6). The speed of jet is relativistic, but that of hotspot is subrelativistic ($\sim 0.01 - 0.1c$) (e.g., Conway, 2002). At the location of shock wave, kinematic energy of relativistic jet is dissipated, and plasma in jet is heated and accelerated. Because of low density of particles in jet, shock in jet is relativistic one and plasma temperature is high. Thus, shocked particles thermally expand in a direction perpendicular to jet axis, and then shock waves are formed.

Particles in jet are confined in an egg-like region called cocoon in this manner. Pressure of cocoon is higher than that of ambient medium, and then cocoon thermally expands and transmits shock wave to ambient medium.

Since hotspot and lobes are filled with relativistic electrons and magnetic field, synchrotron radiation or radiation by inverse Compton scattering is emitted.

1.1.3 Dynamics of Relativistic Jets

High resolution observations with radio interferometer revealed that AGN jet is relativistic plasma flow and that various relativistic effects can be seen as follows.

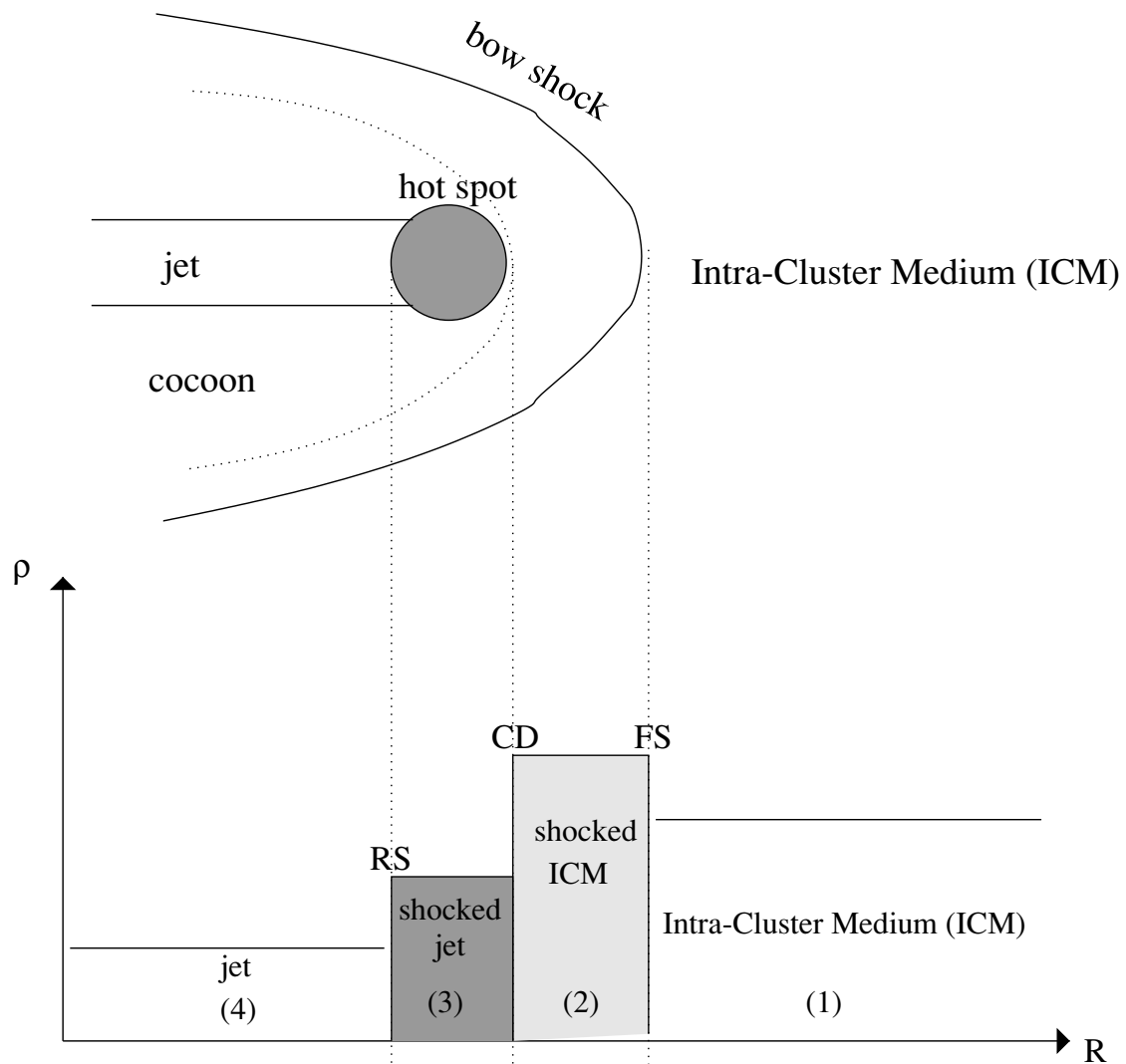


Figure 1.6. A schematic view of shock dissipation at the tip of the relativistic jet from Kino and Takahara (2004). The upper panel shows the model geometry of shocks in a FR2 radio galaxy. The lower panel shows the mass densities (ρ) in each region. FS, RS and CD represent the position of the forward shock front, the reverse shock front and the contact discontinuity, respectively. The reverse-shocked region is identified as a hotspot. The forward shock is identified as a bow shock. The cocoon is composed of shocked jet material that has expanded sideways.

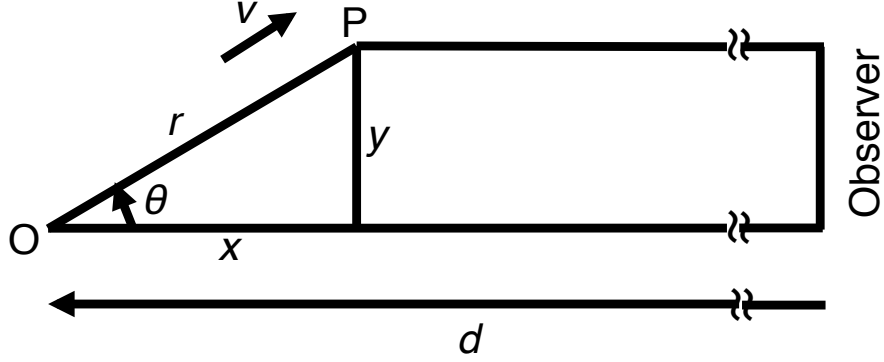


Figure 1.7. Geometrical configuration of superluminal motion.

Superluminal Motion

Superluminal motion is that AGN jet apparently exceeds the speed of light, when jet is launched at relativistic speed, nearly coincident with the line of sight. As shown in Figure 1.7, we assume a blazar is located at position O, distant d from an observer. At time $t = 0$, a bright cloud called jet knot is launched at speed v toward an angle θ with respect to the observer. Light emitted at the moment reaches the observer at $t = t_1 = d/c$, where c is the speed of light. Light emitted on arrival at the position P, reaches the observer at $t = t_2$. t_2 is the sum of knot traveling time from O to P and light traveling time from O to the observer,

$$t_2 = \frac{r}{v} + \frac{d-x}{c} = \frac{r}{v} + \frac{d-r\cos\theta}{c}. \quad (1.1)$$

From the view of the observer, the knot travels $y (= r \sin \theta)$ between $t = t_1$ and $t = t_2$, and then the apparent speed v_{app} is

$$v_{\text{app}} = \frac{y}{t_2 - t_1} = \frac{v \sin \theta}{1 - v/c \cos \theta}. \quad (1.2)$$

Therefore, when θ is smaller and v approaches the speed of light, the apparent speed of jet knot v_{app} can exceed the speed of light.

Relativistic Beaming Effect

Generally, AGN jets are launched toward both sides with respect to radio core, but the approaching jet looks brighter than the counter jet. When the jet motion is superluminal, only an approaching jet is observable. One-sided jet is ascribed to apparently slower speed and apparently dimmer brightness of counter jet due to intrinsically relativistic motion of jets. This phenomenon is called relativistic beaming effect. Special relativity theory tells us that a relation between a time interval Δt_s measured in the frame of a jet moving at Lorentz factor $\Gamma = (1 - \beta^2)^{-1/2}$, and Δt_{obs} measured in the rest frame of an observer is

$$\Delta t_{\text{obs}} = \Delta t_s / \delta, \quad (1.3)$$

where $\beta = v/c$, $\delta = 1/(\Gamma(1 - \beta \cos \theta_{\text{obs}}))$ is Doppler factor and θ_{obs} is a viewing angle of the jet with respect to the line of sight in the observer's frame. Then, the relation between frequency $\nu_s \propto 1/\Delta t_s$ and $\nu_{\text{obs}} \propto 1/\Delta t_{\text{obs}}$ is

$$\nu_{\text{obs}} = \delta \nu_s. \quad (1.4)$$

This relation indicates that light with higher frequency is detected when observing approaching jet knot nearly coincident with the line of sight.

Relativistic beaming effect is that light emitted from a moving object concentrate in moving direction. We assume that light travels toward an angle θ_s with respect to the moving direction of the jet knot. Lorentz transformation for traveling direction of light is

$$\cos \theta_s = \frac{\cos \theta_{\text{obs}} - \beta}{1 - \beta \cos \theta_{\text{obs}}}, \quad (1.5)$$

and then

$$\Delta \cos \theta_{\text{obs}} = \delta^{-2} \Delta \cos \theta_s. \quad (1.6)$$

Thus, light emitted into a certain solid angle in the frame of the jet knot is observed within a δ^2 smaller solid angle when viewed from the observer's frame. When light is emitted isotropically in the frame of jet knot, the number of photons is invariant in both frames, and then

$$\frac{L_{\nu_s}}{h\nu_s} \Delta \nu_s \Delta t_s 2\pi \Delta \cos \theta_s = \frac{L_{\nu_{\text{obs}}}}{h\nu_{\text{obs}}} \Delta \nu_{\text{obs}} \Delta t_{\text{obs}} 2\pi \Delta \cos \theta_{\text{obs}}. \quad (1.7)$$

Therefore,

$$\nu_{\text{obs}} L_{\nu_{\text{obs}}} = \delta^4 \nu_s L_{\nu_s}, \quad (1.8)$$

where h is Planck constant, and L_ν is specific luminosity, that is, luminosity per unit frequency. The product of frequency ν and L_ν represents luminosity per unit logarithmic frequency. Eq. (1.8) means that luminosity per unit logarithmic frequency in the frame of jet knot looks δ^4 times brighter in the observer's frame. For example, when we observe an approaching jet knot coincident with the line of sight at a relativistic speed $\Gamma = 10$, the intensity becomes 10^4 times higher. On the other hand, the intensity of receding (or counter) jet becomes 10^4 times lower. Then, it is hard to observe the receding jet, since the contrast between approaching and receding jets becomes 10^8 . Therefore, due to the observability, blazars are adequate sources to study jet structures and emission mechanisms since early times.

Blandford and Königl (1979) derived the ratio of brightness of equivalent components in the approaching and counter jets;

$$R = \left(\frac{1 + \beta \cos \theta_{\text{obs}}}{1 - \beta \cos \theta_{\text{obs}}} \right)^\eta, \quad (1.9)$$

where η is either $(2 - \alpha)$ or $(3 - \alpha)$ for a continuous jet or a single blob, respectively.

Here α is the spectral index satisfying $S_\nu \propto \nu^\alpha$, where S_ν is the flux density at frequency ν .

1.1.4 Formation and Evolution of Radio Sources

Jet and Radio Core

AGN jets are bridging structures between the vicinity of central engine and extended lobes. They are well-collimated and often seen at both sides or one side with respect to the center of AGNs. AGN jets extend from parsec to kiloparsec scales, and shines in the wavelength ranges from radio to X-ray. They transfer high energy particles at relativistic speed from central region of AGN to an intragalactic regions.

Mechanisms for launching and accelerating AGN jets are not well-established, but there are promising models using accretion disk. One is the radiative acceleration model (e.g., Icke, 1980). This model is that radiation pressure from accretion disk accelerates plasma electrons, and then jets are formed and accelerated. Another model is magnetic acceleration model based on magnetohydrodynamic (MHD) schemes (e.g., Uchida and Shibata, 1985; Meier et al., 2001). This model is that release of twisted magnetic field in the accretion disk drags and accelerates plasma electrons, and then jets are formed and accelerated. This model can also explain collimation of jets due to magnetic hoop stress of the toroidal magnetic field (see Figure 1.8).

The recent theoretical studies based on the general relativistic-MHD (GRMHD) simulations, suggested that jets are initially formed with large opening angles, and collimated and accelerated gradually in the inner $10^3 R_S$ regions, where R_S is Schwarzschild radius;

$$R_S = \frac{2GM}{c^2} \sim 3.0 \left(\frac{M}{M_\odot} \right) \text{ (km)}, \quad (1.10)$$

and M , G are mass and gravitational constant, respectively (e.g., McKinney, 2006; Komissarov et al., 2007). In these regions, the jets have concave paraboloidal shapes due to confinement by the magnetic hoop stress. At the downstream of these regions, the jets have conical shapes due to free of forces confining the jet flow.

High-resolution observations with very long baseline interferometer (VLBI) have recently been providing some evidence in favor of the (GR)MHD models (e.g., Junor et al., 1999; Gabuzda et al., 2000; Asada and Nakamura, 2012; Hada et al., 2013). Asada and Nakamura (2012) discovered a transition from parabolic to conical streamlines in the jet of radio galaxy M87, using the Very Long Baseline Array (VLBA), European VLBI Network (EVN) and MERLIN array. Figure 1.9 shows the jet width as a function of the deprojected distance from the core in units of Schwarzschild radius. As seen in Figure 1.9, the jet is described by two different shapes: (i) a concave parabolic shape with $z \propto r^{1.73 \pm 0.05}$, where z represents the axial distance from the core and r indicates the radius of the jet emission, on scales up to $\sim 2.5 \times 10^5 R_S$, and (ii) a conical shape with $z \propto r^{0.96 \pm 0.1}$ starting at $\sim 2.5 \times 10^5 R_S$. However, it is not easy to identify the toroidal

component or helical structure of the magnetic field by observing the projected direction of the magnetic field (B_{\perp} , a component perpendicular to the line of sight), unless the emission of the jet is highly polarized.

The emission from AGN jets at radio band is mainly synchrotron radiation, and linearly polarized perpendicular to the magnetic field. Thus, B_{\perp} is perpendicular to the observed polarization angle, and the radio emission from AGN jets should be highly polarized. However, emission from some AGN jets is unpolarized (e.g., Taylor et al., 2006, 0.2% at 22 GHz). This might be due to Faraday rotation, which twists the position angle χ_0 of linearly polarized emission as it propagates through the foreground plasma. The position angle is rotated by

$$\chi_{\text{obs}} = \chi_0 + \text{RM} \lambda^2, \quad (1.11)$$

where χ_{obs} is the observed polarization angle and RM is the rotation measure, and λ is the observed wavelength. The RM is proportional to the integral of the electron density (n_e) and the magnetic field parallel to the line of sight (B_{\parallel}), as $\text{RM} \sim \int_{\text{LOS}} n_e B_{\parallel} dr$, where $\int_{\text{LOS}} dr$ indicates integration along the line of sight. If RM changes across the source and the spatial resolution of an observation is insufficient to resolve this structure (so-called ‘‘beam depolarization’’), the degree of observed polarization may be very small. Therefore, a detailed analysis of both the RM and χ_{obs} is useful to investigate the three-dimensional structure of the magnetic field in the jet (e.g., Asada et al., 2002, 2008).

Hada et al. (2011, Figure 1.10) revealed that the central engine of M87 is located within $14 - 23R_S$ (0.007-0.01 pc) of the radio core at 43 GHz using multifrequency observation with VLBI, assuming that the jet is conical and the central engine is located at the apex of the jet, the separation between the central engine and a radio core at a given frequency ν satisfies $r_c(\nu) \propto \nu^{-\alpha}$ ($\alpha > 0$) (core-shift effect; e.g., Lobanov, 1998, see Figure 1.11). Here, radio cores are located at the apparent jet base in each frequency image, and basically considered to be opaque photospheres (surfaces with an optical depth of unity) against synchrotron self-absorption (SSA) or free-free absorption (FFA) (Blandford and Königl, 1979). On the other hand, the stationary standing shock model, which is also another idea explaining blazar radio cores, has proposed based on recent VLBI observations (e.g., Marscher et al., 2008, 2010; Agudo et al., 2011; Abdo et al., 2010, see Figure 1.12). These observations suggest that the central black holes are far from the radio cores by the order of $10^4 - 10^6 R_S$ ($\sim 0.1 - 10$ pc). Although detailed radio observations can provide the morphological structure of an inner jet, their stationarity is not well understood besides the location of the radio core. Thus, the positions of radio cores is an open question.

CSOs and Large-Scale Double Radio Sources

Large-scale double radio sources consist of a bright compact nucleus, relativistic and well-collimated jets, and huge double radio lobes. Blandford and Rees (1974) and Scheuer

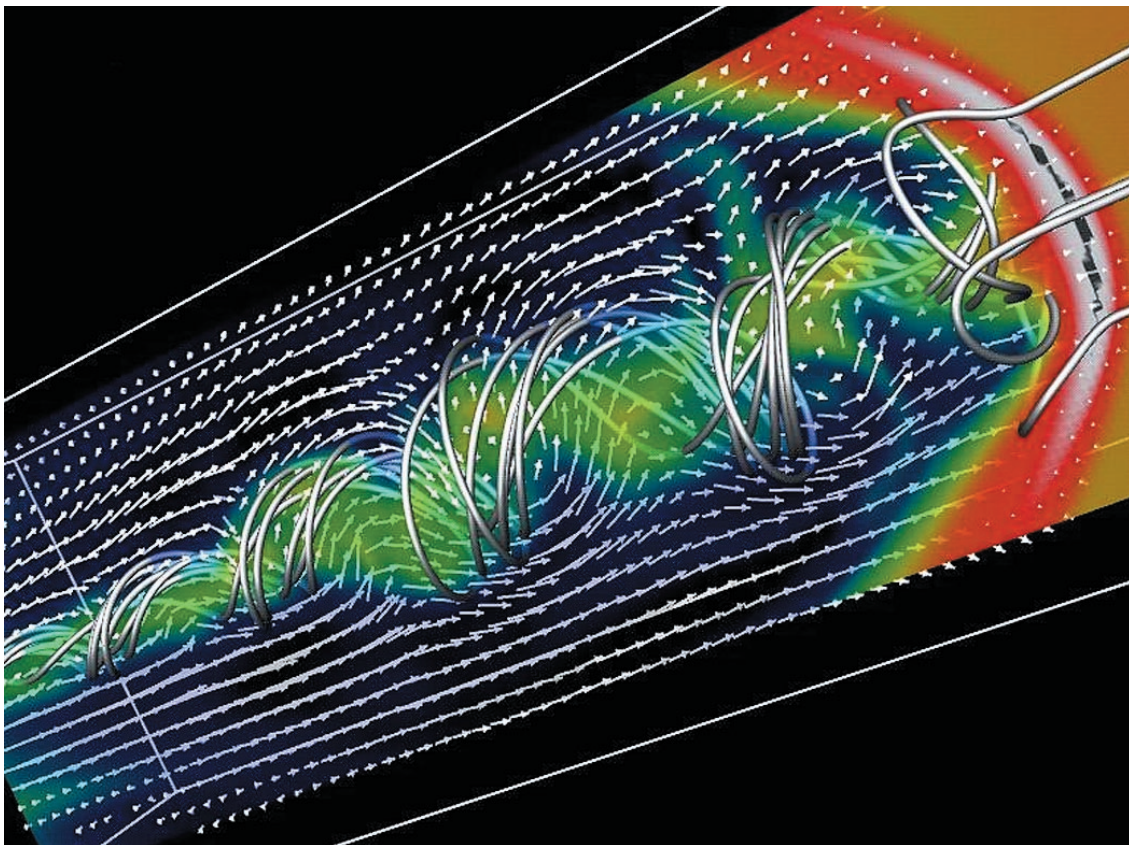


Figure 1.8. A three-dimensional (3D) simulation of the propagation of a magnetized jet, which represents most of the properties of the MHD model from Meier et al. (2001). The panel indicates flow velocity (arrows), the plasma density field (color scale with white and blue indicating high and low pressure, respectively), and the magnetic lines of force (metallic tubes). The initially axisymmetric, rotating jet has amplified a helical-magnetohydrodynamic instabilities that distorts its shape. The plasma flow still follows the magnetic field lines. Such an instability may explain the wiggles observed in some parsec-scale radio jets. The jet terminates in a strong shock wave at top right corner, as it propagates into a region with decreasing velocity. High-energy particles accelerated in the twisted magnetic field, and especially in the compressed magnetic field behind the bow shock, will emit synchrotron radiation. Thus, this shock may correspond to the hotspot often seen at the tip of jets in many radio sources.

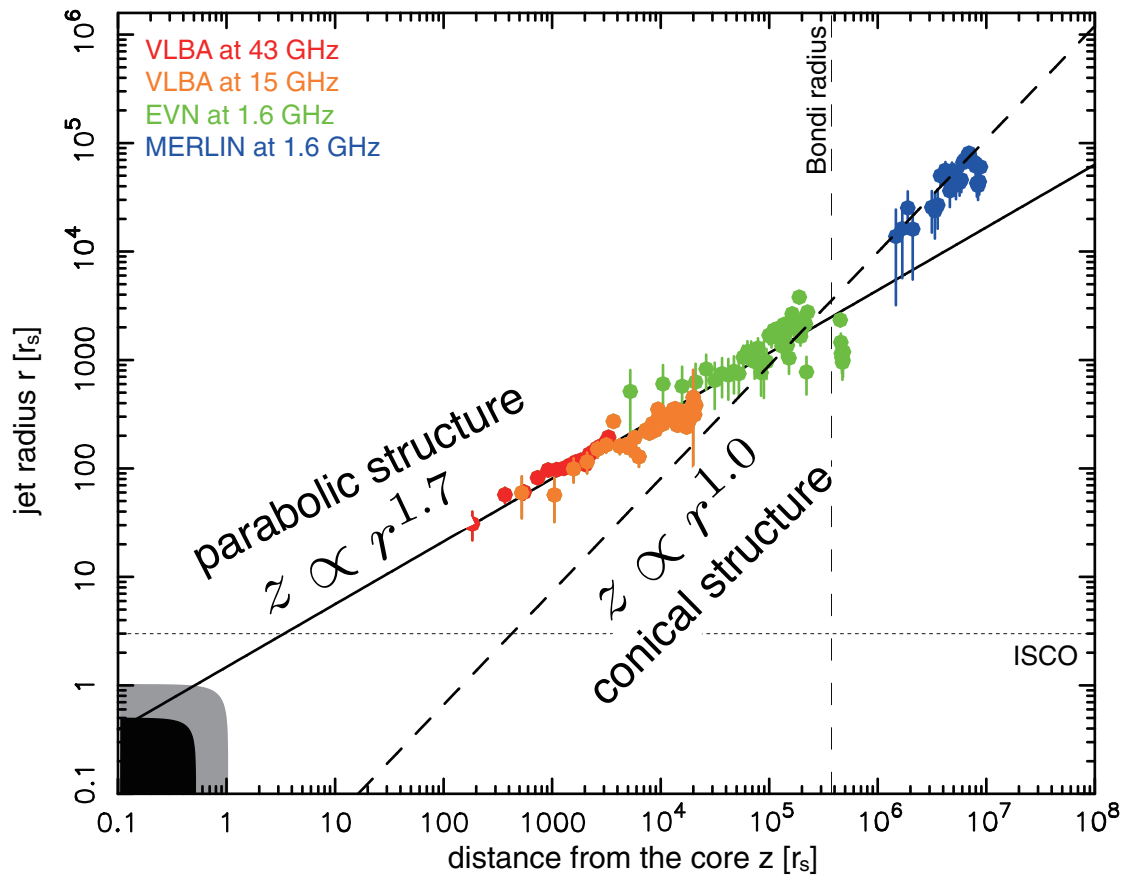


Figure 1.9. Relation between the jet radius r and the deprojected distance from the core z of M87 in units of Schwarzschild radius r_S revised from Asada and Nakamura (2012). Red and orange circles are observational data using the Very Long Baseline Array (VLBA), a VLBI array in the USA, at 43 GHz and at 15 GHz, respectively. Green and blue circles denote data points obtained with the European VLBI Network (EVN) at 1.6 GHz and with the MERLIN array at 1.6 GHz, respectively. The jet can be divided into two different shapes. The black solid line represents a parabolic structure with $z \propto r^{1.7}$, while the black dashed line shows a conical structure with $z \propto r^{1.0}$. The black area indicates the size of the minor axis of the event horizon of the spinning black hole with maximum spin. The gray area shows the size of the major axis of the event horizon of the spinning black hole with maximum spin, and coincides with the size of the event horizon of the Schwarzschild black hole. The gray dotted line represents the size of the innermost stable circular orbit (ISCO, $3r_S$) of the accretion disk for the Schwarzschild black hole. The gray dashed line indicates the Bondi radius, which is given by $2GM_{\text{BH}}/c_s^2$, where M_{BH} is the mass of the black hole and c_s is the sound speed of the hot gas surrounding a SMBH.

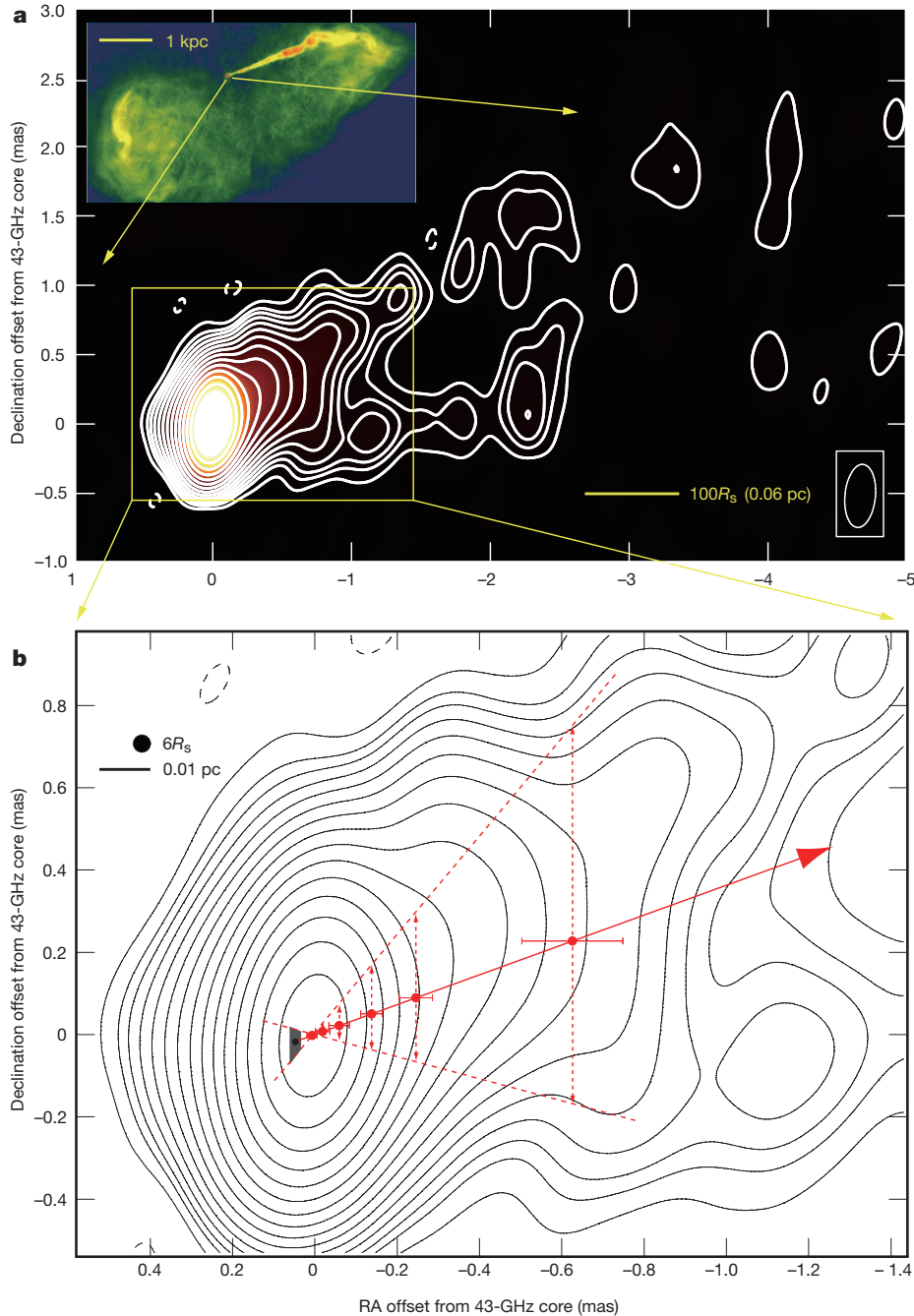


Figure 1.10. An image of M87 at 43 GHz superimposed on the measured core-shift positions observed with the VLBA from Hada et al. (2011). (a) Global view of the subparsec-scale radio jet. The yellow tick at bottom right corner indicates $100R_S$ (0.06 pc). The synthesized beam of the VLBA is 0.22×0.46 mas at -5 deg shown in bottom right corner. Inset in (a), is an image of kiloparsec-scale structure observed with 15-GHz Very Large Array (VLA), a phased radio interferometer in the USA. (b) Close-up view of the region enclosed by the yellow rectangle in (a). Red circles indicate the core positions at 2.3, 5.0, 8.4, 15.2, 23.8 and 43.2 GHz relative to the 43.2-GHz core (the higher the frequency of the core, the closer it approaches the central engine). Two broken red lines represent the maximum possible range of the inner jet direction centered on the 43.2-GHz core. A solid red arrow indicates the larger-scale jet direction. They assumed that the core shift occurs along the larger-scale jet direction. The black shaded area at the east of the 43.2-GHz core indicates the upstream end of the jet derived from the core-shift measurements. A black circle in top left corner shows the diameter $6R_S$ of the innermost stable orbit around a non-rotating black hole.

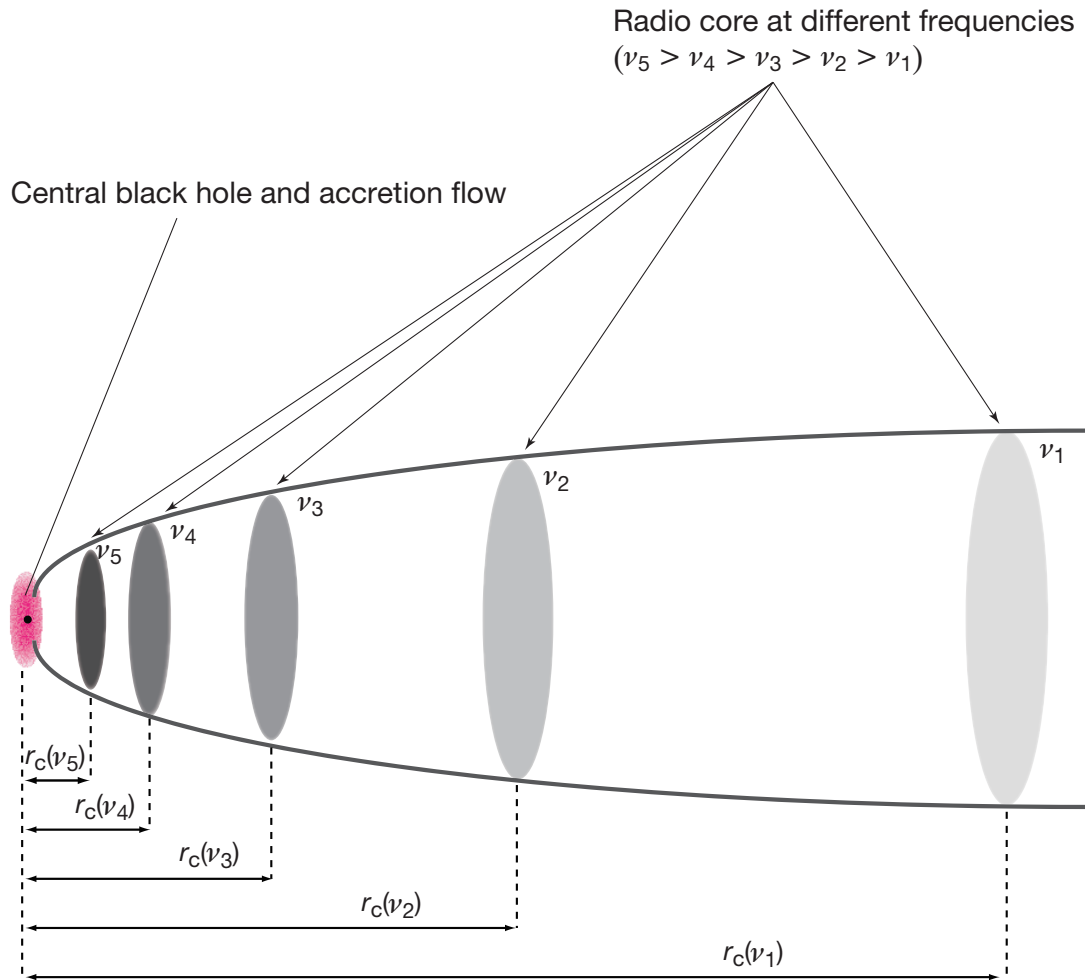


Figure 1.11. Schematic diagram explaining the shift effect of radio core (apparent jet base in a certain frequency) from Hada et al. (2011). The diagram indicates the core shift effect of a jet generated from the vicinity of central black hole (a black dot) surrounded by the accretion disk (a red ellipse), with the horizontal axis showing a distance from the black hole (r). The radio cores of a jet, the bright surfaces of optical depths of unity, are indicated as grey ellipses at the actual radio frequencies of VLBI observations; darker colors indicate higher frequencies. The cores are located at the apparent jet base in each frequency image. See the paper in detail.

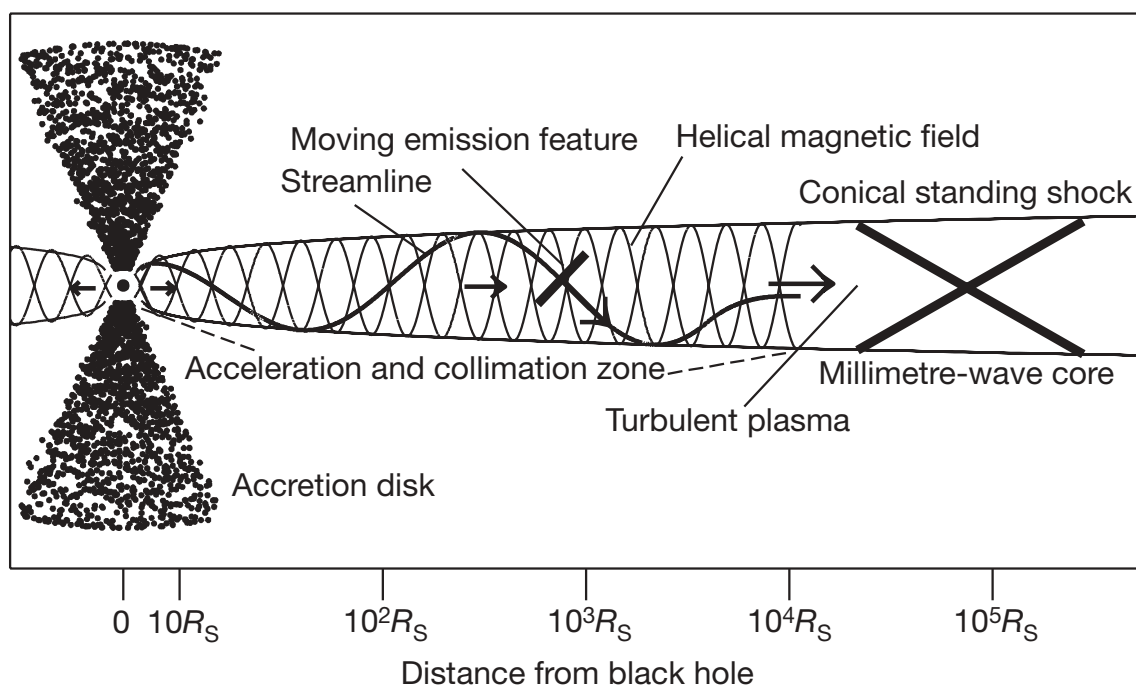


Figure 1.12. Stationary standing shock model for the inner jet of a blazar population (BL Lacertae) from Marscher et al. (2008). A shock propagates down the jet along a spiral streamline. The first flare occurs during the last 240 deg twist of the streamline before the flow straightens and becomes turbulent. The passage of the feature through the millimeter-wave core stimulates the second flare. A logarithmic scale of distance from the central black hole, shown in the unit of R_S).

(1974) discussed an evolution scenario of large-scale double radio sources, and the basic idea is briefly summarized as follows:

1. Well-collimated jets are launched from the vicinity of SMBH in opposite directions.
2. The jets travel, while keeping almost collimated shape, for distances of sometimes up to a few Mpc.
3. The jets collide with the surrounding ambient medium, and bulk kinetic energy of jet is dissipated by the strong terminal shocks which are identified as hotspots.
4. Due to shock wave heating, accelerated high-energy particles emanate from the hotspots to create backflows, and form radio lobe.
5. Shocked relativistic plasma expands sideways and envelopes the whole jet system and this is called cocoon.

This evolution scenario of large-scale double radio sources was tested by synchrotron aging theory (e.g., Pacholczyk, 1970). This theory is based on the idea that the plasma close to the hotspots shows a younger age than that far from the hotspots. Then, the ages of radio sources were estimated as $\sim 10^6 - 10^7$ years (e.g., Alexander and Leahy, 1987; Carilli et al., 1991).

Powerful FR1 and FR2 radio galaxies can have a significant impact on the environment in the host galaxies, since their sizes of structure are comparable to that of the host galaxies, sometimes beyond. The coevolution of SMBHs and galaxies has been discussed by many researchers who say that AGN feedback may be a key mechanism in regulating the growth of SMBHs and also in preventing star formation of galaxies (e.g., King, 2003; Murray et al., 2005; Granato et al., 2004; Kawata and Gibson, 2005; Okamoto et al., 2008).

However, it is not well-understood how we should treat AGN feedback associated with AGN jets, because we do not understand how small, young radio sources evolve into FR1 and FR2 galaxies. Thus, in order to understand AGN feedback, it need to explore conditions under which small, young radio sources can pass through a dense ambient medium within host galaxies.

Based on the evolution scenario mentioned above, we expect that young radio galaxies are compact. Actually, a large number of compact, bright double-lobe radio sources as compact symmetric objects (CSOs), whose overall size is ≤ 1 kpc, have been discovered (Wilkinson et al., 1994; Fanti et al., 1995; Readhead et al., 1996b,a). The structure of CSOs resemble that of large-scale double radio sources, except for the extremely compact size. This hypothesis is verified by estimating their age based on direct measurements of the advance speed of hotspots of several CSOs (e.g., Owsianik et al., 1998; Taylor et al., 2000; Polatidis and Conway, 2003; Nagai et al., 2006). They showed that the advance speed is typically $\sim 0.1c$, indicatig a dynamical age of $\sim 10^2 - 10^4$ years which implies that CSOs are possible candidates as the progenitors of large-scale double radio sources.

Kawakatu et al. (2008) examined the evolution of various sizes of 117 radio galaxies by comparing the relation between the hotspot size and the projected linear size (Figure 1.13) with a coevolution model of hotspots and a cocoon (Kawakatu and Kino, 2006). They categorized radio galaxies into three groups according to their projected hotspot distance from the core (l_h); CSOs ($l_h \leq 1$ kpc), medium-size symmetric objects (MSOs; $1 \leq l_h \leq 10$ kpc), FR2 radio galaxies ($l_h \geq 1$ kpc). They found that the advance velocity of hotspots and lobes (v_{HS}) inevitably show the deceleration phase (CSO-MSO phase; $v_{\text{HS}} \propto l_h^{-1}$) and the acceleration phase (MSO-FR2 phase; $v_{\text{HS}} \propto l_h^{0.3}$). They predict that only CSOs whose initial advance velocity (at the time when the two-dimensional (2D) phase (cocoon head (A_h) growth phase) starts (5 pc from the center of the galaxy)) is higher than $\sim 0.1c$ can evolve into FR2 galaxies, comparing the hotspot speed with the sound speed of the ambient medium. These results indicate that the advance velocity of hotspots during the 1D phase (constant A_h phase) controls the fate of CSOs. In order to understand the evolution of young radio sources, it is necessary to reveal the end of the 1D phase of hotspot evolution. Thus, we need to discover the candidates for ultracompact symmetric radio source (e.g., $l_h < 5$ pc) such as high-frequency peaker (HFP). This class of sources has been intensively observed, and a large number of the sources are being detected (e.g., Orienti et al., 2007), using high-resolution VLBI (e.g., Snellen, 2008). It is very important to unveil the physical conditions for the transitions from 1D phase to 2D phase as well as to predict the fate of CSOs.

1.2 Aim of the Dissertation

AGN jet is a key feedback processes for galaxy evolution, since jet can heat intragalactic gas and prevent gas from cooling and forming stars. Thus, it is inevitable to ignore influences of AGN jets, considering galaxy formation and evolution. However, formation and evolution mechanisms for AGN jets are still unclear. It is necessary to unveil the physics of the vicinity of jet nozzle in order to understand the formation process of radio jet. The jet base can be spatially resolved by VLBI. Then, I studied the physical conditions in the vicinity of jet nozzle of nearby radio galaxy 3C 84 with VLBI.

1.3 Review of 3C 84

As described in § 1.1, radio-loud AGNs often have relativistic jets emanating from the vicinities of central SMBH. Radio galaxies are believed to be misaligned radio-loud AGNs within the unified model of AGN (Urry and Padovani, 1995). Thus, these are ideal sources to explore general properties of AGN jets since the misalignment of the jet axis with the line of sight provides a detailed view of the structure in the jet.

The bright radio source 3C 84 is associated with the giant elliptical galaxy NGC 1275 ($z = 0.0176$; Petrosian et al., 2007), which is a dominant member of the Perseus cluster

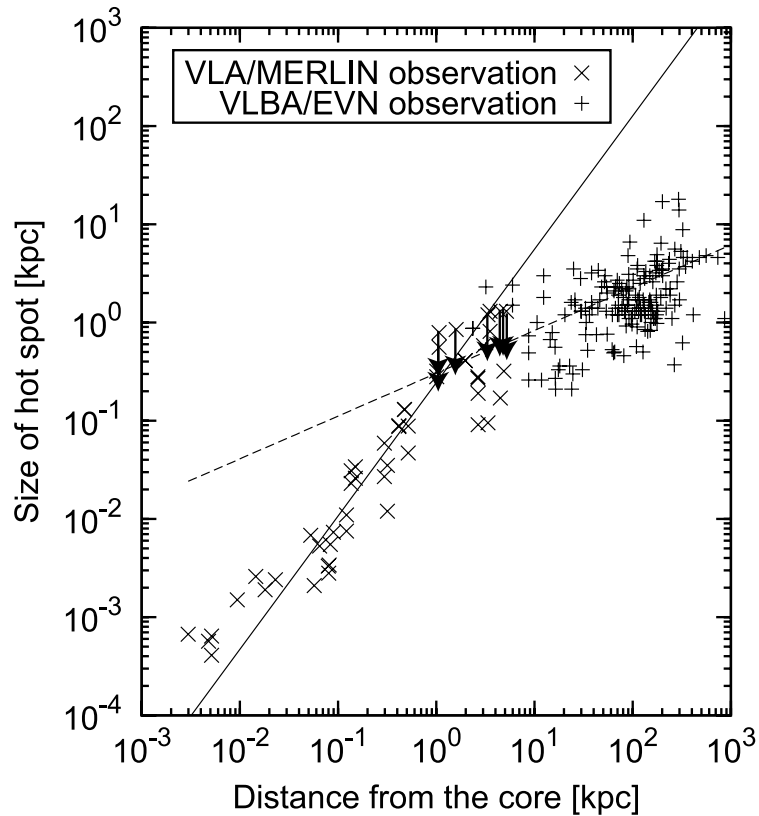


Figure 1.13. Relation between hotspot size (r_{HS}) and hotspot distance from the core (l_h) from Kawakatu et al. (2008). Crosses with arrows represents the upper limit. The solid line corresponds to the best-fit for the sources where $10^{-3} < l_h < 1$ kpc, whereas the dashed line corresponds to that for the sources where $1 < l_h < 10^3$ kpc. Upper limit data were not used in the fittings.

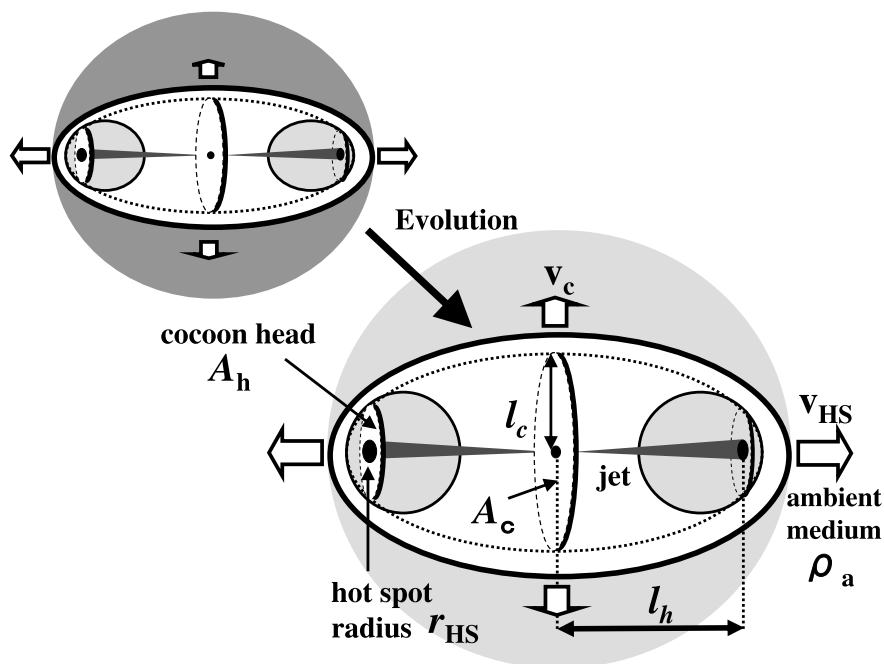


Figure 1.14. Schematic view of the evolution of radio sources from Kawakatu et al. (2008). The aspect ratio of the cocoon is defined as $R = l_c/l_h$.

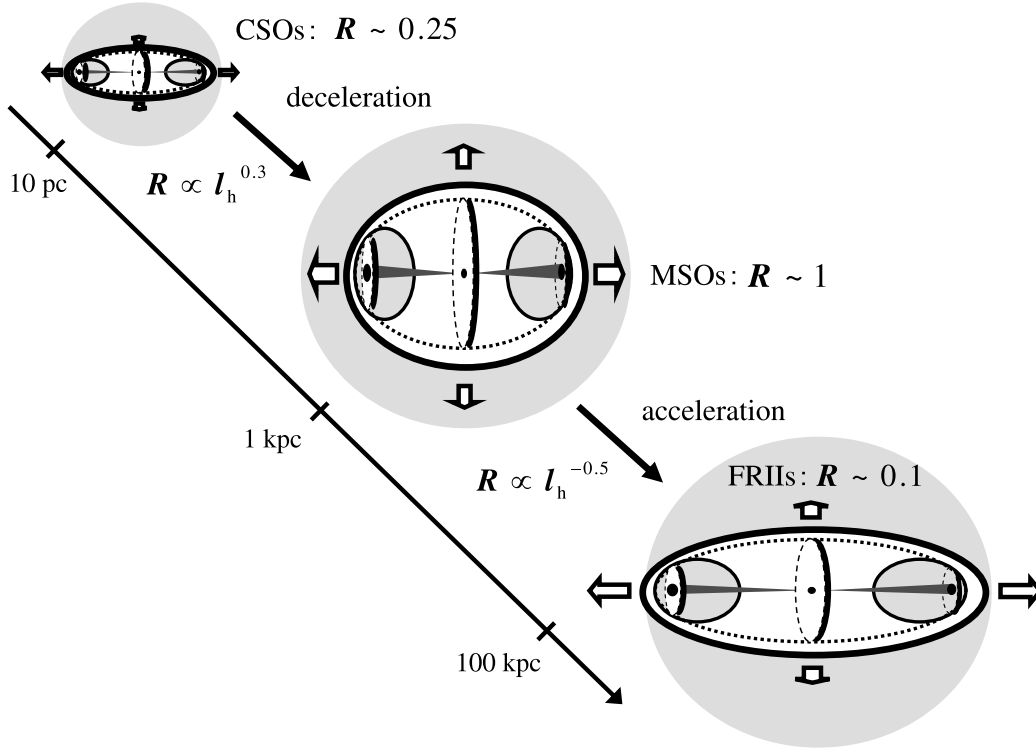


Figure 1.15. Schematic view of the evolution of a cocoon morphology derived from the predictions from Kawakatu et al. (2008).

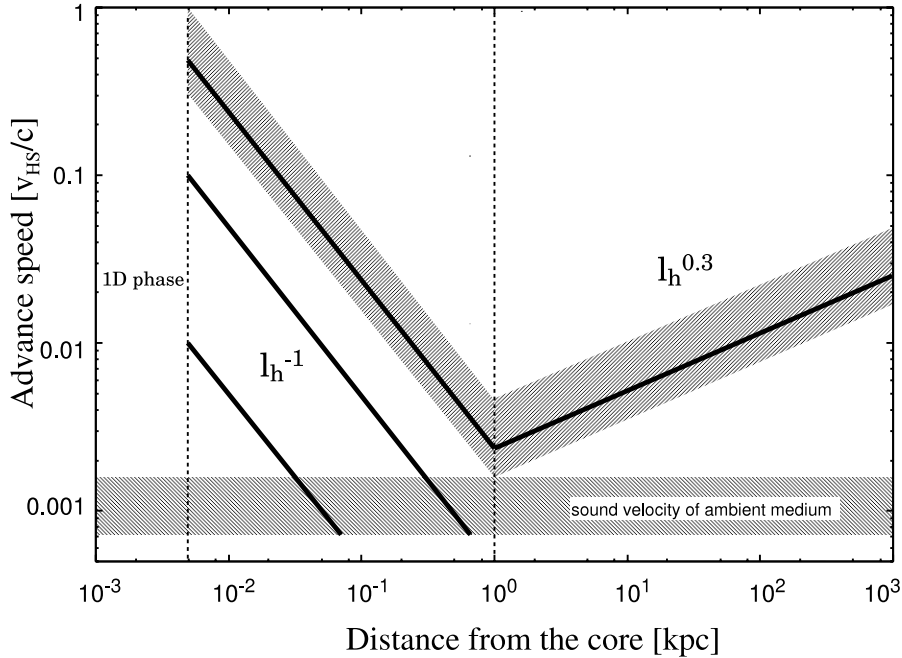


Figure 1.16. Predictions of evolution of v_{HS} from Kawakatu et al. (2008). $v_{\text{HS}} \propto l_h^{-1}$ for $l_h < 1$ kpc and $v_{\text{HS}} \propto l_h^{0.3}$ for $l_h > 1$ kpc. The black solid lines denote the evolution of v_{HS} for $v_{\text{HS}}(l_{h,2\text{D}}) = 0.01, 0.1$ and $0.5c$, where $l_{h,2\text{D}} = 5$ pc. The upper shaded region indicates the evolutionary path from CSOs into FR2 radio galaxies. The lower shaded region represents the range of sound velocity of the ambient medium, $7 \times 10^{-4}c < c_s < 1.4 \times 10^{-3}c$ ($5 \times 10^6 < T_g < 2 \times 10^7$ K), where T_g is the temperature of the surrounding ambient medium.

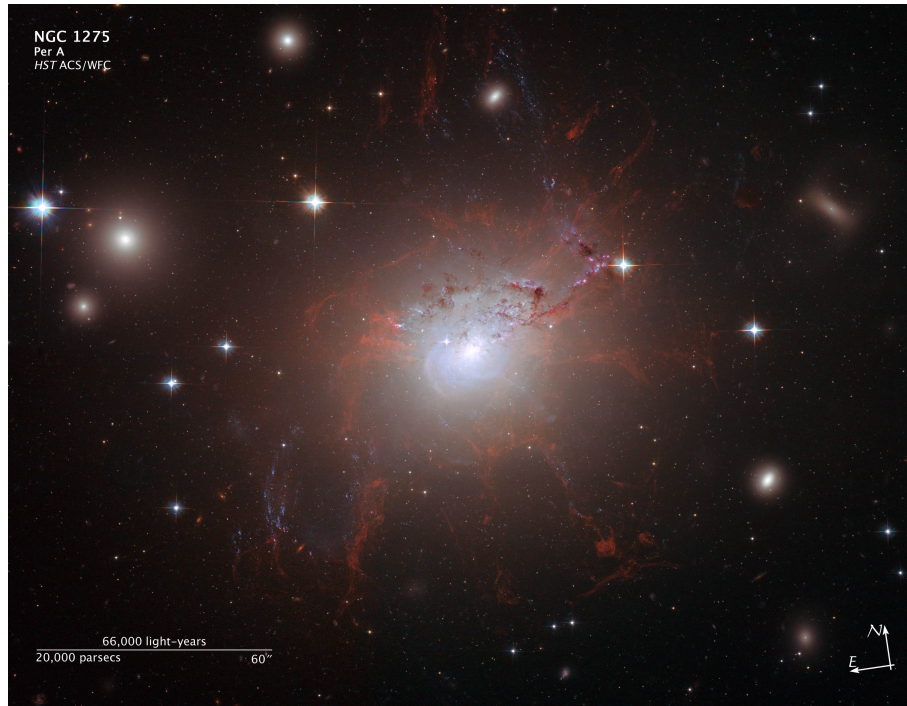


Figure 1.17. A Hubble Space Telescope optical image of galaxy NGC 1275. NGC 1275 is the central, dominant member of the large and relatively nearby Perseus Cluster of Galaxies. The red filaments consist of cool gas suspended by a magnetic field, and are surrounded by the $\sim 6 \times 10^7$ K hot gas in the center of the Perseus galaxy cluster. Image is 3.87 arcmin across. A thick bar at the bottom left corner corresponds to 60 arcsec (20 kpc). Credit: NASA, ESA, and the Hubble Heritage (STScI/AURA)-ESA/Hubble Collaboration (<http://hubblesite.org/newscenter/archive/releases/2008/28/image/b/>)

(see Figure 1.17). The radio emission continues on larger scales, and shows a clear interaction with the hot cluster gas. Observations with X-ray satellites (*ROSAT*; Boehringer et al. (1993) and *Chandra*; Fabian et al. (2003, 2006)) unveil the presence of cavities in the gas, indicating that the jets of 3C 84 have blown multiple bubbles in the hot intracluster medium. The Perseus cluster is the nearest and best source of a prototypical “cooling core” cluster: the radiative cooling time of the X-ray emitting gas is considerably shorter than the age of the universe. Heating by the central AGN is believed to be responsible for balancing the radiative cooling. However, it is not well-understood that the exact mechanisms of transportation and dissipation of energy.

Its proximity allows us to investigate not only large-scale structures, but also the central subparsec-scale region, where the jet nozzle is located, with the high angular resolution provided by observations with VLBI. Therefore, 3C 84 is an ideal source to study the formation mechanism of relativistic jet powered by SMBH and the interaction between the jets and ambient medium in the vicinity of the SMBH.

3C 84 is an uncommon source exhibiting intermittent jet activity. Its radio morphology has multiple lobe-like features with different position angles on broad spatial scales from pc to ~ 10 kpc (e.g., Pedlar et al., 1990; Walker et al., 2000, see Figure 1.18). 3C 84 also shows pairs of 100 kpc-scale X-ray bubbles misaligned with each other (Dunn et al.,

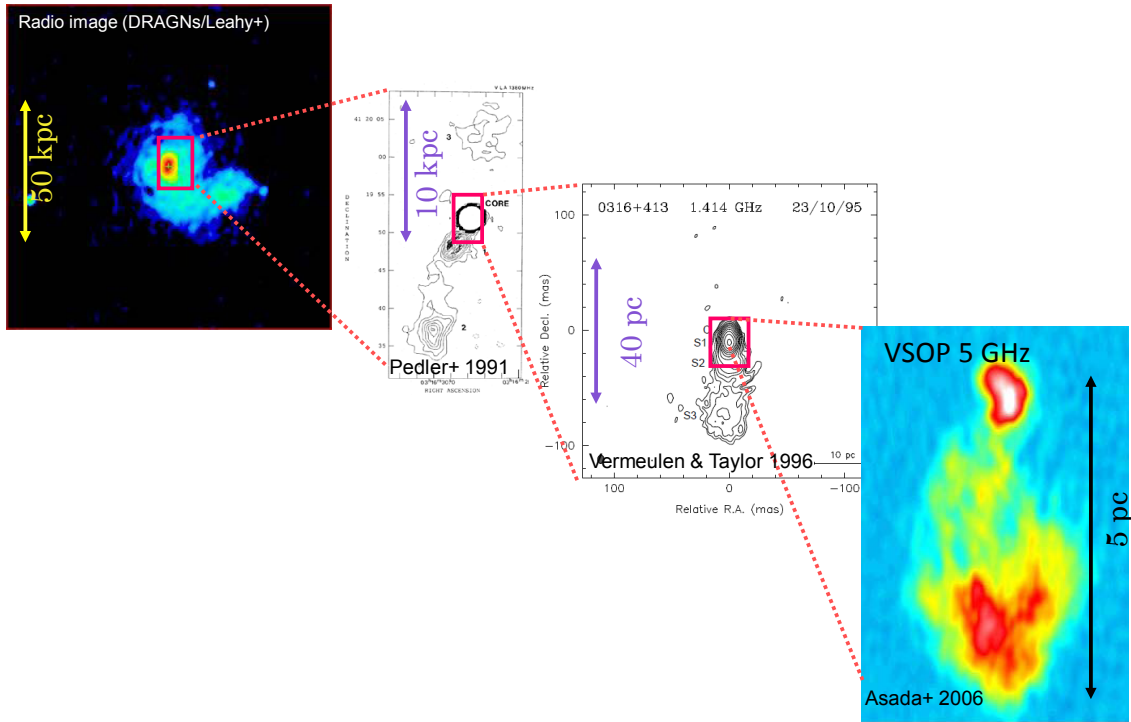


Figure 1.18. Intermittent jet activities of 3C 84. Multiple lobe-like features with different position angles from parsec to 10-kpc scales in radio morphology can be seen.

2006).

In the central 5–10 pc scale region, 3C 84 has two-sided compact radio jets/lobes, which were probably formed by the jet activity originating in the 1959 flare (Vermeulen et al., 1994; Walker et al., 1994, 2000; Asada et al., 2006). The morphology of 3C 84 is similar to Compact Symmetric Objects (CSOs: Readhead et al., 1996a) as well as a Fanaroff-Riley type-I radio galaxy (e.g., Dhawan et al., 1998). Despite CSO-like morphology, it is not a genuine young radio source because of the presence of large scale morphology. According to the Very Long Baseline Array (VLBA) observation at 43 GHz in the 1990’s, Dhawan et al. (1998) revealed that the inner 0.5 pc of the core has bright knots of emission located along a line with multiple sharp bends. These bends may also reflect a precessing jet nozzle, or three-dimensional hydrodynamic Kelvin-Helmholtz instabilities in 3C 84 (Dhawan et al., 1998), but no one has directly observed the wobbling motion of a particular component.

3C 84 did not undergo significant enhancement in the jet activities in the central subparsec-scale region during 1959 and early 2000s, which was observationally suggested by monotonical decrease in its radio flux density. However, monitoring observation at 14.5 GHz with a single-dish radio telescope at the University of Michigan Radio Astronomy Observatory (UMRAO) has detected brightening restarting in 2005 (Abdo et al., 2009a, see Figure 1.19). Using the VLBI Exploration Radio Astrometry (VERA) at 22 GHz for 14 epochs from 2006 to 2009, Nagai et al. (2010) found that this activity was ascribed to the central subparsec-scale region, accompanying the ejection of the new bright component (C3). Therefore, 3C 84 is an adequate source for studying ongoing recurrent

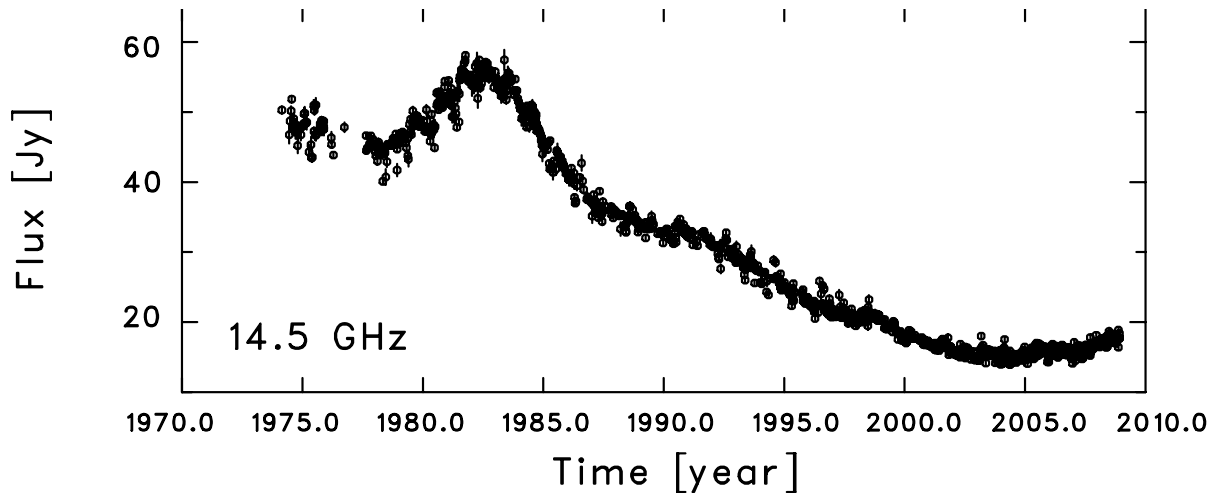


Figure 1.19. A 14.5 GHz long-term radio light curve of 3C 84 observed with a single-dish radio telescope at the UMRAO between 1974 February and 2008 December revised from Abdo et al. (2009a). The flux density has started brightening around 2005. Here, $1 \text{ Jy} = 10^{-23} \text{ erg s}^{-1} \text{ cm}^{-2} \text{ Hz}^{-1}$.

jet activity in the central subparsec-scale region. Using higher spatial resolution observations with VLBA at 43 GHz for 28 epochs from 2002 to 2008, that is, earlier epochs than those discussed in Nagai et al. (2010), Suzuki et al. (2012) found that C3 had emerged from the bright region (C1) before 2005, and traveled southward following a parabolic trajectory on the celestial sphere (see Figure 1.20). Suzuki et al. (2012) also found that the apparent speed of C3 with reference to C1 shows moderate acceleration from $0.10c$ to $0.47c$ between 2003 November and 2008 November, but is still sub-relativistic. In addition, Suzuki et al. (2012) measured the spectral index (α) of each component on 2008 November 27. They defined the spectral index between 43 GHz and 22 GHz as $\alpha_K^Q = \log(S_Q/S_K)/\log(43/22)$, where S_Q and S_K are the flux density of components at 43 GHz and 22 GHz, respectively. As shown in Figure 1.21, the spectrum of C1 was flat ($\alpha_K^Q \sim 0$), whereas those of C2 and C3 were steep ($\alpha_K^Q \sim -0.9$), where C2 is a bright region already present before the emergence of C3. Thus, they interpreted C1 as the radio core, and C2 and C3 as optically thin jet components.

In order to understand the formation mechanism of jet, it is important to study kinematic properties in the vicinity of jet base. In this thesis, we present the detailed kinematics in the central subparsec-scale region of 3C 84 with VERA at 22 GHz for 80 epochs from 2007 to 2013, that is, later epochs than those discussed in Suzuki et al. (2012) and Nagai et al. (2010) in order to reveal the physical properties in the vicinity of jet base. In particular, we investigate kinematics of C3 in detail by monitoring the subsequent motion for non-linear trajectory found by Suzuki et al. (2012). In order to confirm the nature of C3, we will also discuss it by approaching from light curve in a forthcoming paper.

The redshift of 3C 84 corresponds to the angular scale of $0.353 \text{ pc mas}^{-1}$ ($0.1 \text{ mas yr}^{-1} =$

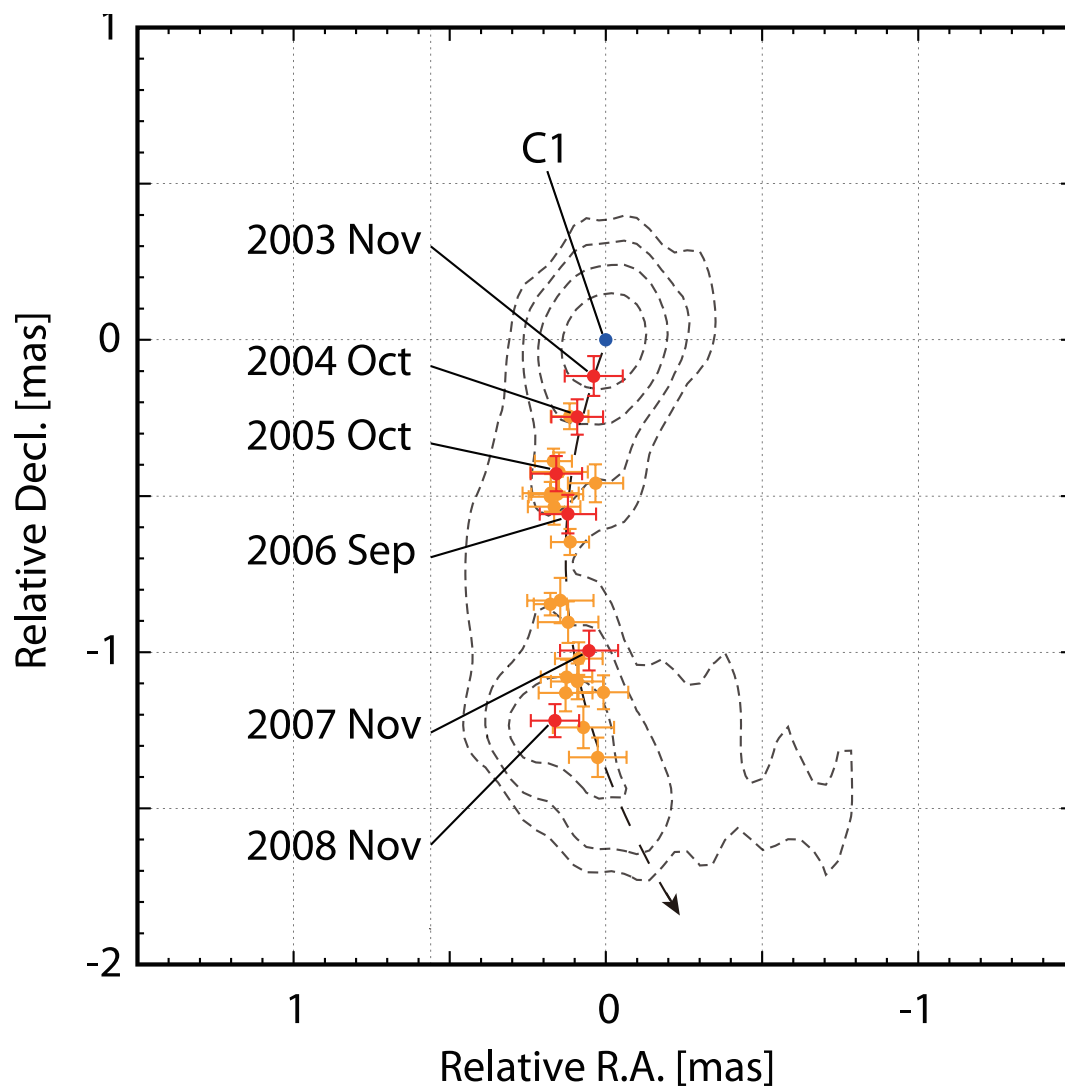


Figure 1.20. Peak position of a new bright component (C3) for all 25 epochs between 2003 November 20 and 2008 November 27, superposed on the contours of 43 GHz intensity distribution on 2008 November 27 revised from Suzuki et al. (2012). The dashed parabolic arrow traces the average positional change of C3. The position of a radio component (C1) is fixed at the origin.

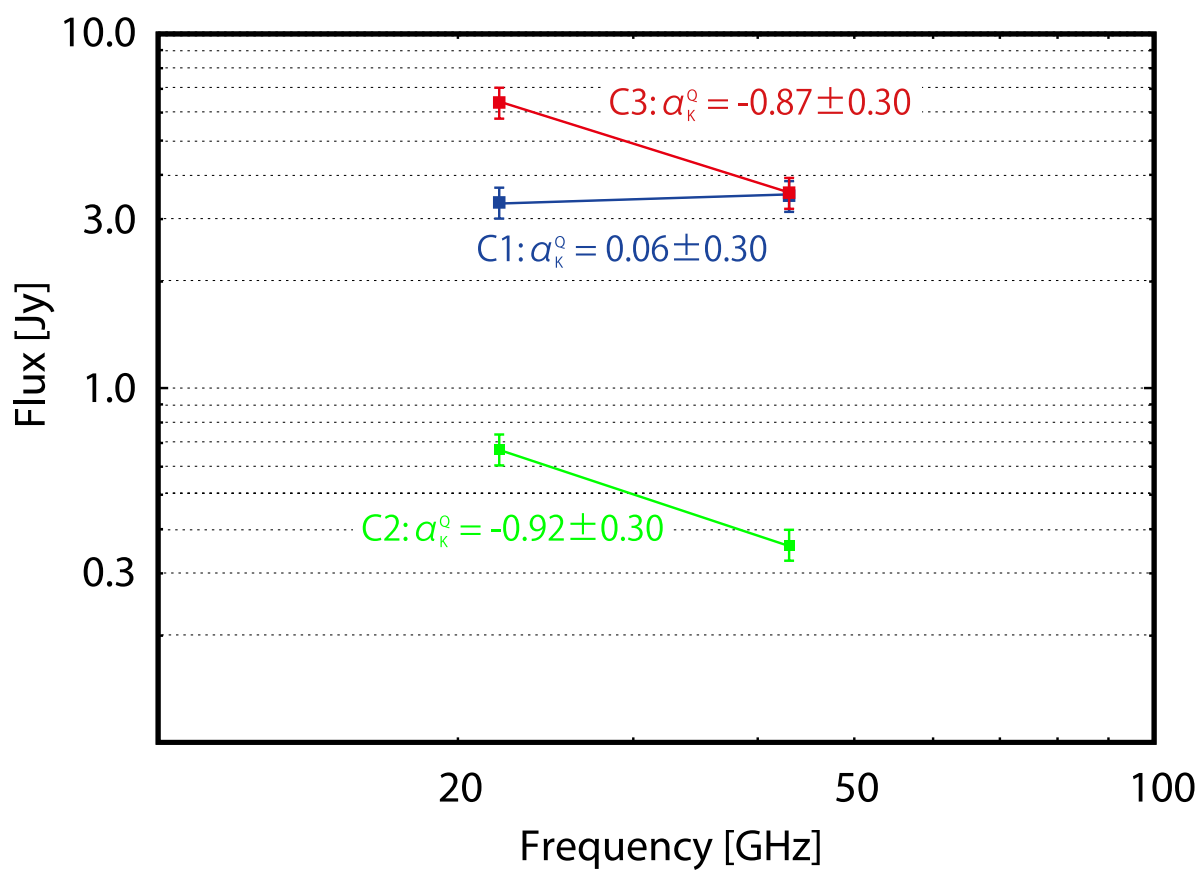


Figure 1.21. Spectral indices (α_k^Q) of C1, C2 and C3 between 22 GHz and 43 GHz on 2008 November 27 from Suzuki et al. (2012). The error of flux density is 10% of the flux density of each component.

0.115 c) assuming $H_0 = 71 \text{ km s}^{-1} \text{ Mpc}^{-1}$, $\Omega_M = 0.27$, and $\Omega_\Lambda = 0.73$ (Komatsu et al., 2009). The mass of the central SMBH was estimated to be $3.4 \times 10^8 M_\odot$ (Wilman et al., 2005), which yields $10^3 R_S = 9.2 \times 10^{-2} \text{ mas} = 3.3 \times 10^{-2} \text{ pc}$, where R_S is Schwarzschild radius.

2

Observation and Data Reduction

2.1 The VERA observation at 22 GHz

In order to investigate the detailed kinematics of C3, we mainly used the GENJI programme (Gamma-ray Emitting Notable AGN Monitoring with Japanese VLBI; Nagai et al., 2013) data at 22 GHz (2010 November - 2013 December, 68 epochs). The GENJI programme aims for dense sampling of gamma-ray loud AGNs using the VLBI Exploration of Radio Astrometry (VERA) array, aiming for the Galactic maser astrometry (shown in Figure 2.1). It needs to monitor a bright calibrator once in every ~ 80 minutes. We use GENJI sources including 3C 84 as the calibrator. One of the goal of the GENJI programme is to identify the radio counterpart of the gamma-ray emitting region by comparing radio light curve with gamma-ray one. The GENJI programme also aim to study the kinematics of the jet. We pay attention to the time variation on a time scale shorter than one month, which provides quick follow-up observations after gamma-ray flares. Typically, each GENJI source was monitored almost once every two weeks. Such frequent monitoring is unexampled at 22 GHz in the northern hemisphere (see Table 2.1 about GENJI and other AGN monitoring projects). Thanks to this dense monitoring, we can obtain rich data of 3C 84 on subparsec scales.

The VERA consists of four stations with the maximum baseline length of $\sim 2,270$ km. This corresponds to typical angular spatial resolution of ~ 1 mas. In addition to the GENJI programme data, we used the published data (Nagai et al., 2010, 2007 October - 2008 May, 7 epochs) and the archival data of VERA (2009 February - 2010 February, 5 epochs) at 22 GHz. In each observation, total on-source time for 3C 84 was typically 30 minutes, consisting of 4-6 scans at different hour angles. Figure 2.2 shows a typical interferometric uv -coverage taken on 2013 December 20.

After left-hand circular polarization radio frequency (RF) signals at 22 GHz band were amplified by the receiver, the RF signals were mixed with the standard frequency signal generated in the first local oscillator and converted to an intermediate frequency (IF) signals of 4.7–7 GHz. The first local frequency was fixed at 16.8 GHz. Then, the IF signals were mixed again with the second local frequency, and converted to baseband

(0-512 MHz). The second local frequency is tunable with a possible frequency range between 4 GHz and 7 GHz. The correction of the Doppler effect owing to the earth rotation was carried out in the following correlation process after the observation. Thus, the second local frequency was kept to be constant during the observation. The converted baseband signals were sampled with 2-bit quantization by A/D converter. After that, the digital signals were filtered with the VERA digital filter unit (Iguchi et al., 2005), providing 16 IF-bands with a bandwidth of 256 MHz (16-MHz bandwidth per an IF-band). The filtered signals were recorded at a rate of 1024 Mbps (Figure 2.3). 14 IF-bands (224-MHz bandwidth) of a total 16 IF-bands were assigned to 3C 84. Due to a bandpass characteristic of an analog filter equipped in front of the digital filter, significant signal ($\sim 30\%$) was lost. Thus, we did not use the data of the 13th and 14th IF-bands. Correlation processes were performed using the Mitaka FX correlator (Chikada et al., 1991). Each correlated IF-band was dispersed into 64 channels.

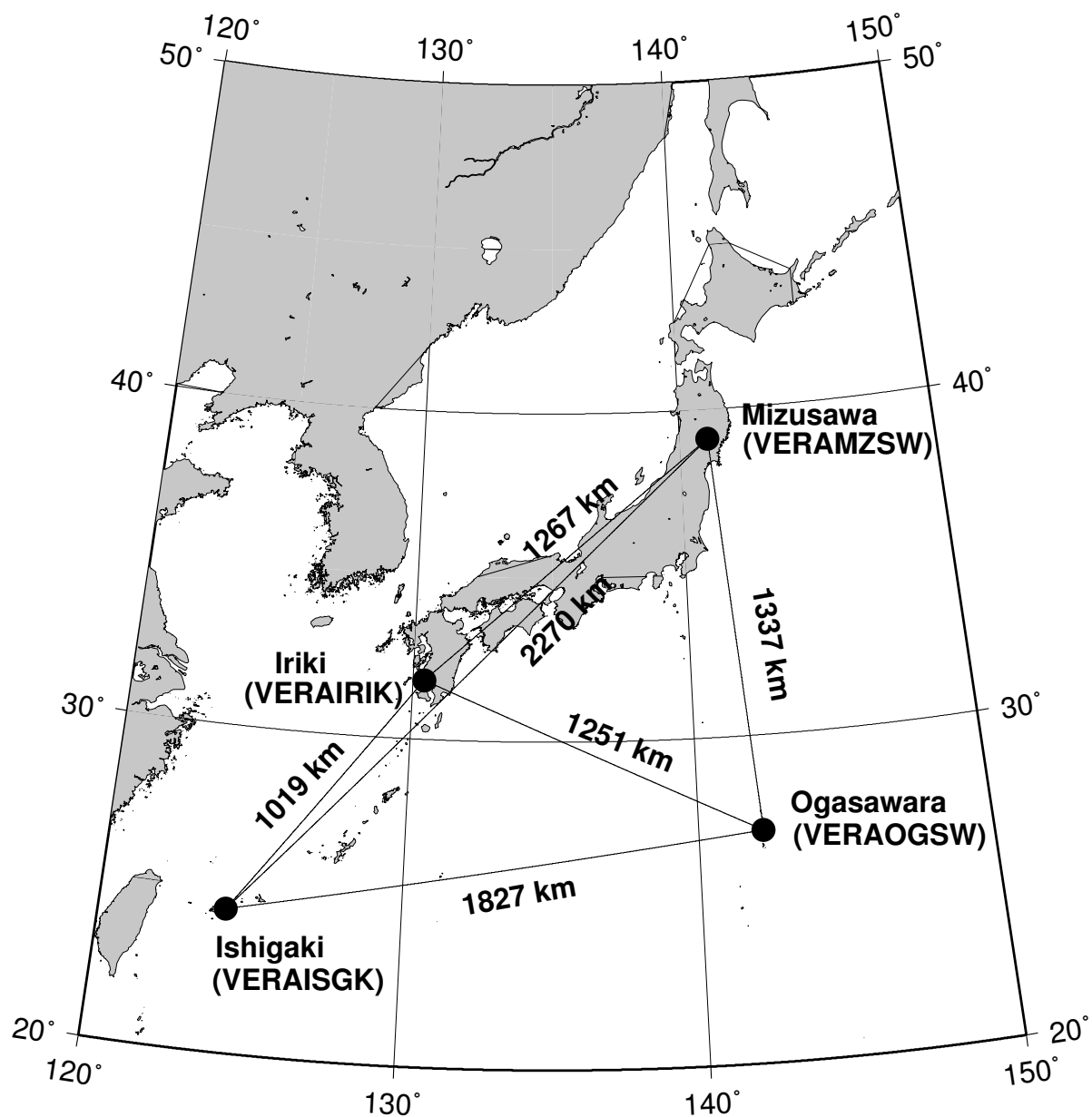


Figure 2.1. The configuration of VERA array from VERA Status Report in 2011 (Mizusawa VLBI Observatory, 2011)

Table 2.1. AGN monitoring projects.

Project	Frequency band	Monitoring interval	Typical angular resolution	Source declination
GENJI (Nagai et al., 2013)	22 GHz	~ 2 weeks	~ 1.2 mas	northern hemisphere
MOJAVE* (Lister et al., 2009)	15 GHz	~ 3 weeks	~ 0.6 mas	northern hemisphere
Boston University blazar monitoring program [†]	43 GHz	~ 1 month	~ 0.5 mas	northern hemisphere
TANAMI [‡] (Ojha et al., 2010)	8.4 & 22 GHz	~ 2 months	~ 1.0 mas	southern hemisphere

* <https://www.physics.purdue.edu/astro/mojave/>† <http://www.bu.edu/blazars/research.html>‡ <http://pulsar.sternwarte.uni-erlangen.de/tanami/>

2.2 Data calibration and imaging

The observable obtained with VLBI is a complex visibility $\mathcal{V}_\nu(u, v)$ at frequency ν , and this is two-dimensional (2D) Fourier transformation of the brightness distribution on the plane of the sky $I_\nu(x, y)$ at frequency ν , where (x, y) is a sky coordinate (usually in the equatorial coordinate) relative to a reference position (so-called “phase-tracking center”). The relation between $\mathcal{V}_\nu(u, v)$ and $I_\nu(x, y)$ is described as

$$\mathcal{V}_\nu(u, v) = g_i g_j^* \iint_{\text{source}} I_\nu(x, y) e^{2\pi i(ux+vy)} dx dy, \quad (2.1)$$

where $g_i = |g_i|e^{i\phi_i}$ is the complex gain, including amplitude and phase, of i -th antenna. Thus, we can obtain the brightness distribution of sources when we observe visibilities with various pairs of spatial frequency (u, v) , and perform inverse Fourier transformation of them.

$$g_i g_j^* I_\nu(x, y) = \int_{u=-\infty}^{\infty} \int_{v=-\infty}^{\infty} \mathcal{V}_\nu(u, v) e^{-2\pi i(ux+vy)} du dv. \quad (2.2)$$

This equation is called Van Cittert-Zernike’s theorem, and represents the relation between the brightness distribution $I_\nu(x, y)$ and visibility $\mathcal{V}_\nu(u, v)$. Actually, since observed visibilities include information (complex gain in block) arising from receivers and frequency standard when passing through the Earth’s atmosphere and observational instruments, they are different from the real visibility. Relation between observed visibility $\mathcal{V}_{\text{obs}}^{ij}$ and real visibility \mathcal{V}^{ij} is

$$\mathcal{V}_{\text{obs}}^{ij} = g_i(\nu, t) g_j^*(\nu, t) \mathcal{V}^{ij} + \epsilon_{ij}, \quad (2.3)$$

where ϵ_{ij} is random noise. When we calibrate data obtained with VLBI, we estimate real visibility from observed one by calibrating the phase and amplitude of complex gain.

Data reduction was performed using the National Radio Astronomy Observatory (NRAO) Astronomical Imaging Processing System (AIPS) in the same way as discussed in Nagai et al. (2013). First, we flagged the data of nine channels at both edges of each IF-band due to a bad bandpass characteristic of the filter. Then, we normalized the crosscorrelation by the autocorrelation. A standard *a priori* amplitude calibration was performed using the AIPS task APCAL, based on measurements of the system temperature (T_{sys}) by the chopper-wheel method during the observation, and on the aperture efficiency provided in the VERA Status Report in 2009. The opacity correction in the task APCAL was not performed, since the T_{sys} derived from the chopper-wheel method includes the effect of atmospheric absorption. This amplitude calibration provides an accuracy of 10%, according to a number of experiences using VERA (e.g., Petrov et al., 2012). Since observational instruments such as antennas, receivers and bandpass filters have bandpass characteristic, we need to calibrate bandpass characteristic in order to obtain correct visibility. We calibrated bandpass characteristic of visibility amplitude using autocorrelation spectra in the AIPS task BPASS, since signal-to-noise (S/N) ratio of autocorrelation function is higher than that of crosscorrelation function. In addition,

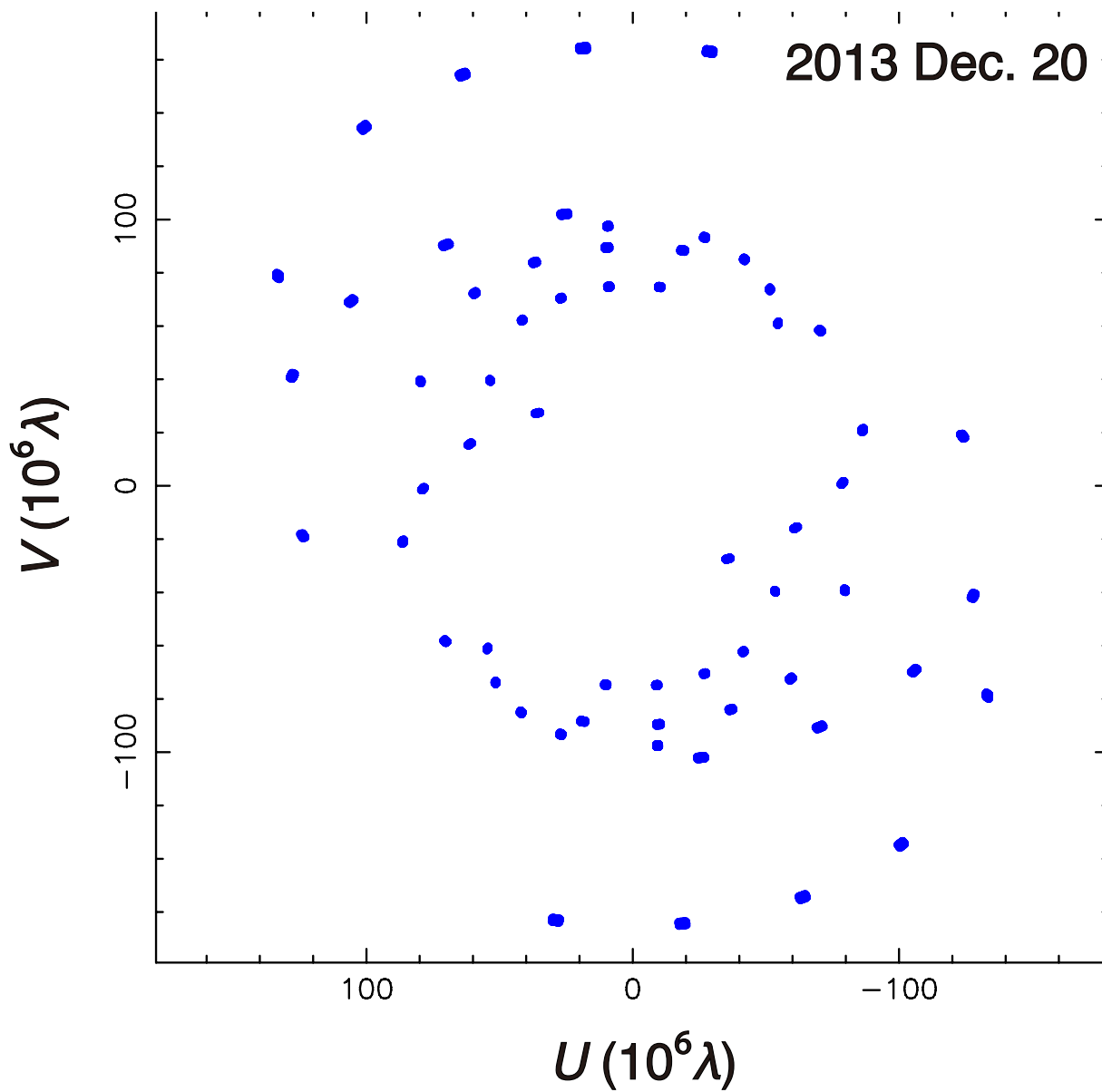


Figure 2.2. The interferometric uv -coverage taken on 2013 December 20.

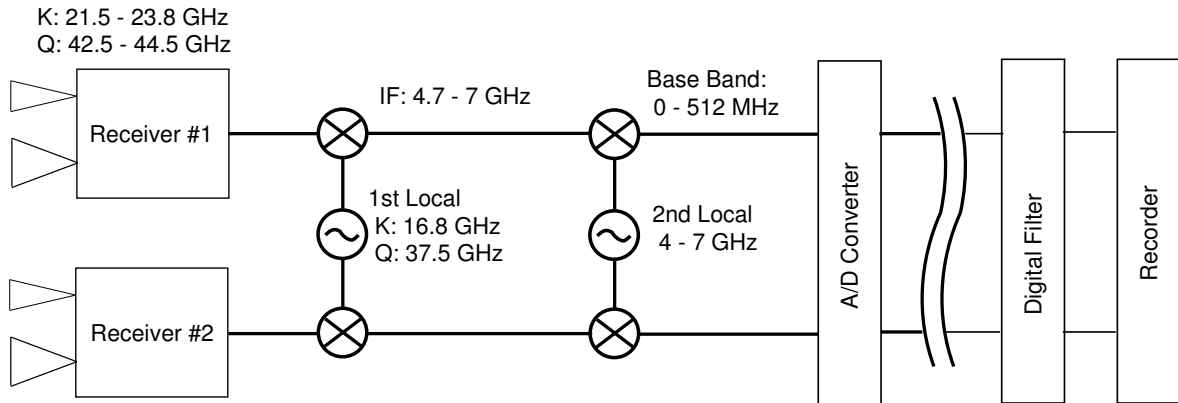


Figure 2.3. The signal-flow diagram from receivers to a recorder of VERA array from VERA Status Report in 2011 (Mizusawa VLBI Observatory, 2011). Although the second local frequency is tunable with a possible frequency range between 4 GHz and 7 GHz, it was kept to be constant during the observation. This is because the correction of the Doppler effect due to the earth rotation was carried out in the correlation process after the observation.

autocorrelation function dose not suffer from coherence loss because phase of autocorrelation function is always zero. Thus, autocorrelation function is suitable to calibrate bandpass characteristic of visibility amplitude correctly. As for calibration of visibility phase of VERA array, we need not calibrate it, since the bandpass characteristic is almost flat. Fringe fitting was performed using the AIPS task FRING. After carefully flagging the bad data, the data were averaged 10 sec in the time domain and over a bandpass.

At the step of imaging procedure, we constructed the initial source model with circular Gaussian distribution using *modelfit* implemented in the Difmap software package (Shepherd et al., 1994), not using the CLEAN algorithm (Högbom, 1974), since it is known that the central subparsec-scale structure of 3C 84 is spatially resolved with the VERA synthesized beam (e.g., Nagai et al., 2010) and that side-lobe level is relatively high due to the sparse uv -coverage sampled with VERA (see Figure 2.2). Thus, it is difficult to distinguish signal from noise using the CLEAN algorithm. In this process, we fitted multiple circular Gaussian model components to the visibility data. Assuming that a model intensity distribution $I_{\text{model}}(x, y)$ includes n -parameters (p_0, p_1, \dots, p_{n-1}) and is expressed as $I_{\text{model}}(x, y) = F(l, m; p_0, p_1, \dots, p_{n-1})$, the model visibility $\mathcal{V}_{\text{model}}(u, v)$ is the Fourier transform of $I_{\text{model}}(x, y)$ and expressed as $\mathcal{V}_{\text{model}}(u, v) = \text{FT}[I_{\text{model}}(x, y)] = \hat{F}(u, v; p_0, p_1, \dots, p_{n-1})$. Thus, $\mathcal{V}_{\text{model}}(u, v)$ also includes n -parameters. We searched the best-fit parameters minimizing the weighted residual χ^2 between the observed visibility $\mathcal{V}_{\text{obs}}(u, v)$ and $\mathcal{V}_{\text{model}}(u, v)$. The weighted residual χ^2 is calculated as follows,

$$\chi^2 = \sum_{i=0}^{N-1} \left(\frac{\mathcal{V}_{\text{obs}}(u_i, v_i) - \mathcal{V}_{\text{model}}(u_i, v_i)}{\sigma} \right)^2, \quad (2.4)$$

where σ is error of the observed visibility. We used circular Gaussian models which have

four parameters; total flux density, distance from the map center, position angle with respect to the map center and full width at half maximum (FWHM) of peak intensity.

Next, we performed self-calibration of visibility phase and amplitude using $\mathcal{V}_{\text{model}}(u(t), v(t))$ derived by *modelfit* process. In this process, we estimated real complex gain (g) by minimizing a weighted χ^2 as follows,

$$\begin{aligned}\chi^2 &= \sum_{i,j} \int_t \frac{1}{\sigma_{\mathcal{V}}^2} |\mathcal{V}_{\text{obs}}(t) - \mathcal{V}_{\text{model}}(t)|^2 dt \\ &= \sum_{i,j} \int_t \frac{1}{\sigma_{\mathcal{V}}^2} |\mathcal{V}_{\text{obs}}(t) - g_i g_j^* \tilde{\mathcal{V}}_{\text{model}}(t)|^2 dt\end{aligned}\quad (2.5)$$

,where $\sigma_{\mathcal{V}}$ is error of the observed visibility and $\tilde{\mathcal{V}}_{\text{model}}(t)$ satisfies,

$$\mathcal{V}_{\text{model}}(t) = g_i g_j^* \tilde{\mathcal{V}}_{\text{model}}(t). \quad (2.6)$$

In this way, we performed self-calibration adjusting the visibility phase in order to minimize χ^2 with conserving the closure phase. We performed a number of iterations of *modelfit* as well as phase self-calibration. When $\sigma_{\mathcal{V}}$ converged, then we switched to both phase and amplitude self-calibration processes on successively shortened calibration time (t) within a negligible change of antenna gain (~ 8 minutes). When $\sigma_{\mathcal{V}}$ converged, the final images were obtained after a number of iterations of *modelfit*, and phase and amplitude self-calibration processes. In total, our dataset consists of 80 epochs of subparsec-scale data shown in Table 2.2. Here, total model-fitted flux (S_{total}) was the sum of the flux density of all Gaussian components modeled in § 2.3, and its error for each image was estimated assuming the amplitude calibration error was 10% of total flux density, according to a number of experiences using VERA (e.g., Petrov et al., 2012).

Table 2.2. Epoch, rms, synthesized beam size, peak brightness, and total model-fitted flux for all images.

Epoch		Image noise rms	Beam	I_{peak}	S_{total}
Date	MJD-54397	(mJy beam ⁻¹)	(mas × mas, deg)	(Jy beam ⁻¹)	(Jy)
	(1)		(2)	(3)	(4)
2007 Oct. 24	0	27.9	1.29 × 0.76, -54.7	3.5	8.4 ± 0.8
2007 Nov. 20	27	42.0	1.17 × 0.83, -53.4	4.4	9.9 ± 1.0
2007 Dec. 27	64	27.1	1.24 × 0.73, -52.8	4.1	10.5 ± 1.0
2008 Feb. 4	103	34.9	1.27 × 0.79, -58.1	4.1	9.9 ± 1.0
2008 Mar. 3	131	38.0	1.18 × 0.75, -49.5	3.7	9.0 ± 0.9
2008 Apr. 15	174	27.0	1.27 × 0.80, -53.8	4.7	10.6 ± 1.1
2008 May. 20	209	30.6	1.31 × 0.78, -51.1	4.9	11.0 ± 1.1
2009 Feb. 19	484	10.4	1.19 × 0.75, -46.6	5.1	13.7 ± 1.4
2009 May. 17	571	18.3	1.24 × 0.83, -49.2	5.9	15.2 ± 1.5
2009 Sep. 23	700	18.6	1.22 × 0.82, -45.7	5.4	15.0 ± 1.5
2009 Nov. 2	740	15.8	1.18 × 0.77, -46.9	5.2	14.8 ± 1.5
2010 Feb. 8	838	14.5	1.20 × 0.78, -42.9	5.4	14.5 ± 1.4
2010 Nov. 28	1131	35.0	1.23 × 0.79, -54.6	6.7	16.7 ± 1.7
2010 Nov. 29	1132	27.3	1.25 × 0.90, -64.8	6.9	15.0 ± 1.5
2010 Dec. 4	1137	18.2	1.26 × 0.79, -45.2	7.0	16.6 ± 1.7
2011 Jan. 11	1175	48.3	1.21 × 0.79, -45.0	6.9	18.3 ± 1.8
2011 Jan. 29	1193	36.9	1.18 × 0.79, -49.2	6.7	18.5 ± 1.8
2011 Feb. 3	1198	49.2	1.24 × 0.83, -39.8	6.8	17.1 ± 1.7
2011 Feb. 12	1207	37.2	1.37 × 0.76, -74.1	7.1	19.2 ± 1.9
2011 Apr. 21	1275	19.8	1.23 × 0.75, -62.4	7.0	18.9 ± 1.9
2011 May. 18	1302	33.2	1.23 × 0.75, -60.7	7.2	19.1 ± 1.9
2011 Aug. 16	1392	26.7	1.11 × 0.75, -54.6	8.4	21.2 ± 2.1
2011 Sep. 12	1419	53.4	1.29 × 0.72, -42.3	8.8	21.5 ± 2.1
2011 Sep. 13	1420	19.4	1.38 × 0.76, -61.8	9.2	21.4 ± 2.1
2011 Sep. 14	1421	3.7	1.46 × 0.71, -54.8	9.1	21.5 ± 2.1
2011 Oct. 16	1453	29.3	1.18 × 0.79, -49.3	9.3	21.8 ± 2.2
2011 Oct. 17	1454	19.7	1.30 × 0.78, -69.8	10.2	23.8 ± 2.4
2011 Nov. 7	1475	24.1	1.21 × 0.83, -58.6	10.5	23.8 ± 2.4
2011 Nov. 20	1488	19.5	1.20 × 0.81, -58.0	10.4	23.8 ± 2.4
2011 Dec. 24	1522	27.5	1.24 × 0.76, -64.0	10.2	24.5 ± 2.5
2012 Jan. 17	1546	25.6	1.29 × 0.75, -65.3	11.0	26.3 ± 2.6
2012 Jan. 18	1547	28.0	1.26 × 0.78, -72.8	10.7	24.4 ± 2.4
2012 Jan. 21	1550	62.4	1.20 × 0.78, 49.7	10.5	24.0 ± 2.4
2012 Jan. 22	1551	18.9	1.18 × 0.84, -67.8	10.5	24.9 ± 2.5
2012 Jan. 29	1558	30.9	1.21 × 0.80, -64.2	9.8	24.3 ± 2.4
2012 Feb. 10	1570	25.2	1.25 × 0.76, -49.4	10.2	23.4 ± 2.3
2012 Feb. 19	1579	25.5	1.22 × 0.80, -44.6	10.7	23.7 ± 2.4
2012 Mar. 9	1598	29.0	1.22 × 0.82, -63.9	10.7	25.9 ± 2.6
2012 Mar. 19	1608	22.6	1.15 × 0.77, -51.0	10.3	26.8 ± 2.7
2012 Apr. 4	1624	32.3	1.33 × 0.72, -65.7	10.6	28.6 ± 2.9
2012 Apr. 8	1628	29.1	1.35 × 0.72, -69.4	11.1	28.7 ± 2.9
2012 Apr. 13	1633	29.1	1.28 × 0.70, -45.7	10.6	26.1 ± 2.6
2012 Apr. 26	1646	38.6	1.35 × 0.76, -48.6	12.0	28.1 ± 2.8

Table 2.2. Epoch, rms, synthesized beam size, peak brightness, and total model-fitted flux for all images.

Epoch		Image noise rms	Beam	I_{peak}	S_{total}
Date	MJD-54397	(mJy beam ⁻¹)	(mas × mas, deg)	(Jy beam ⁻¹)	(Jy)
	(1)		(2)	(3)	(4)
2012 Apr. 30	1650	24.8	1.27 × 0.75, -61.7	11.9	28.4 ± 2.8
2012 May. 14	1664	19.1	1.17 × 0.90, -0.5	11.7	24.6 ± 2.5
2012 May. 16	1666	92.3	1.09 × 0.76, -68.0	10.9	27.7 ± 2.8
2012 Jun. 1	1682	24.1	1.28 × 0.69, -72.8	10.9	27.3 ± 2.7
2012 Jun. 4	1685	28.8	1.25 × 0.72, -57.9	10.6	26.8 ± 2.7
2012 Jul. 28	1739	31.3	1.21 × 0.72, -59.5	10.1	25.8 ± 2.6
2012 Aug. 14	1756	28.4	1.32 × 0.74, -55.4	10.9	26.5 ± 2.6
2012 Aug. 27	1769	26.7	1.44 × 0.67, -65.1	10.1	25.9 ± 2.6
2012 Sep. 7	1780	69.6	1.30 × 0.70, -73.4	10.3	26.9 ± 2.7
2012 Sep. 10	1783	29.9	1.31 × 0.72, -69.3	10.3	26.1 ± 2.6
2012 Sep. 21	1794	24.5	1.26 × 0.76, -71.0	11.0	27.4 ± 2.7
2012 Sep. 23	1796	29.9	1.28 × 0.76, -60.5	10.8	25.5 ± 2.5
2012 Oct. 1	1804	24.5	1.26 × 0.78, -47.1	11.1	25.2 ± 2.5
2013 Jan. 15	1910	31.2	1.34 × 0.75, -56.7	10.5	25.1 ± 2.5
2013 Jan. 29	1924	31.5	1.27 × 0.71, -52.2	11.0	25.9 ± 2.6
2013 Jan. 30	1925	36.4	1.19 × 0.73, -61.0	11.0	26.2 ± 2.6
2013 Feb. 1	1927	42.1	1.27 × 0.66, -51.3	10.2	25.0 ± 2.5
2013 Feb. 4	1930	37.8	1.06 × 0.94, -52.1	11.5	26.2 ± 2.6
2013 Feb. 15	1941	27.7	1.38 × 0.74, -51.5	11.5	25.8 ± 2.6
2013 Mar. 10	1964	18.5	1.20 × 0.82, -27.3	10.8	24.1 ± 2.4
2013 Mar. 15	1969	26.4	1.28 × 0.69, -49.6	10.5	25.2 ± 2.5
2013 Mar. 22	1976	45.9	1.33 × 0.68, -66.3	10.3	27.2 ± 2.7
2013 Mar. 25	1979	34.2	1.42 × 0.67, -68.1	10.4	26.9 ± 2.7
2013 Apr. 1	1986	28.4	1.23 × 0.78, -56.0	11.1	25.7 ± 2.6
2013 Apr. 17	2002	44.6	1.33 × 0.71, -69.8	10.2	28.2 ± 2.8
2013 Apr. 29	2014	36.1	1.40 × 0.70, -56.4	10.5	26.6 ± 2.7
2013 Apr. 30	2015	48.8	1.05 × 0.78, -52.7	9.7	25.4 ± 2.5
2013 May. 26	2041	86.6	1.10 × 0.80, -67.3	10.2	27.4 ± 2.7
2013 Aug. 17	2124	39.7	1.25 × 0.73, -57.8	10.4	26.9 ± 2.7
2013 Aug. 22	2129	37.5	1.19 × 0.77, -50.9	10.8	27.7 ± 2.8
2013 Sep. 10	2148	32.3	1.29 × 0.69, -44.1	10.4	25.7 ± 2.6
2013 Sep. 16	2154	32.8	1.29 × 0.75, -61.1	10.7	27.6 ± 2.8
2013 Oct. 10	2178	38.9	1.24 × 0.75, -48.0	11.2	28.2 ± 2.8
2013 Oct. 12	2180	35.4	1.32 × 0.72, -54.0	11.0	29.2 ± 2.9
2013 Nov. 2	2201	40.6	1.23 × 0.72, -59.1	10.9	31.0 ± 3.1
2013 Nov. 8	2207	34.7	1.16 × 0.79, -58.0	11.3	29.1 ± 2.9
2013 Dec. 20	2249	40.6	1.19 × 0.72, -57.6	10.4	30.1 ± 3.0

Notes.

(1) Time gap between Modified Julian Date (MJD) of the epoch and MJD 54397 (2007 Oct. 24).

(2) Major axis, minor axis, and position angle of synthesized beam.

(3) Peak brightness for each image.

(4) Total model-fitted flux and its error for each image. The amplitude calibration error is assumed to be 10% of flux density, according to a number of experiences using VERA (e.g., Petrov et al., 2012).

2.3 Gaussian Model Fitting

In order to quantify the position, size, flux density of each component of 3C 84 on subparsec scales, we modeled the source structure of the final map calibrated in § 2.2 using the task *modelfit* in Difmap. Unlike Nagai et al. (2010), we adopted only circular Gaussian model components, not elliptical one, to the visibility data of each epoch in order to avoid extremely elongated components and to facilitate comparison of the features and their identification (e.g., Kudryavtseva et al., 2011). We judged the goodness of the fit from relative χ^2 statistic (Eq. (2.4)).

Resultant images for the epochs before 2010 December were well represented by three major components (C1, C2, and C3; shown in § 3.1), which were the same components as identified in Nagai et al. (2013). In addition to these three components, there was an additional emission bridging between C1 and C3, for the epochs after 2010 December. This additional emission was also detected in 43 GHz VERA observations for eight epochs between 2009 and 2011 (Nagai et al., 2012). Then, we modeled this bridging emission by using a circular Gaussian component (C4) for the epochs after 2010 December. The choice of 3 or 4 components was verified by *F*-test across all epochs.

2.4 Positional Accuracy

It is important to check the positional accuracy for studying the detailed kinematics. In the same manner as Suzuki et al. (2012), we estimated the C3 positional errors by examining the scatters in the C3 positions with reference to the optically thick component C1 in images between two close epochs (within 30 days separation), such that the source structures are approximately the same in both epochs. Assuming that the apparent motion of C3 is $0.5c$, this motion will show 0.036 mas positional change (< 0.05 of typical VERA 22 GHz beam) within 30 days. We have analyzed 60 pairs of images which are listed in Table 2.3.

Figure 2.4 shows the differences of relative positions of C3 with respect to C1 for these 60 pairs. Each data point in Figure 2.4 is normalized with the beam size averaged between the pair (θ_B^{mean}). The unbiased standard deviations of sample along right ascension ($\sigma_s^{\text{R.A.}}$) and declination ($\sigma_s^{\text{Decl.}}$) normalized by θ_B^{mean} are 0.035 and 0.069, respectively. As shown in Figure 2.4, we can regard histograms of the difference of C3 position as normally-distributed, since the most bins of histograms are covered by the normal distribution functions, especially in the tails of the distributions. Thus, assuming that each point in Figure 2.4 is normally-distributed, the $100(1 - \alpha)\%$ confidence interval of the standard deviation of population for statistical ensemble i , σ_p^i , is estimated from N samples of statistical ensemble i as

$$\frac{(N-1)\sigma_s^{i2}}{\chi_{N-1}^2(\alpha/2)} \leq \sigma_p^i \leq \frac{(N-1)\sigma_s^{i2}}{\chi_{N-1}^2(1-\alpha/2)}, \quad (2.7)$$

where $\chi_{N-1}^2(\alpha)$ is χ^2 statistic for degrees of freedom (dof) = $N - 1$ on which the event $\chi^2 \geq \chi_{N-1}^2$ happens with probability α . We apply this estimator for right ascension ensemble ($i = \text{R.A.}$) and declination ensemble ($i = \text{Decl.}$). Given $N = 60$ and $\alpha = 0.05$, the standard deviation of population for both right ascension ($\sigma_p^{\text{R.A.}}$) and declination ($\sigma_p^{\text{Decl.}}$) is estimated to be

$$0.030 \leq \sigma_p^{\text{R.A.}} \leq 0.043, \quad (2.8)$$

$$0.059 \leq \sigma_p^{\text{Decl.}} \leq 0.085. \quad (2.9)$$

Hereafter, the positional accuracy of C3 is conservatively set as $0.043\theta_{\text{beam}}$ for right ascension and $0.085\theta_{\text{beam}}$ for declination, where θ_{beam} is the beam size averaged for the major-minor axis on each epoch. In the same way as mentioned above, the positional errors of C2 and C4 are estimated (see also Figure 2.5 and 2.6). We set the positional accuracy of C2 as $0.14\theta_{\text{beam}}$ for right ascension and $0.13\theta_{\text{beam}}$ for declination, and that of C4 as $0.077\theta_{\text{beam}}$ for right ascension and $0.082\theta_{\text{beam}}$ for declination.

Table 2.3. Dispersions of C3 position with reference to C1.

Pairs	θ_B^{mean} (mas)	$\Delta\text{R.A.}$ (beam)	$\Delta\text{Decl.}$ (beam)
(1)	(2)	(3)	(3)
2007 Oct. 24/2007 Nov. 20	1.01	-0.005	0.022
2008 Feb. 4/2008 Mar. 3	0.99	-0.081	-0.008
2010 Nov. 28/2010 Nov. 29	1.04	0.100	-0.032
2010 Nov. 29/2010 Dec. 4	1.05	-0.006	0.015
2011 Jan. 11/2011 Jan. 29	0.99	0.098	0.017
2011 Jan. 29/2011 Feb. 3	1.01	-0.134	-0.125
2011 Feb. 3/2011 Feb. 12	1.05	0.067	0.097
2011 Apr. 21/2011 May. 18	0.99	-0.006	-0.013
2011 Aug. 16/2011 Sep. 12	0.96	-0.052	-0.029
2011 Sep. 12/2011 Sep. 13	1.04	-0.107	-0.114
2011 Sep. 13/2011 Sep. 14	1.08	0.130	-0.005
2011 Oct. 16/2011 Oct. 17	1.01	-0.081	0.021
2011 Oct. 17/2011 Nov. 7	1.03	0.061	0.006
2011 Nov. 7/2011 Nov. 20	1.01	0.003	-0.007
2011 Dec. 24/2012 Jan. 17	1.01	-0.031	0.065
2012 Jan. 17/2012 Jan. 18	1.02	-0.065	-0.045
2012 Jan. 18/2012 Jan. 21	1.00	0.258	-0.175
2012 Jan. 21/2012 Jan. 22	1.00	-0.126	0.190
2012 Jan. 22/2012 Jan. 29	1.01	-0.103	0.017
2012 Jan. 29/2012 Feb. 10	1.00	0.084	-0.084
2012 Feb. 10/2012 Feb. 19	1.01	0.002	0.009
2012 Feb. 19/2012 Mar. 9	1.02	-0.018	0.124
2012 Mar. 9/2012 Mar. 19	0.99	-0.027	-0.217
2012 Mar. 19/2012 Apr. 4	0.99	-0.145	0.190
2012 Apr. 4/2012 Apr. 8	1.03	-0.015	0.022
2012 Apr. 8/2012 Apr. 13	1.01	0.153	-0.119
2012 Apr. 13/2012 Apr. 26	1.02	-0.009	0.088
2012 Apr. 26/2012 Apr. 30	1.03	-0.100	0.023
2012 Apr. 30/2012 May. 14	1.02	0.305	-0.221
2012 May. 14/2012 May. 16	0.98	-0.305	0.254
2012 May. 16/2012 Jun. 1	0.95	0.035	-0.083
2012 Jun. 1/2012 Jun. 4	0.98	-0.011	0.025
2012 Jul. 28/2012 Aug. 14	1.00	-0.055	0.070
2012 Aug. 14/2012 Aug. 27	1.04	-0.106	0.012
2012 Aug. 27/2012 Sep. 7	1.03	0.144	-0.114
2012 Sep. 7/2012 Sep. 10	1.00	-0.030	0.007
2012 Sep. 10/2012 Sep. 21	1.01	0.111	0.114
2012 Sep. 21/2012 Sep. 23	1.01	-0.057	-0.117
2012 Sep. 23/2012 Oct. 1	1.02	0.052	-0.187
2013 Jan. 15/2013 Jan. 29	1.02	0.054	-0.109
2013 Jan. 29/2013 Jan. 30	0.98	-0.058	0.146
2013 Jan. 30/2013 Feb. 1	0.96	0.082	-0.196
2013 Feb. 1/2013 Feb. 4	0.98	-0.100	0.200
2013 Feb. 4/2013 Feb. 15	1.03	0.035	-0.169

Table 2.3. Dispersions of C3 position with reference to C1.

Pairs	θ_B^{mean} (mas)	$\Delta\text{R.A.}$ (beam)	$\Delta\text{Decl.}$ (beam)
(1)	(2)	(3)	(3)
2013 Feb. 15/2013 Mar. 10	1.04	0.228	0.010
2013 Mar. 10/2013 Mar. 15	1.00	-0.239	0.028
2013 Mar. 15/2013 Mar. 22	1.00	-0.143	0.133
2013 Mar. 22/2013 Mar. 25	1.02	-0.010	0.020
2013 Mar. 25/2013 Apr. 1	1.03	0.191	-0.042
2013 Apr. 1/2013 Apr. 17	1.01	0.032	0.023
2013 Apr. 17/2013 Apr. 29	1.03	-0.100	-0.064
2013 Apr. 29/2013 Apr. 30	0.98	0.080	0.059
2013 Apr. 30/2013 May. 26	0.93	-0.146	-0.011
2013 Aug. 17/2013 Aug. 22	0.99	0.057	-0.030
2013 Aug. 22/2013 Sep. 10	0.99	0.050	-0.192
2013 Sep. 10/2013 Sep. 16	1.01	-0.202	0.191
2013 Sep. 16/2013 Oct. 10	1.01	0.047	0.067
2013 Oct. 10/2013 Oct. 12	1.01	-0.082	-0.027
2013 Oct. 12/2013 Nov. 2	1.00	0.095	-0.016
2013 Nov. 2/2013 Nov. 8	0.97	-0.031	-0.009

Notes.

- (1) Pairs of adjacent epochs with their separation ≤ 30 days (for which the motion of components are negligible).
- (2) Beam sizes averaged for the major-minor axis and two epochs.
- (3) Differences of relative positions in right ascension and declination of C3 with reference to C1 between two epochs. These are normalized by θ_B^{mean} .

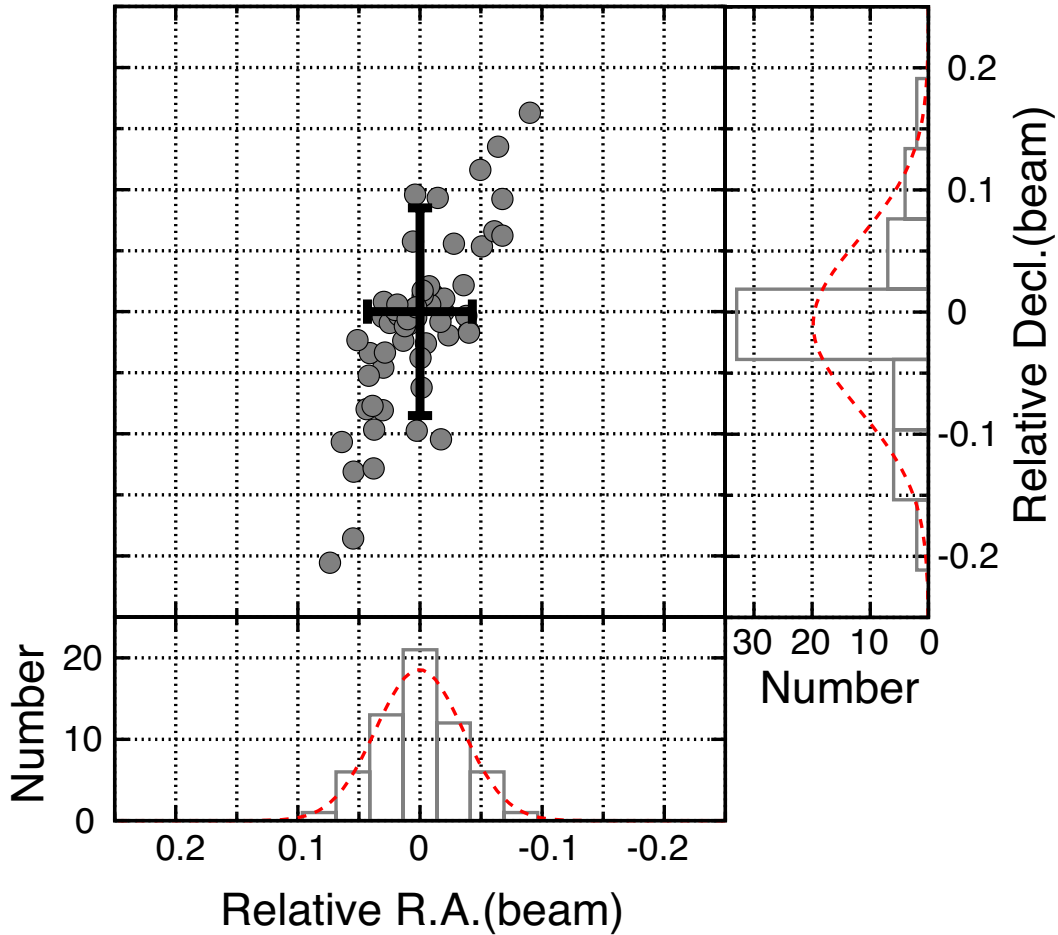


Figure 2.4. Estimation of positional error for C3. Each point represents the difference of C3 position with reference to C1 measured between two epochs closely separated in time (within 30 days). These are normalized by the beam size averaged between the pair. Thick bars correspond to the positional error for right ascension and declination direction, and are estimated to be $0.043\theta_{\text{beam}}$ and $0.085\theta_{\text{beam}}$, respectively. Histograms of the difference of C3 position are shown along each axis. Red dashed lines represents normal distribution functions with the means and unbiased standard deviations of samples along each axis. Areas of under the normal distribution functions correspond to those of the histograms.

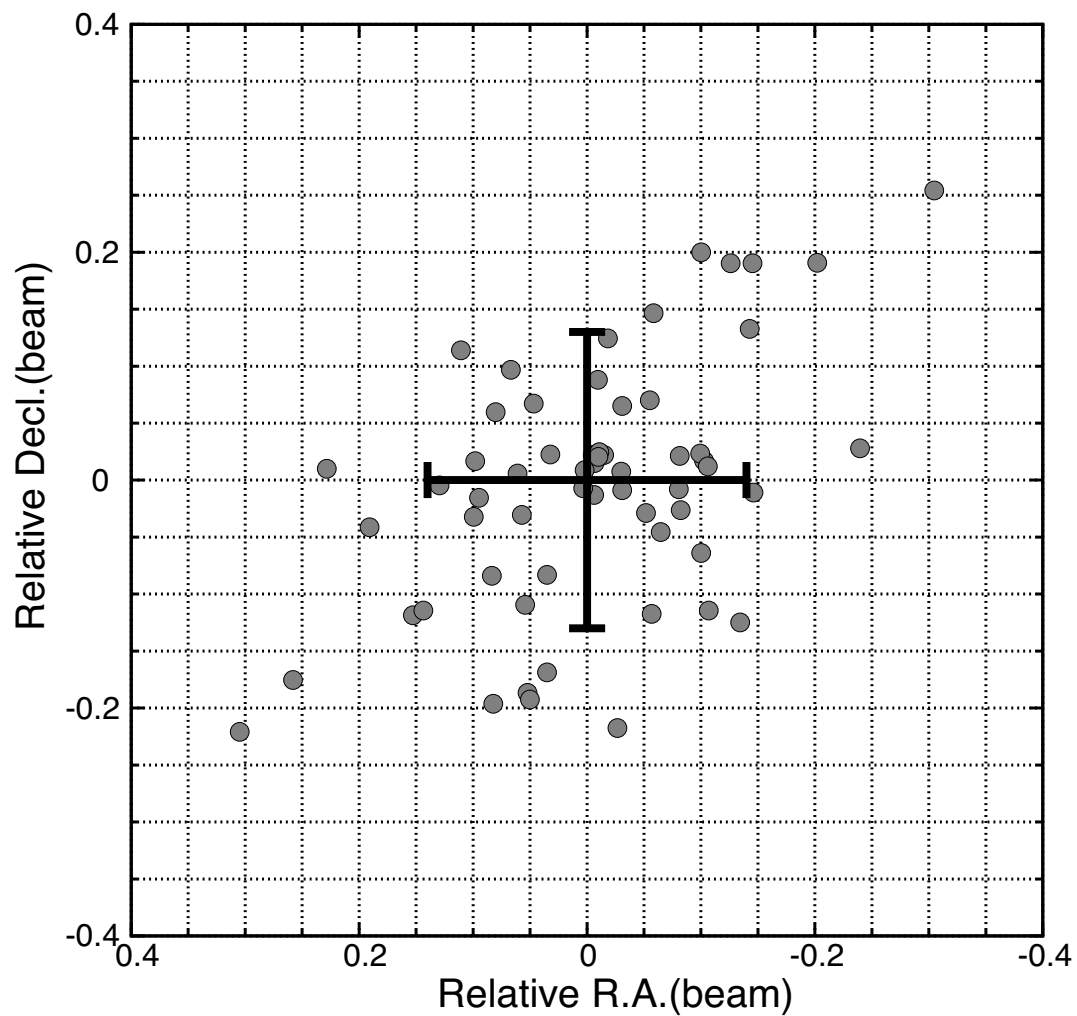


Figure 2.5. Same as Figure 2.4, but for C2. Thick bars correspond to the positional error for right ascension and declination direction, and are estimated to be $0.14\theta_{\text{beam}}$ and $0.13\theta_{\text{beam}}$, respectively.

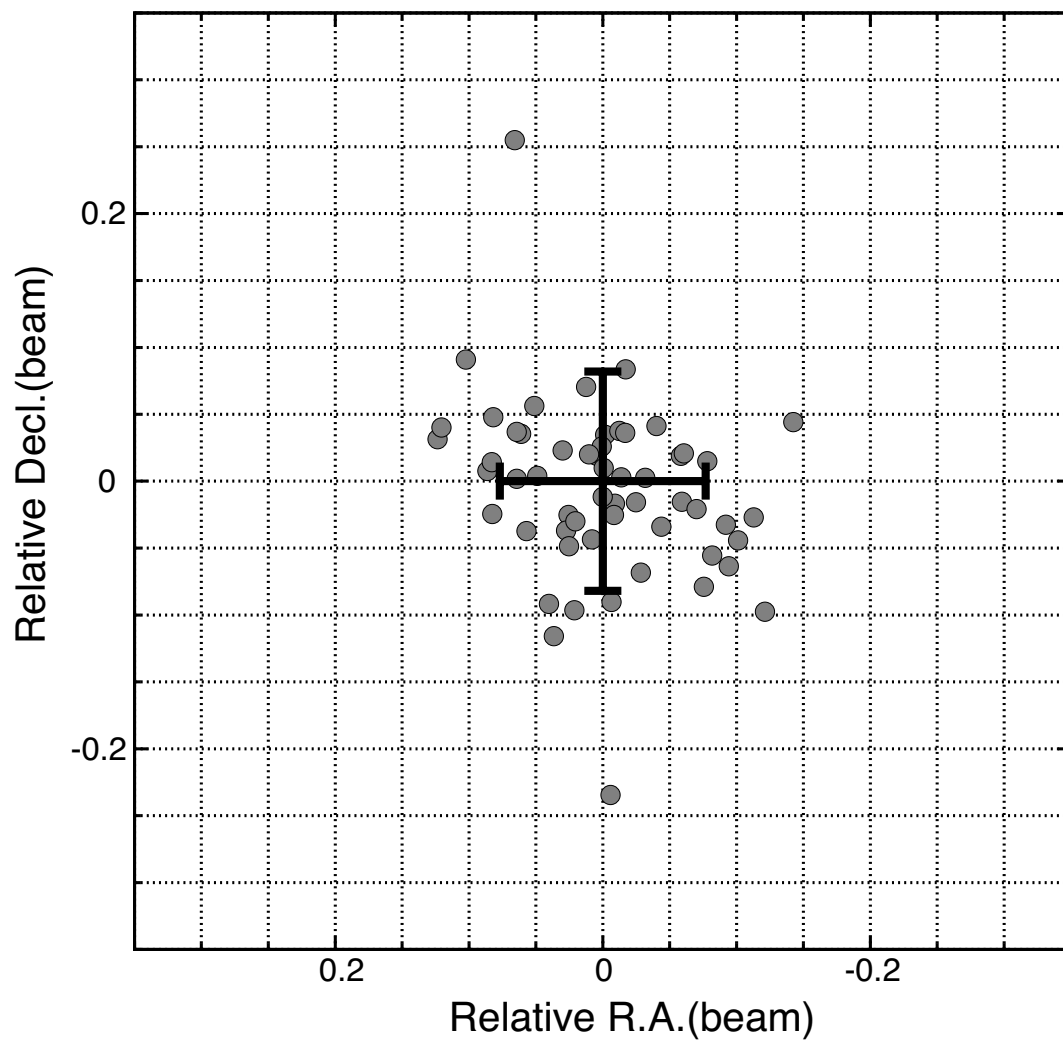


Figure 2.6. Same as Figure 2.4, but for C4. Thick bars correspond to the positional error for right ascension and declination direction, and are estimated to be $0.077\theta_{\text{beam}}$ and $0.082\theta_{\text{beam}}$, respectively.

3

Results

3.1 Total Intensity Image

Figure 3.1 shows the self-calibrated image of 3C 84 on 2013 December 20 (Modified Julian Date (MJD) 56646). As described in § 2.3, the subparsec-scale structure in 3C 84 can be represented by 3 (4) circular Gaussian components for the epochs before (after) 2010 December. Due to a lack of short baselines, we only detected the structure within ~ 3 mas from the phase tracking center, but we missed extended structures. The jet extends southward from the northern bright core component C1. C2 is ~ 1.6 mas away from C1, and its position angle relative to C1 (from north to east) is ~ 218 deg on 2013 December 20. C3 and C4 are located at ~ 2.2 mas, ~ 179 deg and ~ 1.3 mas, ~ 167 deg relative to C1, respectively. No counter jet component is detected with a level of 3σ throughout all epochs. Physical parameters of all fitted components over 80 epochs are listed in Table 3.1, 3.2, and 3.3.

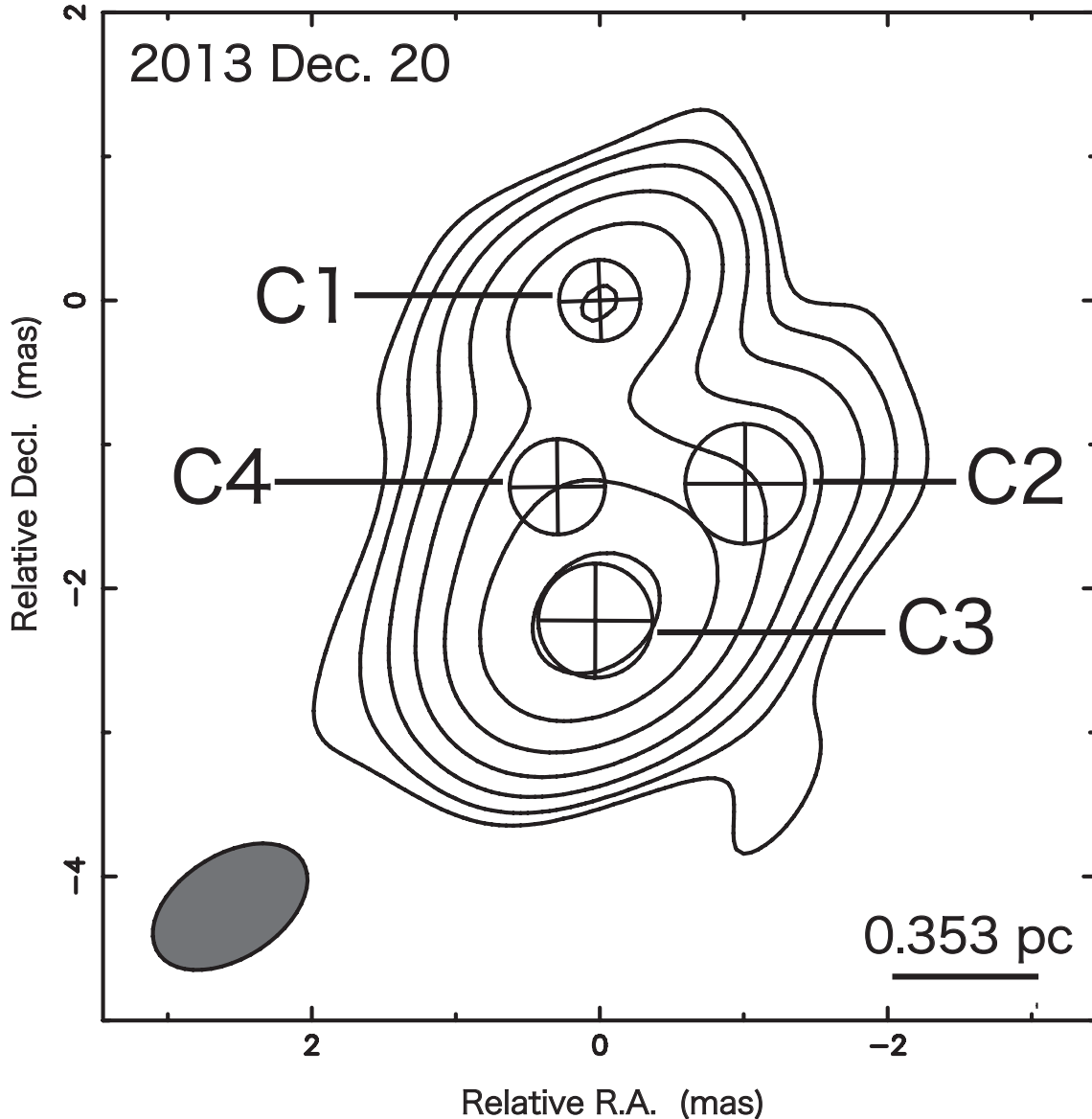


Figure 3.1. 22 GHz total intensity image of 3C 84 on 2013 December 20 (MJD 56646) with circular Gaussian components imposed. The diameters of these circular components represent the full width at the half maximum (FWHM) sizes of the individual fitted Gaussian components. The ellipse shown at the bottom left corner of the image indicates the FWHM of the convolved beam. The FWHM of the convolved beam is 1.19×0.72 mas at the position angle of -57.6 deg. The contours are plotted at the level of $3\sigma \times 2^n$ ($n = 0, 1, 2, 3, \dots$), where σ is image noise rms of $40.6 \text{ mJy beam}^{-1}$. The thick bar at the bottom right corner corresponds to 0.353 pc .

Table 3.1. Relative positions from C1.

Epoch	C2		C3		C4	
	Δ R.A.	Δ Decl.	Δ R.A.	Δ Decl.	Δ R.A.	Δ Decl.
	(mas) (1)	(mas) (1)	(mas) (2)	(mas) (2)	(mas) (3)	(mas) (3)
2007 Oct. 24	-0.701 ± 0.145	-1.276 ± 0.136	0.002 ± 0.044	-0.827 ± 0.087
2007 Nov. 20	-0.706 ± 0.141	-1.253 ± 0.132	0.033 ± 0.043	-0.874 ± 0.085
2007 Dec. 27	-0.646 ± 0.138	-1.246 ± 0.130	0.042 ± 0.042	-0.879 ± 0.083
2008 Feb. 4	-0.584 ± 0.145	-1.294 ± 0.136	0.072 ± 0.044	-0.886 ± 0.087
2008 Mar. 3	-0.664 ± 0.136	-1.302 ± 0.127	0.032 ± 0.042	-0.902 ± 0.082
2008 Apr. 15	-0.631 ± 0.146	-1.294 ± 0.137	0.054 ± 0.045	-0.928 ± 0.088
2008 May. 20	-0.656 ± 0.148	-1.285 ± 0.138	0.047 ± 0.045	-0.950 ± 0.089
2009 Feb. 19	-0.608 ± 0.137	-1.327 ± 0.128	0.109 ± 0.042	-1.084 ± 0.082
2009 May. 17	-0.541 ± 0.145	-1.332 ± 0.136	0.095 ± 0.045	-1.114 ± 0.087
2009 Sep. 23	-0.685 ± 0.144	-1.343 ± 0.135	0.082 ± 0.044	-1.163 ± 0.087
2009 Nov. 2	-0.601 ± 0.138	-1.319 ± 0.129	0.121 ± 0.042	-1.172 ± 0.083
2010 Feb. 8	-0.642 ± 0.139	-1.308 ± 0.131	0.142 ± 0.043	-1.243 ± 0.084
2010 Nov. 28	-0.873 ± 0.142	-1.242 ± 0.133	0.115 ± 0.043	-1.396 ± 0.085
2010 Nov. 29	-0.769 ± 0.151	-1.276 ± 0.142	0.147 ± 0.046	-1.400 ± 0.091
2010 Dec. 4	-0.776 ± 0.144	-1.260 ± 0.135	0.152 ± 0.044	-1.398 ± 0.087	0.678 ± 0.079	-0.713 ± 0.083
2011 Jan. 11	-0.899 ± 0.140	-1.236 ± 0.131	0.118 ± 0.043	-1.430 ± 0.084	0.366 ± 0.077	-0.525 ± 0.081
2011 Jan. 29	-0.802 ± 0.139	-1.219 ± 0.130	0.182 ± 0.042	-1.523 ± 0.083	0.360 ± 0.076	-0.614 ± 0.080
2011 Feb. 3	-0.938 ± 0.146	-1.345 ± 0.137	0.113 ± 0.045	-1.542 ± 0.088	0.354 ± 0.080	-0.851 ± 0.085
2011 Feb. 12	-0.868 ± 0.141	-1.243 ± 0.132	0.117 ± 0.043	-1.441 ± 0.085	0.423 ± 0.077	-0.583 ± 0.081
2011 Apr. 21	-0.783 ± 0.139	-1.340 ± 0.130	0.166 ± 0.043	-1.632 ± 0.084	0.192 ± 0.076	-0.478 ± 0.081
2011 May. 18	-0.790 ± 0.139	-1.353 ± 0.130	0.162 ± 0.043	-1.658 ± 0.084	0.200 ± 0.076	-0.521 ± 0.080
2011 Aug. 16	-0.692 ± 0.131	-1.262 ± 0.122	0.125 ± 0.040	-1.696 ± 0.078	0.278 ± 0.071	-0.830 ± 0.076
2011 Sep. 12	-0.742 ± 0.141	-1.290 ± 0.132	0.060 ± 0.043	-1.607 ± 0.085	0.290 ± 0.077	-0.762 ± 0.082
2011 Sep. 13	-0.853 ± 0.140	-1.409 ± 0.131	0.136 ± 0.043	-1.820 ± 0.084	0.172 ± 0.076	-0.790 ± 0.081
2011 Sep. 14	-0.713 ± 0.140	-1.414 ± 0.131	0.163 ± 0.043	-1.830 ± 0.084	0.212 ± 0.076	-0.915 ± 0.081
2011 Oct. 16	-0.821 ± 0.138	-1.230 ± 0.129	0.111 ± 0.042	-1.711 ± 0.083	0.294 ± 0.076	-0.867 ± 0.080
2011 Oct. 17	-0.904 ± 0.137	-1.209 ± 0.128	0.095 ± 0.042	-1.702 ± 0.082	0.292 ± 0.075	-0.833 ± 0.079
2011 Nov. 7	-0.841 ± 0.144	-1.203 ± 0.135	0.094 ± 0.044	-1.741 ± 0.086	0.314 ± 0.079	-0.932 ± 0.083
2011 Nov. 20	-0.838 ± 0.141	-1.210 ± 0.132	0.104 ± 0.043	-1.751 ± 0.085	0.340 ± 0.077	-0.958 ± 0.082
2011 Dec. 24	-0.869 ± 0.141	-1.170 ± 0.132	0.079 ± 0.043	-1.817 ± 0.085	0.317 ± 0.077	-0.982 ± 0.082
2012 Jan. 17	-0.900 ± 0.137	-1.105 ± 0.128	0.068 ± 0.042	-1.804 ± 0.082	0.347 ± 0.075	-0.959 ± 0.079
2012 Jan. 18	-0.966 ± 0.145	-1.151 ± 0.136	0.082 ± 0.044	-1.828 ± 0.087	0.302 ± 0.079	-0.994 ± 0.084
2012 Jan. 21	-0.707 ± 0.139	-1.327 ± 0.130	0.146 ± 0.043	-1.935 ± 0.084	0.262 ± 0.076	-0.952 ± 0.081
2012 Jan. 22	-0.833 ± 0.136	-1.137 ± 0.127	0.082 ± 0.042	-1.800 ± 0.082	0.344 ± 0.074	-0.977 ± 0.079
2012 Jan. 29	-0.936 ± 0.136	-1.120 ± 0.127	0.059 ± 0.042	-1.819 ± 0.082	0.286 ± 0.074	-0.957 ± 0.079
2012 Feb. 10	-0.853 ± 0.141	-1.204 ± 0.132	0.089 ± 0.043	-1.900 ± 0.085	0.277 ± 0.077	-0.974 ± 0.082
2012 Feb. 19	-0.851 ± 0.137	-1.195 ± 0.128	0.095 ± 0.042	-1.843 ± 0.082	0.328 ± 0.075	-0.918 ± 0.079
2012 Mar. 9	-0.869 ± 0.144	-1.069 ± 0.135	0.075 ± 0.044	-1.842 ± 0.087	0.394 ± 0.079	-0.916 ± 0.083
2012 Mar. 19	-0.896 ± 0.144	-1.284 ± 0.135	0.129 ± 0.044	-2.027 ± 0.086	0.252 ± 0.079	-0.872 ± 0.083
2012 Apr. 4	-1.040 ± 0.137	-1.095 ± 0.129	0.040 ± 0.042	-1.865 ± 0.082	0.292 ± 0.075	-0.963 ± 0.079
2012 Apr. 8	-1.055 ± 0.145	-1.072 ± 0.136	0.035 ± 0.045	-1.855 ± 0.087	0.279 ± 0.079	-0.925 ± 0.084
2012 Apr. 13	-0.900 ± 0.143	-1.192 ± 0.134	0.090 ± 0.044	-1.987 ± 0.086	0.284 ± 0.078	-0.906 ± 0.083
2012 Apr. 26	-0.910 ± 0.149	-1.102 ± 0.140	0.040 ± 0.046	-1.868 ± 0.090	0.342 ± 0.082	-0.944 ± 0.086
2012 Apr. 30	-1.013 ± 0.142	-1.078 ± 0.133	0.030 ± 0.043	-1.853 ± 0.085	0.309 ± 0.078	-0.941 ± 0.082
2012 May. 14	-0.702 ± 0.146	-1.304 ± 0.136	0.075 ± 0.045	-1.934 ± 0.088	0.337 ± 0.080	-0.979 ± 0.084
2012 May. 16	-1.000 ± 0.131	-1.055 ± 0.122	0.025 ± 0.040	-1.882 ± 0.078	0.320 ± 0.071	-0.898 ± 0.076
2012 Jun. 1	-0.966 ± 0.139	-1.135 ± 0.130	0.042 ± 0.043	-1.884 ± 0.083	0.262 ± 0.076	-0.878 ± 0.080
2012 Jun. 4	-0.977 ± 0.141	-1.110 ± 0.132	0.045 ± 0.043	-1.889 ± 0.085	0.311 ± 0.077	-0.874 ± 0.082
2012 Jul. 28	-0.904 ± 0.136	-1.232 ± 0.128	0.043 ± 0.042	-1.883 ± 0.082	0.266 ± 0.075	-0.897 ± 0.079
2012 Aug. 14	-0.958 ± 0.145	-1.162 ± 0.136	0.026 ± 0.045	-1.891 ± 0.087	0.286 ± 0.080	-0.926 ± 0.084
2012 Aug. 27	-1.069 ± 0.148	-1.150 ± 0.139	0.005 ± 0.045	-1.880 ± 0.089	0.256 ± 0.081	-0.998 ± 0.086
2012 Sep. 7	-0.921 ± 0.141	-1.267 ± 0.132	0.047 ± 0.043	-1.914 ± 0.085	0.256 ± 0.077	-1.009 ± 0.081
2012 Sep. 10	-0.951 ± 0.144	-1.260 ± 0.135	0.039 ± 0.044	-1.908 ± 0.087	0.242 ± 0.079	-1.006 ± 0.083
2012 Sep. 21	-0.840 ± 0.137	-1.145 ± 0.128	0.031 ± 0.042	-1.887 ± 0.082	0.329 ± 0.075	-0.999 ± 0.079
2012 Sep. 23	-0.897 ± 0.144	-1.263 ± 0.134	0.044 ± 0.044	-1.899 ± 0.086	0.269 ± 0.078	-1.014 ± 0.083
2012 Oct. 1	-0.844 ± 0.140	-1.454 ± 0.131	0.082 ± 0.043	-1.998 ± 0.084	0.186 ± 0.076	-1.071 ± 0.081

Table 3.1. Relative positions from C1.

Epoch	C2		C3		C4	
	Δ R.A.	Δ Decl.	Δ R.A.	Δ Decl.	Δ R.A.	Δ Decl.
	(mas) (1)	(mas) (1)	(mas) (2)	(mas) (2)	(mas) (3)	(mas) (3)
2013 Jan. 15	-0.900 ± 0.147	-1.358 ± 0.138	0.052 ± 0.045	-1.993 ± 0.088	0.205 ± 0.080	-1.241 ± 0.085
2013 Jan. 29	-0.844 ± 0.140	-1.469 ± 0.131	0.094 ± 0.043	-2.047 ± 0.084	0.180 ± 0.077	-1.257 ± 0.081
2013 Jan. 30	-0.901 ± 0.131	-1.326 ± 0.123	0.067 ± 0.040	-1.992 ± 0.079	0.240 ± 0.072	-1.223 ± 0.076
2013 Feb. 1	-0.822 ± 0.141	-1.515 ± 0.132	0.104 ± 0.043	-2.066 ± 0.084	0.173 ± 0.077	-1.243 ± 0.081
2013 Feb. 4	-0.920 ± 0.144	-1.319 ± 0.135	0.090 ± 0.044	-1.975 ± 0.087	0.273 ± 0.079	-1.153 ± 0.084
2013 Feb. 15	-0.884 ± 0.150	-1.493 ± 0.140	0.093 ± 0.046	-2.075 ± 0.090	0.148 ± 0.082	-1.254 ± 0.087
2013 Mar. 10	-0.647 ± 0.139	-1.482 ± 0.130	0.122 ± 0.043	-2.110 ± 0.084	0.276 ± 0.076	-1.221 ± 0.080
2013 Mar. 15	-0.887 ± 0.136	-1.455 ± 0.127	0.087 ± 0.042	-2.088 ± 0.082	0.181 ± 0.074	-1.285 ± 0.079
2013 Mar. 22	-1.029 ± 0.142	-1.323 ± 0.133	0.026 ± 0.043	-2.023 ± 0.085	0.182 ± 0.077	-1.259 ± 0.082
2013 Mar. 25	-1.039 ± 0.146	-1.302 ± 0.136	0.024 ± 0.045	-2.009 ± 0.087	0.192 ± 0.080	-1.238 ± 0.084
2013 Apr. 1	-0.844 ± 0.134	-1.345 ± 0.126	0.076 ± 0.041	-2.033 ± 0.081	0.259 ± 0.073	-1.200 ± 0.078
2013 Apr. 17	-0.811 ± 0.144	-1.322 ± 0.135	0.038 ± 0.044	-2.037 ± 0.086	0.284 ± 0.079	-1.250 ± 0.083
2013 Apr. 29	-0.914 ± 0.147	-1.388 ± 0.138	0.058 ± 0.045	-2.036 ± 0.089	0.203 ± 0.081	-1.234 ± 0.085
2013 Apr. 30	-0.836 ± 0.133	-1.330 ± 0.124	0.087 ± 0.041	-2.028 ± 0.080	0.322 ± 0.073	-1.195 ± 0.077
2013 May. 26	-0.972 ± 0.133	-1.340 ± 0.125	0.050 ± 0.041	-2.044 ± 0.080	0.228 ± 0.073	-1.236 ± 0.077
2013 Aug. 17	-0.926 ± 0.140	-1.286 ± 0.131	0.043 ± 0.043	-2.088 ± 0.084	0.311 ± 0.077	-1.286 ± 0.081
2013 Aug. 22	-0.869 ± 0.138	-1.315 ± 0.130	0.053 ± 0.042	-2.094 ± 0.083	0.311 ± 0.076	-1.277 ± 0.080
2013 Sep. 10	-0.820 ± 0.140	-1.505 ± 0.131	0.091 ± 0.043	-2.221 ± 0.084	0.236 ± 0.076	-1.354 ± 0.081
2013 Sep. 16	-1.023 ± 0.141	-1.313 ± 0.132	0.023 ± 0.043	-2.158 ± 0.085	0.228 ± 0.077	-1.380 ± 0.082
2013 Oct. 10	-0.976 ± 0.140	-1.246 ± 0.131	0.020 ± 0.043	-2.140 ± 0.084	0.312 ± 0.077	-1.365 ± 0.081
2013 Oct. 12	-1.059 ± 0.143	-1.272 ± 0.134	0.019 ± 0.044	-2.203 ± 0.086	0.219 ± 0.078	-1.398 ± 0.083
2013 Nov. 2	-0.964 ± 0.137	-1.288 ± 0.129	0.022 ± 0.042	-2.199 ± 0.082	0.301 ± 0.075	-1.351 ± 0.079
2013 Nov. 8	-0.994 ± 0.141	-1.296 ± 0.132	0.040 ± 0.043	-2.194 ± 0.085	0.284 ± 0.077	-1.315 ± 0.082
2013 Dec. 20	-1.009 ± 0.134	-1.273 ± 0.126	0.031 ± 0.041	-2.224 ± 0.081	0.294 ± 0.074	-1.294 ± 0.078

Notes.

Positional error is estimated in § 2.4.

(1) Relative right ascension and declination between C1 and C2.

(2) Relative right ascension and declination between C1 and C3.

(3) Relative right ascension and declination between C1 and C4.

Table 3.2. FWHM size of fitted components.

Epoch	C1 (mas)	C2 (mas)	C3 (mas)	C4 (mas)
2007 Oct. 24	< 0.24	0.57 ± 0.52	0.42 ± 0.05	...
2007 Nov. 20	< 0.24	< 0.50	0.48 ± 0.05	...
2007 Dec. 27	< 0.23	0.65 ± 0.49	0.48 ± 0.05	...
2008 Feb. 4	< 0.24	0.67 ± 0.51	0.49 ± 0.05	...
2008 Mar. 3	< 0.23	0.51 ± 0.48	0.47 ± 0.05	...
2008 Apr. 15	< 0.24	< 0.52	0.39 ± 0.05	...
2008 May. 20	< 0.25	< 0.52	0.39 ± 0.05	...
2009 Feb. 19	0.27 ± 0.23	0.94 ± 0.49	0.70 ± 0.05	...
2009 May. 17	0.31 ± 0.24	0.87 ± 0.52	0.72 ± 0.05	...
2009 Sep. 23	0.31 ± 0.24	0.73 ± 0.51	0.80 ± 0.05	...
2009 Nov. 2	0.35 ± 0.23	0.82 ± 0.49	0.73 ± 0.05	...
2010 Feb. 8	0.24 ± 0.23	0.79 ± 0.50	0.69 ± 0.05	...
2010 Nov. 28	0.41 ± 0.24	0.58 ± 0.50	0.74 ± 0.05	...
2010 Nov. 29	0.25 ± 0.25	0.64 ± 0.54	0.66 ± 0.05	...
2010 Dec. 4	< 0.24	0.78 ± 0.51	0.67 ± 0.05	< 0.26
2011 Jan. 11	0.72 ± 0.23	0.72 ± 0.50	0.79 ± 0.05	< 0.25
2011 Jan. 29	0.35 ± 0.23	1.03 ± 0.49	0.77 ± 0.05	< 0.25

Table 3.2. FWHM size of fitted components.

Epoch	C1 (mas)	C2 (mas)	C3 (mas)	C4 (mas)
2011 Feb. 3	0.39 ± 0.24	< 0.52	0.78 ± 0.05	< 0.26
2011 Feb. 12	0.61 ± 0.24	0.80 ± 0.50	0.75 ± 0.05	< 0.25
2011 Apr. 21	0.39 ± 0.23	0.81 ± 0.49	0.76 ± 0.05	< 0.25
2011 May. 18	0.34 ± 0.23	0.81 ± 0.49	0.74 ± 0.05	< 0.25
2011 Aug. 16	0.23 ± 0.22	1.01 ± 0.46	0.62 ± 0.04	< 0.23
2011 Sep. 12	0.48 ± 0.24	< 0.50	0.76 ± 0.05	< 0.25
2011 Sep. 13	0.35 ± 0.23	< 0.50	0.69 ± 0.05	0.53 ± 0.25
2011 Sep. 14	0.37 ± 0.23	< 0.50	0.62 ± 0.05	0.48 ± 0.25
2011 Oct. 16	0.28 ± 0.23	0.95 ± 0.49	0.65 ± 0.05	< 0.25
2011 Oct. 17	0.44 ± 0.23	0.92 ± 0.49	0.69 ± 0.05	< 0.24
2011 Nov. 7	0.44 ± 0.24	0.91 ± 0.51	0.64 ± 0.05	< 0.26
2011 Nov. 20	0.40 ± 0.24	0.99 ± 0.50	0.61 ± 0.05	< 0.25
2011 Dec. 24	0.55 ± 0.24	0.86 ± 0.50	0.64 ± 0.05	0.32 ± 0.25
2012 Jan. 17	0.58 ± 0.23	0.86 ± 0.49	0.67 ± 0.05	< 0.24
2012 Jan. 18	0.62 ± 0.24	0.64 ± 0.51	0.63 ± 0.05	< 0.26
2012 Jan. 21	< 0.23	0.62 ± 0.49	0.66 ± 0.05	0.51 ± 0.25
2012 Jan. 22	0.59 ± 0.23	0.89 ± 0.48	0.67 ± 0.05	0.40 ± 0.24
2012 Jan. 29	0.59 ± 0.23	0.90 ± 0.48	0.70 ± 0.05	0.52 ± 0.24
2012 Feb. 10	0.52 ± 0.24	< 0.50	0.67 ± 0.05	< 0.25
2012 Feb. 19	0.45 ± 0.23	0.79 ± 0.49	0.66 ± 0.05	< 0.24
2012 Mar. 9	0.59 ± 0.24	0.93 ± 0.51	0.73 ± 0.05	0.28 ± 0.26
2012 Mar. 19	0.58 ± 0.24	< 0.51	0.77 ± 0.05	0.71 ± 0.26
2012 Apr. 4	0.77 ± 0.23	0.81 ± 0.49	0.73 ± 0.05	0.52 ± 0.24
2012 Apr. 8	0.71 ± 0.24	0.84 ± 0.52	0.72 ± 0.05	0.42 ± 0.26
2012 Apr. 13	0.54 ± 0.24	< 0.51	0.75 ± 0.05	0.43 ± 0.26
2012 Apr. 26	0.58 ± 0.25	0.91 ± 0.53	0.69 ± 0.05	< 0.27
2012 Apr. 30	0.63 ± 0.24	0.89 ± 0.50	0.67 ± 0.05	< 0.25
2012 May. 14	0.32 ± 0.24	0.81 ± 0.52	0.64 ± 0.05	< 0.26
2012 May. 16	0.63 ± 0.22	0.86 ± 0.46	0.71 ± 0.04	< 0.23
2012 Jun. 1	0.59 ± 0.23	0.79 ± 0.49	0.71 ± 0.05	< 0.25
2012 Jun. 4	0.58 ± 0.24	0.87 ± 0.50	0.73 ± 0.05	< 0.25
2012 Jul. 28	0.51 ± 0.23	0.85 ± 0.48	0.72 ± 0.05	< 0.24
2012 Aug. 14	0.49 ± 0.24	0.91 ± 0.52	0.73 ± 0.05	< 0.26
2012 Aug. 27	0.59 ± 0.25	0.91 ± 0.53	0.70 ± 0.05	< 0.26
2012 Sep. 7	0.57 ± 0.24	0.79 ± 0.50	0.71 ± 0.05	0.44 ± 0.25
2012 Sep. 10	0.55 ± 0.24	0.75 ± 0.51	0.71 ± 0.05	0.42 ± 0.26
2012 Sep. 21	0.54 ± 0.23	0.86 ± 0.49	0.74 ± 0.05	< 0.24
2012 Sep. 23	0.42 ± 0.24	0.81 ± 0.51	0.68 ± 0.05	< 0.26
2012 Oct. 1	< 0.23	< 0.50	0.68 ± 0.05	0.62 ± 0.25
2013 Jan. 15	0.49 ± 0.25	0.73 ± 0.52	0.64 ± 0.05	0.58 ± 0.26
2013 Jan. 29	< 0.23	< 0.50	0.63 ± 0.05	0.65 ± 0.25
2013 Jan. 30	0.39 ± 0.22	0.71 ± 0.47	0.62 ± 0.05	0.49 ± 0.23
2013 Feb. 1	< 0.24	< 0.50	0.66 ± 0.05	0.62 ± 0.25
2013 Feb. 4	0.34 ± 0.24	1.02 ± 0.51	0.68 ± 0.05	0.53 ± 0.26
2013 Feb. 15	< 0.25	< 0.53	0.65 ± 0.05	0.69 ± 0.27
2013 Mar. 10	< 0.23	0.80 ± 0.49	0.63 ± 0.05	0.42 ± 0.25

Table 3.2. FWHM size of fitted components.

Epoch	C1 (mas)	C2 (mas)	C3 (mas)	C4 (mas)
2013 Mar. 15	< 0.23	< 0.48	0.65 ± 0.05	0.67 ± 0.24
2013 Mar. 22	0.55 ± 0.24	0.72 ± 0.50	0.67 ± 0.05	0.63 ± 0.25
2013 Mar. 25	0.52 ± 0.24	0.76 ± 0.52	0.67 ± 0.05	0.58 ± 0.26
2013 Apr. 1	0.30 ± 0.22	0.60 ± 0.48	0.68 ± 0.05	0.50 ± 0.24
2013 Apr. 17	0.66 ± 0.24	0.74 ± 0.51	0.74 ± 0.05	0.59 ± 0.26
2013 Apr. 29	0.47 ± 0.25	0.67 ± 0.52	0.67 ± 0.05	0.54 ± 0.26
2013 Apr. 30	0.41 ± 0.22	0.92 ± 0.47	0.71 ± 0.05	0.47 ± 0.24
2013 May. 26	0.49 ± 0.22	0.69 ± 0.47	0.68 ± 0.05	0.54 ± 0.24
2013 Aug. 17	0.53 ± 0.23	0.76 ± 0.50	0.69 ± 0.05	0.51 ± 0.25
2013 Aug. 22	0.51 ± 0.23	0.79 ± 0.49	0.70 ± 0.05	0.55 ± 0.25
2013 Sep. 10	0.24 ± 0.23	< 0.50	0.69 ± 0.05	0.69 ± 0.25
2013 Sep. 16	0.60 ± 0.24	0.76 ± 0.50	0.68 ± 0.05	0.72 ± 0.25
2013 Oct. 10	0.56 ± 0.23	0.79 ± 0.50	0.66 ± 0.05	0.58 ± 0.25
2013 Oct. 12	0.59 ± 0.24	0.63 ± 0.51	0.70 ± 0.05	0.78 ± 0.25
2013 Nov. 2	0.65 ± 0.23	0.79 ± 0.49	0.74 ± 0.05	0.75 ± 0.24
2013 Nov. 8	0.60 ± 0.24	0.59 ± 0.50	0.72 ± 0.05	0.73 ± 0.25
2013 Dec. 20	0.57 ± 0.23	0.83 ± 0.48	0.79 ± 0.05	0.66 ± 0.24

Notes.

Error is 1σ level, and estimated in the same way as the estimation of positional error (see § 2.4). The upper limit is estimated at 1σ level.

Table 3.3. Flux of fitted components.

Epoch	C1 (Jy)	C2 (Jy)	C3 (Jy)	C4 (Jy)
2007 Oct. 24	2.66 ± 0.27	2.13 ± 0.21	3.60 ± 0.36	...
2007 Nov. 20	2.94 ± 0.29	2.14 ± 0.21	4.83 ± 0.48	...
2007 Dec. 27	3.11 ± 0.31	2.81 ± 0.28	4.53 ± 0.45	...
2008 Feb. 4	2.85 ± 0.29	2.75 ± 0.28	4.29 ± 0.43	...
2008 Mar. 3	2.70 ± 0.27	2.05 ± 0.21	4.28 ± 0.43	...
2008 Apr. 15	3.34 ± 0.33	2.51 ± 0.25	4.75 ± 0.48	...
2008 May. 20	3.54 ± 0.35	2.49 ± 0.25	5.01 ± 0.50	...
2009 Feb. 19	3.80 ± 0.38	2.89 ± 0.29	7.03 ± 0.70	...
2009 May. 17	4.49 ± 0.45	3.33 ± 0.33	7.34 ± 0.73	...
2009 Sep. 23	4.42 ± 0.44	2.53 ± 0.25	8.00 ± 0.80	...
2009 Nov. 2	4.41 ± 0.44	3.42 ± 0.34	6.95 ± 0.70	...
2010 Feb. 8	4.14 ± 0.41	3.21 ± 0.32	7.14 ± 0.71	...
2010 Nov. 28	4.60 ± 0.46	1.81 ± 0.18	10.31 ± 1.03	...
2010 Nov. 29	3.97 ± 0.40	2.10 ± 0.21	8.94 ± 0.89	...
2010 Dec. 4	4.21 ± 0.42	2.72 ± 0.27	9.61 ± 0.96	0.03 ± 0.003
2011 Jan. 11	4.91 ± 0.49	1.90 ± 0.19	11.27 ± 1.13	0.17 ± 0.02
2011 Jan. 29	4.56 ± 0.46	3.33 ± 0.34	10.30 ± 1.03	0.31 ± 0.03
2011 Feb. 3	4.87 ± 0.49	1.33 ± 0.13	10.71 ± 1.07	0.16 ± 0.02
2011 Feb. 12	5.81 ± 0.58	2.52 ± 0.25	10.54 ± 1.05	0.36 ± 0.04
2011 Apr. 21	3.20 ± 0.32	2.51 ± 0.25	11.00 ± 1.10	2.17 ± 0.22
2011 May. 18	3.23 ± 0.32	2.46 ± 0.25	11.21 ± 1.12	2.18 ± 0.22

Table 3.3. Flux of fitted components.

Epoch	C1 (Jy)	C2 (Jy)	C3 (Jy)	C4 (Jy)
2011 Aug. 16	3.93 ± 0.39	3.74 ± 0.38	11.46 ± 1.15	2.05 ± 0.21
2011 Sep. 12	4.58 ± 0.46	1.27 ± 0.13	14.74 ± 1.47	0.91 ± 0.09
2011 Sep. 13	3.76 ± 0.38	1.29 ± 0.13	13.27 ± 1.33	3.06 ± 0.31
2011 Sep. 14	4.33 ± 0.43	1.99 ± 0.20	12.04 ± 1.20	3.08 ± 0.31
2011 Oct. 16	3.88 ± 0.39	2.88 ± 0.29	13.15 ± 1.32	1.91 ± 0.19
2011 Oct. 17	4.62 ± 0.46	2.72 ± 0.27	14.70 ± 1.47	1.80 ± 0.18
2011 Nov. 7	4.66 ± 0.47	2.97 ± 0.30	14.07 ± 1.41	2.15 ± 0.22
2011 Nov. 20	4.49 ± 0.45	3.22 ± 0.32	14.00 ± 1.40	2.07 ± 0.21
2011 Dec. 24	5.07 ± 0.51	2.62 ± 0.26	14.57 ± 1.46	2.28 ± 0.23
2012 Jan. 17	5.64 ± 0.56	2.47 ± 0.25	16.17 ± 1.62	2.04 ± 0.20
2012 Jan. 18	5.67 ± 0.57	1.65 ± 0.17	15.11 ± 1.51	2.02 ± 0.20
2012 Jan. 21	3.51 ± 0.35	2.32 ± 0.23	14.79 ± 1.48	3.43 ± 0.34
2012 Jan. 22	5.11 ± 0.51	2.76 ± 0.28	14.71 ± 1.47	2.37 ± 0.24
2012 Jan. 29	4.77 ± 0.48	2.60 ± 0.26	14.28 ± 1.43	2.64 ± 0.26
2012 Feb. 10	4.53 ± 0.45	1.44 ± 0.14	15.07 ± 1.51	2.36 ± 0.24
2012 Feb. 19	4.37 ± 0.44	2.02 ± 0.20	15.39 ± 1.54	1.95 ± 0.20
2012 Mar. 9	5.03 ± 0.50	2.40 ± 0.24	16.35 ± 1.64	2.15 ± 0.22
2012 Mar. 19	3.80 ± 0.38	1.40 ± 0.14	17.24 ± 1.72	4.32 ± 0.43
2012 Apr. 4	6.77 ± 0.68	2.09 ± 0.21	16.85 ± 1.69	2.88 ± 0.29
2012 Apr. 8	6.19 ± 0.62	2.18 ± 0.22	17.74 ± 1.77	2.60 ± 0.26
2012 Apr. 13	4.09 ± 0.41	1.23 ± 0.12	17.76 ± 1.78	3.03 ± 0.30
2012 Apr. 26	5.71 ± 0.57	2.52 ± 0.25	17.62 ± 1.76	2.28 ± 0.23
2012 Apr. 30	6.16 ± 0.62	2.29 ± 0.23	17.75 ± 1.78	2.24 ± 0.22
2012 May. 14	4.13 ± 0.41	2.52 ± 0.25	15.56 ± 1.56	2.37 ± 0.24
2012 May. 16	5.83 ± 0.58	2.20 ± 0.23	18.26 ± 1.83	2.22 ± 0.22
2012 Jun. 1	5.59 ± 0.56	1.88 ± 0.19	17.62 ± 1.76	2.24 ± 0.22
2012 Jun. 4	5.34 ± 0.53	2.08 ± 0.21	17.16 ± 1.72	2.19 ± 0.22
2012 Jul. 28	5.00 ± 0.50	2.28 ± 0.23	16.23 ± 1.62	2.25 ± 0.23
2012 Aug. 14	4.88 ± 0.49	2.33 ± 0.23	16.97 ± 1.70	2.31 ± 0.23
2012 Aug. 27	5.60 ± 0.56	2.24 ± 0.22	15.85 ± 1.59	2.23 ± 0.22
2012 Sep. 7	5.42 ± 0.54	2.18 ± 0.22	16.40 ± 1.64	2.94 ± 0.29
2012 Sep. 10	5.19 ± 0.52	1.92 ± 0.19	16.14 ± 1.61	2.82 ± 0.28
2012 Sep. 21	5.25 ± 0.53	2.41 ± 0.24	17.44 ± 1.74	2.32 ± 0.23
2012 Sep. 23	4.73 ± 0.47	2.32 ± 0.23	16.07 ± 1.61	2.34 ± 0.23
2012 Oct. 1	3.76 ± 0.38	1.53 ± 0.15	15.76 ± 1.58	4.14 ± 0.41
2013 Jan. 15	4.50 ± 0.45	2.35 ± 0.24	13.80 ± 1.38	4.47 ± 0.45
2013 Jan. 29	3.80 ± 0.38	1.99 ± 0.20	14.76 ± 1.48	5.34 ± 0.53
2013 Jan. 30	4.38 ± 0.44	2.30 ± 0.23	15.32 ± 1.53	4.18 ± 0.42
2013 Feb. 1	3.51 ± 0.35	1.64 ± 0.16	15.15 ± 1.52	4.66 ± 0.47
2013 Feb. 4	3.81 ± 0.38	3.38 ± 0.34	15.28 ± 1.53	3.73 ± 0.37
2013 Feb. 15	3.60 ± 0.36	1.59 ± 0.16	15.12 ± 1.51	5.51 ± 0.55
2013 Mar. 10	3.40 ± 0.34	3.10 ± 0.31	13.74 ± 1.37	3.85 ± 0.39
2013 Mar. 15	3.72 ± 0.37	1.54 ± 0.15	14.53 ± 1.45	5.41 ± 0.54
2013 Mar. 22	5.07 ± 0.51	2.10 ± 0.21	15.12 ± 1.51	4.86 ± 0.49
2013 Mar. 25	4.97 ± 0.50	2.15 ± 0.22	15.29 ± 1.53	4.46 ± 0.45

Table 3.3. Flux of fitted components.

Epoch	C1 (Jy)	C2 (Jy)	C3 (Jy)	C4 (Jy)
2013 Apr. 1	4.02 ± 0.40	2.09 ± 0.21	15.78 ± 1.58	3.81 ± 0.38
2013 Apr. 17	5.68 ± 0.57	2.69 ± 0.27	15.69 ± 1.57	4.09 ± 0.41
2013 Apr. 29	5.10 ± 0.51	2.32 ± 0.23	15.02 ± 1.50	4.20 ± 0.42
2013 Apr. 30	4.29 ± 0.43	2.70 ± 0.27	15.12 ± 1.51	3.27 ± 0.33
2013 May. 26	5.04 ± 0.50	2.01 ± 0.21	15.22 ± 1.52	3.90 ± 0.39
2013 Aug. 17	5.26 ± 0.53	2.38 ± 0.24	15.58 ± 1.56	3.66 ± 0.37
2013 Aug. 22	5.15 ± 0.52	2.71 ± 0.27	15.92 ± 1.59	3.95 ± 0.40
2013 Sep. 10	3.91 ± 0.39	1.56 ± 0.16	15.39 ± 1.54	4.86 ± 0.49
2013 Sep. 16	5.39 ± 0.54	2.17 ± 0.22	15.12 ± 1.51	4.95 ± 0.50
2013 Oct. 10	5.74 ± 0.57	2.41 ± 0.24	15.94 ± 1.59	4.09 ± 0.41
2013 Oct. 12	5.76 ± 0.58	1.90 ± 0.19	16.08 ± 1.61	5.48 ± 0.55
2013 Nov. 2	6.40 ± 0.64	2.63 ± 0.26	17.25 ± 1.73	4.75 ± 0.48
2013 Nov. 8	5.64 ± 0.56	1.95 ± 0.20	17.09 ± 1.71	4.44 ± 0.44
2013 Dec. 20	5.54 ± 0.55	2.58 ± 0.26	17.99 ± 1.80	3.99 ± 0.40

Notes.

Flux and its error for each fitted component. Error is estimated as the root sum squares of calibration error (10% of component) and image noise rms of each epoch.

3.2 Change in Relative Positions of Components

We need to define the reference position for the following discussion of kinematics, since the information of absolute position in each image is lost at the fringe-fitting and self-calibration processes. In the same way as Suzuki et al. (2012), we set the optically thick radio core C1 as the reference position, and evaluate kinematics of other components relative to it.

Figure 3.2 shows the evolution of the peak positions of C2 (green triangles), C3 (blue circles), and C4 (red squares) with respect to C1 (magenta circle) that were obtained in the total intensity images at 80 epochs over six years. C2 exists before the advent of C3 (Nagai et al., 2010; Suzuki et al., 2012), and the motion of C2 is not systematic and almost stable. On the other hand, C3 and C4 travel mainly southward with the motion in the east-west direction. This trend of the motion of C3 is the same as reported in Suzuki et al. (2012) for the period between 2003 November and 2008 November. Thus, we divide relative angular separation from C1 as a function of time into two directions projected on right ascension and declination in Figure 3.3, since the motions mentioned above of C2, C3 and C4 with respect to C1 cannot be expressed as simple straight ones.

In order to describe the average positional change of C3, we define the average proper motion as a vector $(\langle\mu\rangle, \langle\Phi\rangle)$, where $\langle\mu\rangle$ represents the mean angular speed of motion and $\langle\Phi\rangle$ expresses the average direction of motion relative to C1. The average values are calculated as follows: $\langle\mu\rangle = (\langle\mu_x\rangle^2 + \langle\mu_y\rangle^2)^{1/2}$ and $\langle\Phi\rangle = \arctan(\langle\mu_x\rangle / \langle\mu_y\rangle)$,

where $\langle\mu_x\rangle$ and $\langle\mu_y\rangle$ are the average angular speed projected on x (right ascension) and y (declination) axes, respectively. Then, we fit the (x, y) position versus time for C3 with the straight lines that minimize the χ^2 statistic as presented in Figure 3.4(a) and 3.4(c). The best-fit values are $\langle\mu_x\rangle = -0.005 \pm 0.009 \text{ mas yr}^{-1}$, $\langle\mu_y\rangle = -0.23 \pm 0.02 \text{ mas yr}^{-1}$. Therefore, the average proper motion vector is derived as $(\langle\mu\rangle, \langle\Phi\rangle) = (0.23 \pm 0.02 \text{ mas yr}^{-1}, 181.2 \pm 2.3 \text{ deg})$. This average apparent speed corresponds to $\langle\beta_{\text{app}}\rangle = 0.27 \pm 0.02$ in units of the speed of light c . This value is consistent with the result of Suzuki et al. (2012) ($\langle\beta_{\text{app}}\rangle = 0.23 \pm 0.06$ between 2003 November 20 and 2007 November 2, when C3 is not identified in 22 GHz images). Assuming the previously estimated jet viewing angle (11–55 deg; Lister et al., 2009; Tavecchio and Ghisellini, 2014; Abdo et al., 2009a; Walker et al., 1994; Asada et al., 2006), the intrinsic speed of C3 can be estimated to be 0.28–0.59 c , which corresponds to the Lorentz factor of 1.0–1.2 (the Doppler factor ~ 1.1 –1.9).

We also derive the average proper motion vector of C4, and $(\langle\mu\rangle, \langle\Phi\rangle) = (0.27 \pm 0.05 \text{ mas yr}^{-1}, 188.4 \pm 9.5 \text{ deg})$ (see dashed straight line shown in Figure 3.2). This mean angular speed is equivalent to $\langle\beta_{\text{app}}\rangle = 0.31 \pm 0.05$, and the intrinsic speed, the Lorentz factor and the Doppler factor can be estimated 0.31–0.62 c , 1.1–1.3 and 1.2–2.0, respectively, assuming the jet viewing angle of 11–55 deg. These values of C4 are similar to those of C3.

The uncertainties in the best-fit parameters can be estimated from the confidence interval, which is generally derived with grid-search techniques of χ^2 surface. However, a periodical motion model examined in § 3.3 have nine parameters, of which grid-search is computationally expensive and challenging. Instead, in this thesis, we derived estimates of uncertainties in the best-fit parameters of proper motion models with a Monte Carlo simulation as follows. We created 10^5 trial data sets generated from the best-fit model with Gaussian random noises of which standard variations are same to positional errors derived in § 2.4. Samples of the best-fit parameters for all trial data sets were derived with the least-square method and used to estimate confidence limits. We took the edges of the middle 99.7% (3σ) fractions of samples, and adopted them as estimates of 3σ -confidence interval. We note that derived uncertainties are larger than the standard errors of the least square fitting, indicating that derived uncertainties are more robust than the standard errors.

3.3 Periodicity Analysis on Wobbling Motion of C3

After subtracting the linear trends from the C3 positional change in Figure 3.4(a) and 3.4(c), the residual positional change diagram indicates oscillatory behavior as shown in Figure 3.4(b) and 3.4(d). This indication is verified as follows.

We performed two types of analyses in order to check whether the relative motion of C3 with respect to C1 has a periodicity. First, we examined significance of periodicity by fitting the (x, y) positional change of C3 using separately two types of function that

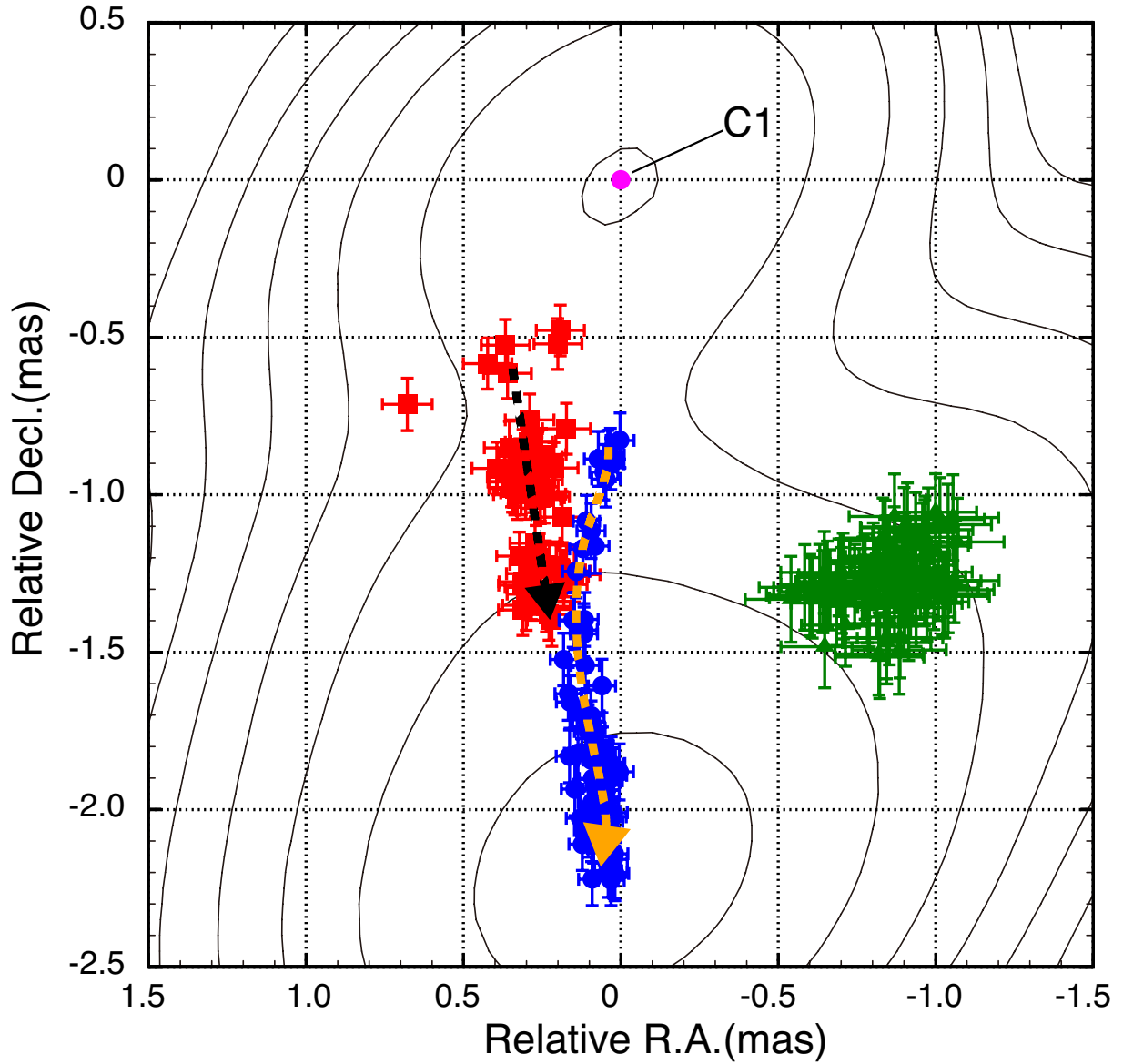


Figure 3.2. Sky position plots of C2 (green triangles), C3 (blue circles), and C4 (red squares) for all 80 epochs, superposed on the contours of 22 GHz intensity distribution on 2013 December 20 (MJD 56646). C1 (magenta circle) is set as the reference position at the origin. Positional error is estimated in § 2.4. Dashed curved and straight lines indicate wobbling motion of C3 and linear motion of C4, respectively.

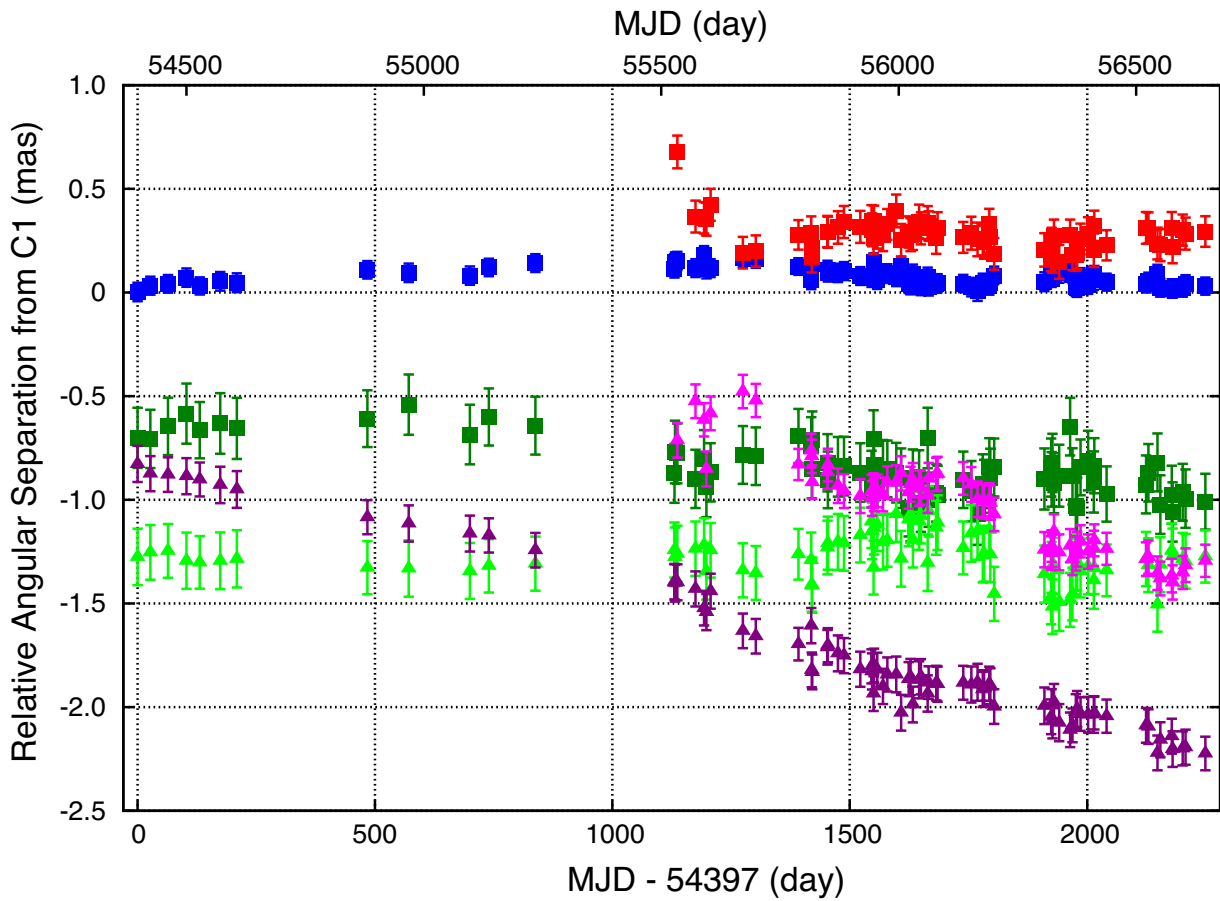


Figure 3.3. Relative angular separation from C1 projected on right ascension (square symbols) and declination (triangle symbols) as a function of time in days over about six years. Green squares and lime triangles represents relative separation between C1 and C2 projected on right ascension and declination, respectively. Blue squares and purple triangles represents relative separation between C1 and C3 projected on right ascension and declination, respectively. Red squares and magenta triangles represents relative separation between C1 and C4 projected on right ascension and declination, respectively. Positional error is estimated in § 2.4.

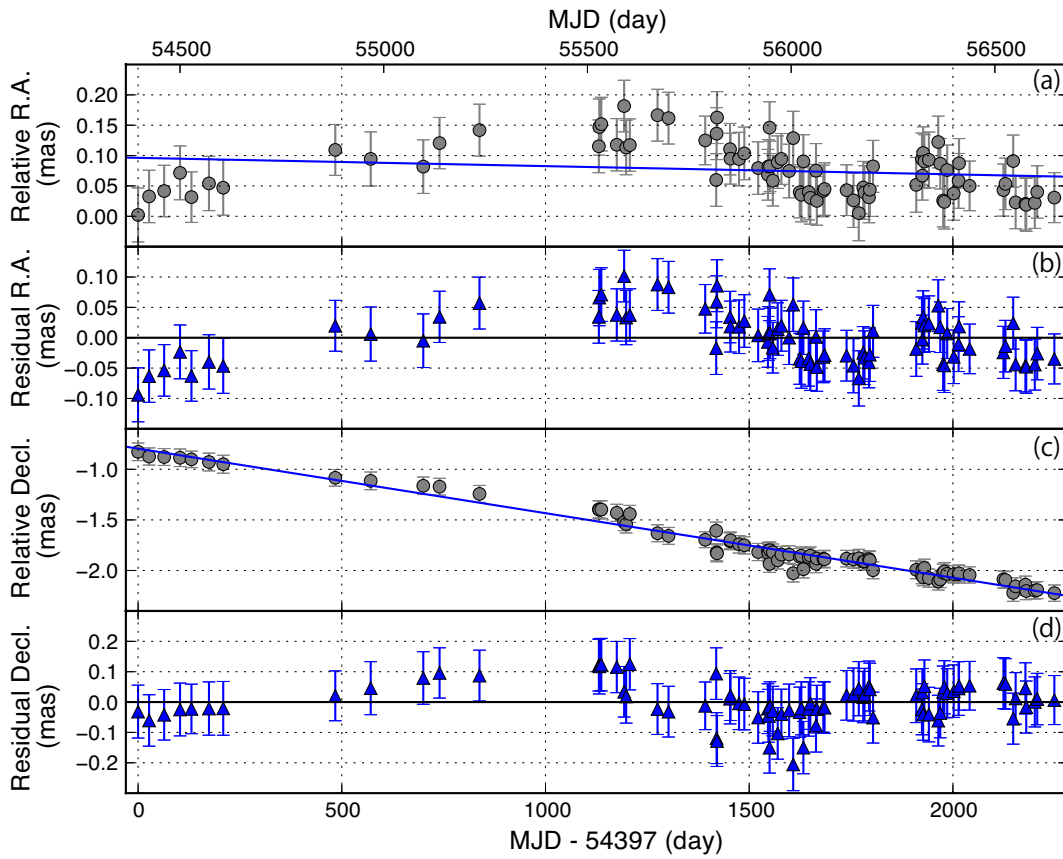


Figure 3.4. (a) Relative angular separation projected on right ascension and (c) declination between C1 and C3 as a function of time in days over about six years. Blue lines are fitted linear functions. Blue triangles in (b) and (d) are the residuals after subtracting the linear trends in (a) and (c), respectively. Positional error is estimated in § 2.4.

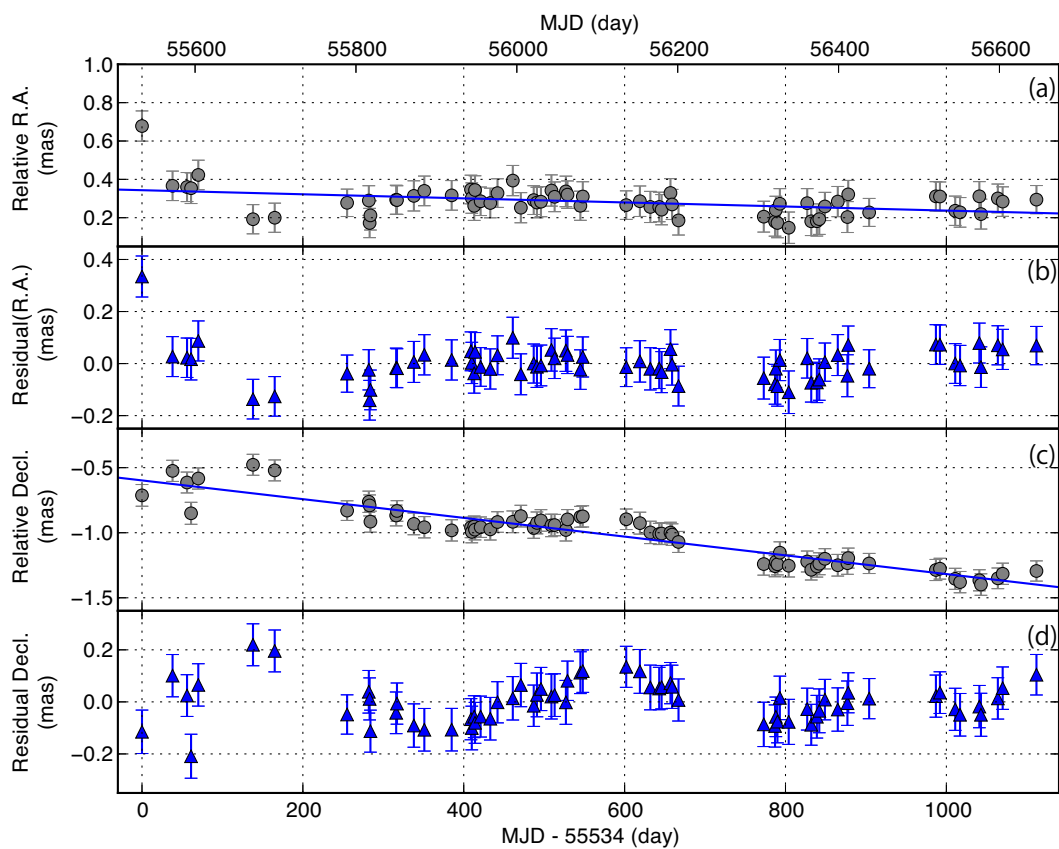


Figure 3.5. Same as Figure 3.4, but for C4.

Table 3.4. The best-fit parameters of the linear motion model.

Parameter	Best-fit value
$a(\text{mas day}^{-1})$	$(-1.4 \pm 2.6) \times 10^{-5}$
$b(\text{mas})$	0.10 ± 0.04
$c(\text{mas day}^{-1})$	$(-6.4 \pm 0.5) \times 10^{-4}$
$d(\text{mas})$	-0.80 ± 0.08

Errors are 3σ -confidence intervals estimated by the Monte Carlo method with 10^5 trials.

minimize the χ^2 statistic (Figure 3.4 and 3.6) and employing some information criteria. One is described by a linear motion model as

$$x(t) = at + b, \quad (3.1)$$

$$y(t) = ct + d, \quad (3.2)$$

and the other is expressed by a periodic motion model as

$$x(t) = A \sin\left(\frac{2\pi}{P_{\text{obs}}^{\text{fit}}}t + \frac{\pi}{180}B\right) + Ct + D, \quad (3.3)$$

$$y(t) = E \sin\left(\frac{2\pi}{P_{\text{obs}}^{\text{fit}}}t + \frac{\pi}{180}F\right) + Gt + H, \quad (3.4)$$

where the units of $x(t)$ and $y(t)$ are in mas and t is the time from 2007 October 24 (MJD 54397) in days, and $P_{\text{fit}}^{\text{obs}}$ is the common parameter which denotes the period of the periodic function.

The best-fit parameters are listed in Table 3.4 and 3.5. The errors of these parameters were 3σ -confidence intervals estimated by the Monte Carlo method with 10^5 trials, considering correlation between parameters. Assuming that underlying errors of data points are normally distributed and independent, the reduced χ^2 of the best fit based on the linear motion model and the periodic motion model are 0.76 and 0.45, respectively. Hence, we selected the more probable one of these two best-fit models using F -test and the Akaike information criterion (AIC) (Akaike, 1974), the latter is an indicator of the relative quality of a statistical model for a given dataset. The preferred model verified by these two methods is the periodic motion model. Comparing the AIC values of these two models, we derived the relative probability of the linear motion model to the periodic motion model. As a result, the linear motion model is 4.2×10^{-9} times as probable as the periodic motion model, which strongly suggests that the motion is periodic.

Next, we searched for evidence of periodicity using the Lomb-Scargle periodogram (hereafter LS periodograms), which gives a least-square estimate of the periodogram based on unequally sampled time series data (Lomb, 1976; Scargle, 1982). We derived

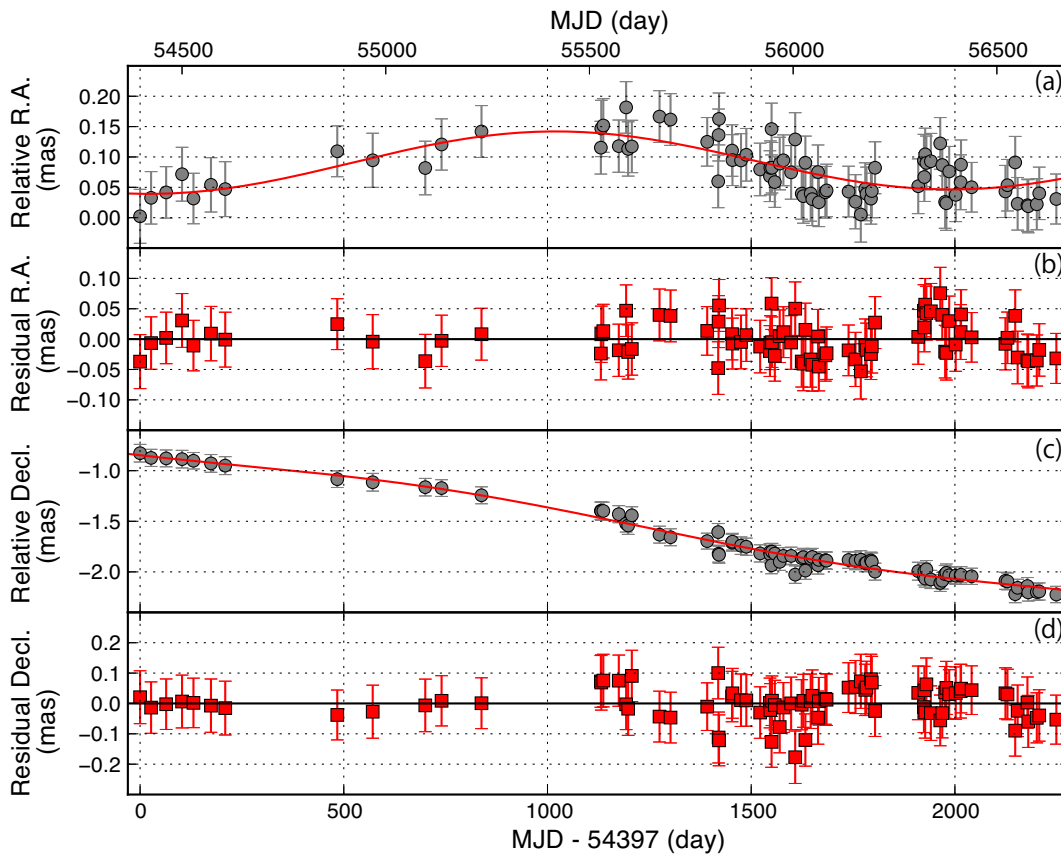


Figure 3.6. (a) Relative angular separation projected on right ascension and (c) declination between C1 and C3 as a function of time in days over about six years. Red lines are fitted periodic functions with the common period between (a) and (c). Red squares in (b) and (d) are the residuals after subtracting the periodic trends in (a) and (c), respectively. Positional error is estimated in § 2.4.

Table 3.5. The best-fit parameters of the periodic motion model.

Parameter	Best-fit value
$A(\text{mas})$	$0.050^{+0.20}_{-0.023}$
$P_{\text{obs}}^{\text{fit}}(\text{days})$	$(2.0^{+3.1}_{-0.4}) \times 10^3$
$B(\text{deg})$	-95^{+160}_{-85}
$C(\text{mas day}^{-1})$	$(3.8^{+210}_{-28}) \times 10^{-6}$
$D(\text{mas})$	$0.09^{+0.04}_{-0.31}$
$E(\text{mas})$	$0.07^{+0.51}_{-0.05}$
$F(\text{deg})$	-45^{+140}_{-90}
$G(\text{mas day}^{-1})$	$(-6.1^{+5.5}_{-0.7}) \times 10^{-4}$
$H(\text{mas})$	$-0.80^{+0.10}_{-0.66}$

Errors are 3σ -confidence intervals estimated by the Monte Carlo method with 10^5 trials.

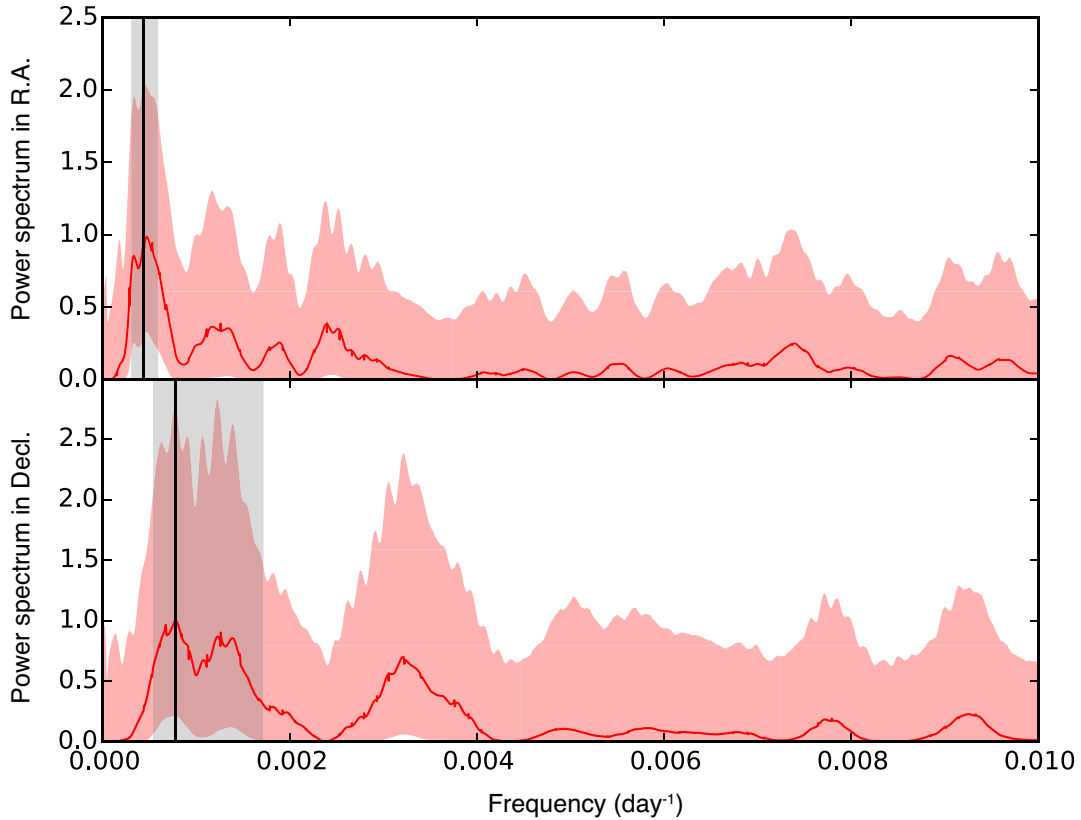


Figure 3.7. The Lomb-Scargle periodograms for residuals of linear-fittings in right ascension (top panel) and declination (bottom panel) directions. Red solid lines indicate the least-square estimate of the power spectrum normalized by the maximum value, while their 3σ uncertainties are shown in surrounding red-shaded regions, which are derived with the non-parametric percentile bootstrap method. Black vertical lines indicate the peaks of the 3σ -credible areas with the largest power and SNR, while gray-shaded regions exhibit their 3σ uncertainties.

the LS periodograms for residuals of linear fittings in both right ascension and declination directions. Uncertainties in the LS periodograms were estimated with the non-parametric percentile bootstrap method (e.g., Akiyama et al. (2013)), which is a straightforward and efficient method in deriving estimates of confidence intervals particularly for large number of parameters. We created 10^5 data sets (so-called bootstrap samples) by re-sampling, in which repetition of data was allowed. Each data-set has the number of data same to original ones. Periodograms for all of 10^5 bootstrap samples were calculated and then used to estimate confidence intervals. The Percentile bootstrap confidence limits of the power spectrum at each frequency were obtained as the edges of the middle 99.7% (3σ) fractions of the bootstrap estimates.

The derived LS periodograms for residuals of linear fittings are shown with their 3σ uncertainties in Figure 3.7. A few regions are marginally detected with $> 3\sigma$ in both right ascension and declination directions, although most of power spectrums are dominated by 3σ errors. In right ascension direction, the peak with the largest power and signal-

Table 3.6. Results of periodicity analyses.

Method	Period (yr)*		Amplitude ($\times 10^{-2}$ pc) [†]	
	R.A.	Decl.	R.A.	Decl.
Best fit	$5.3^{+8.3}_{-1.2}$		$1.8^{+6.9}_{-0.8}$	$2.5^{+17.9}_{-1.9}$
Lomb-Scargle	$6.2^{+1.7}_{-2.8}$	$3.4^{+1.6}_{-1.9}$

Error estimation is described in the text in detail.

* Period of the periodic motion measured in the source frame, $P_{\text{source}} = \frac{P_{\text{obs}}}{1+z}$, where z is the source redshift, and P_{obs} is the period measured in the observer's frame. The period derived by the best fit method (least square method) is the common parameter between right ascension and declination directions.

† Amplitude of the periodic motion along each axis. The method using Lomb-Scargle periodograms does not tell the information about amplitude.

to-noise ratio (SNR) was located in a 3σ -credible region at a frequency of $\sim 4.4 \times 10^{-4}$ day⁻¹ with significance of 4.3σ . The 3σ estimate of the peak frequency for this region is $4.4^{+1.5}_{-1.4} \times 10^{-4}$ day⁻¹ corresponding to a period of $6.3^{+1.7}_{-2.8}$ yr. On the other hand, in declination direction, the LS periodogram has the peak with the largest power and SNR in a 3σ -credible region at a frequency of $\sim 7.8 \times 10^{-4}$ day⁻¹ with significance of 3.8σ . The 3σ estimate of the peak frequency for this region is $7.8^{+94}_{-2.4} \times 10^{-4}$ day⁻¹ corresponding to a period of $3.5^{+1.6}_{-1.9}$ yr. The peak frequencies of periodograms are consistent between right ascension and declination directions, and also with the derived period for the periodic motion model.

Physical parameters derived through the above two methods are given in Table 3.6. Period of the periodic motion in the source frame is calculated as $P_{\text{source}} = \frac{P_{\text{obs}}}{1+z}$, where z is the source redshift, and P_{obs} is the period measured in the observer's frame. The time span of our dataset (~ 6.2 yr) is comparable to these derived periods. Therefore, we need additional monitoring of C3 motion to verify the periodic trend more precisely.

4

Discussion

In § 3.2, we derived the relative velocity of C3 with respect to C1 in the period between 2007 October and 2013 December, and found it to be almost constant and sub-relativistic ($\sim 0.3\text{--}0.6c$ assuming the jet viewing angle of $11\text{--}55$ deg) in the central subparsec-scale region. It is interesting to consider why the relative speed of C3 is significantly slow, whereas the speed of the underlying flow is generally relativistic. We discuss the intriguing kinematic property of C3 and in § 4.1. We also found that the relative motion of C3 relative to C1 had a periodicity (~ 5 yr) by means of two different periodicity analyses in § 3.3. We speculate about possible origins of the periodic motion of C3 with respect to C1 in § 4.2.

4.1 Why is the Velocity of C3 Remarkably Slow in the Relativistic Jet?

In this section, we consider why the relative velocity of C3 with respect to C1 is sub-relativistic in the relativistic jet flow. As described in § 1.1.2, bright regions in the jet stream called jet knots are formed by internal shock wave in the vicinity of the central engine. The proper motions of the jet knots in blazars often exceed the speed of light (e.g., Homan et al., 2001; Jorstad et al., 2001). These superluminal motions suggest that the intrinsic velocity of jet knots is ultra-relativistic and nearly coincident with the line of sight. However, the relative speed of C3 with respect to C1 ($\sim 0.3\text{--}0.6c$) is much slower than that of jet knots, after considering relatively wide range of intrinsic speed due to the uncertainty about the jet viewing angle ($11\text{--}55$ deg). Instead, the kinematic property of C3 is similar to that of hotspots widely identified in large-scale double radio sources such as powerful FR1 and FR2 radio galaxies ($\sim 0.01\text{--}0.1c$) (e.g., Conway, 2002). In the case of small-scale radio sources, advance speed of hotspots of several CSOs are also sub-relativistic ($\sim 0.1\text{--}0.3c$), indicating a dynamical age of $\sim 10^2\text{--}10^4$ yr taking into account their size of ≤ 1 kpc (e.g., Polatidis et al., 1999; Conway, 2002; Nagai et al., 2006).

From theoretical point of view, many authors have been investigating the dynamical evolution of hotspots velocity, pressure and mass density in radio-loud AGNs. Scheck

et al. (2002) examined the long-term evolution of the powerful AGN jets propagating into a homogeneous ambient medium with two-dimensional relativistic hydrodynamic simulations. Scheck et al. (2002) found that their evolution proceeds in two different phases: (i) *one-dimensional (1D) dynamical evolution phase* ($t < 1.2 \times 10^5$ yr) and (ii) *two-dimensional (2D) dynamical evolution phase*. During the 1D phase, multidimensional effects on the tips of jets are negligible and the jets propagate ballistically with nearly constant hotspot velocity ($v_{\text{HS}} \propto l_{\text{h}}^{-0.11}$), where l_{h} is the length from the center of the galaxy to the hotspot. The 2D phase starts when the first large vortices are formed near the tips of jets, causing the cross-section area of the cocoon head to increase. Then, the hotspots start to decelerate, but the speed of unshocked jets remains the same relativistic one during whole simulations. Kawakatu and Kino (2006) aimed to construct an appropriate dynamical model of hotspots in radio-loud AGNs, taking proper account of (I) the conservations of the mass, momentum and kinetic energy flux of the unshocked jets, (II) the deceleration process of the jet head by shocks and (III) the cocoon expansion without assuming the constant aspect ratio of the cocoon. This model can explain the observational trends of the hotspot velocity ($v_{\text{HS}} = \text{constant}$), pressure, size and mass density in both CSOs and FR2 radio galaxies.

Considering that the resultant velocity of C3 in 3C 84 is sub-relativistic ($\sim 0.3\text{--}0.6c$) and almost constant in subparsec-scale jet in the initial phase ($\lesssim 10$ yr), C3 appears to show similar behavior to the terminal hotspot in mini-radio lobe. More strictly speaking, the new radio component C3 is the head of radio lobe including hotspots at a very early stage of radio lobe evolution, since the higher resolution image using 43 GHz VLBA recently revealed that the region around C3 showed very complex structure (Nagai et al., 2014). Similarity between the velocity of C4 ($\sim 0.3\text{--}0.6c$) and that of C3 might mean that C4 is also the head of a mini-radio lobe including hotspots. Although hotspots themselves cannot be resolved by VERA, our result implies that the radio lobes in radio galaxies might be already formed in subparsec-scale jets close to the central SMBHs.

It is also worthwhile to emphasize that the measured advance speed of C3 assuming the jet viewing angle of $11\text{--}55$ deg is slightly faster than that of other CSOs. This trend is also identified on ~ 15 mas (~ 5 pc) scale radio jet/lobe associated with the 1959 outburst in 3C 84 (Asada et al., 2006; Nagai et al., 2008). The apparent speed of the hotspot on ~ 5 -pc scale was $0.34 \pm 0.09c$ in 2001. Nagai et al. (2008) noticed that the hotspot on ~ 5 -pc scale (component ‘B3’ in Asada et al. (2006)) was probably produced by the interaction between the unshocked jet material ejected before 1959 and new-born unshocked jet in the 1959 outburst, rather than by the interaction between the new-born unshocked jet in the 1959 and ambient external medium. Similarly, the slightly faster speed of C3 on subparsec scale ($\sim 0.3\text{--}0.6c$) might be the result of the interaction between the unshocked jet material ejected before 2005 and newly unshocked jet ejected in the 2005 outburst. Figure 4.1 shows a schematic picture described above in this section.

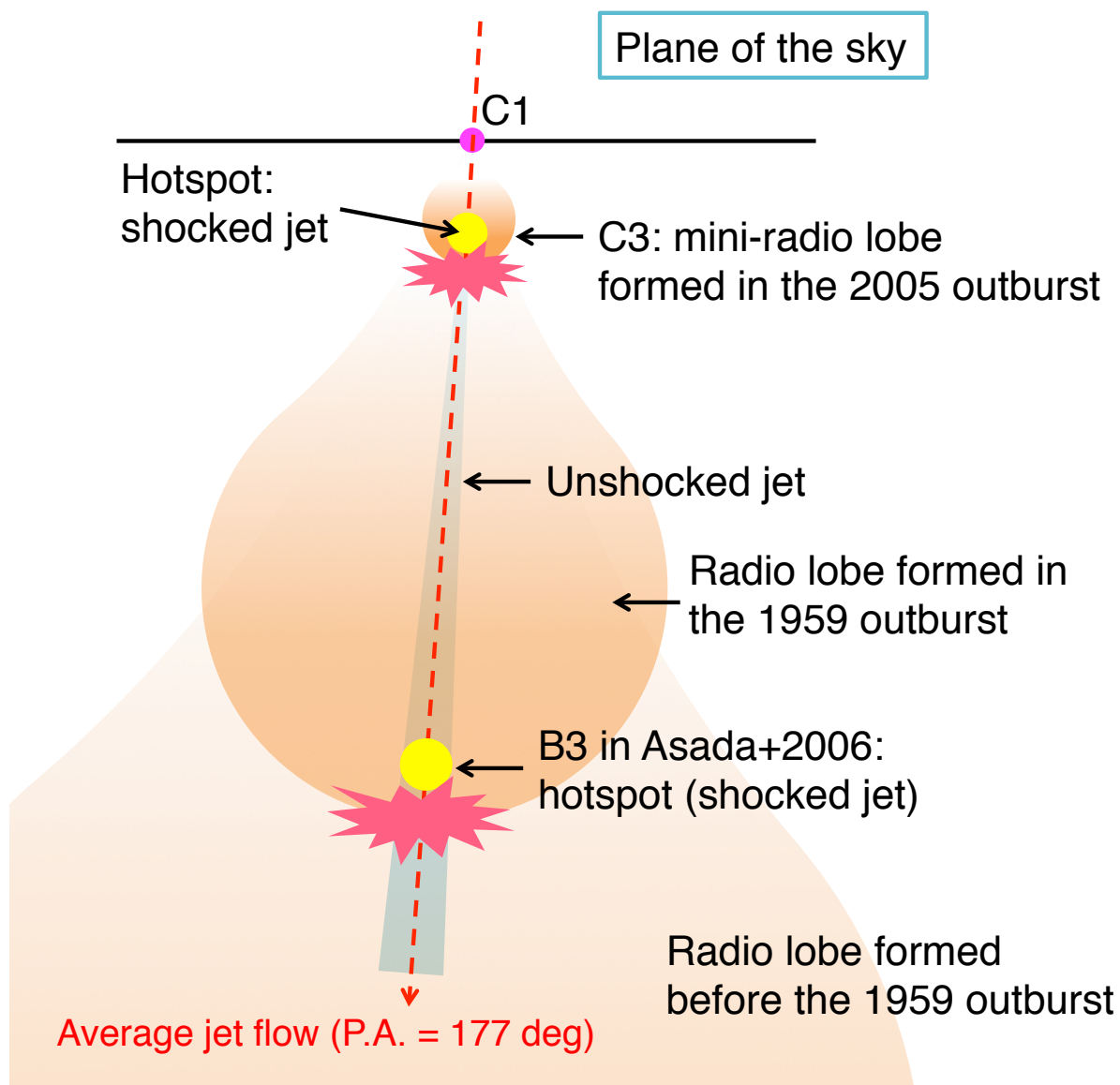


Figure 4.1. Schematic picture of the interactions between the pre-existing unshocked jet material and the newly ejected unshocked jet described in § 4.1. See text in detail.

4.2 Possible Origin of the Periodic Motion of C3

In this section, we consider what mechanisms control the periodic motion of C3 with respect to C1. The periodic motion of C3 can be explained if the underlying continuous jet flow shows precession. Precessions on subparsec-scale jets are generally caused by several physical mechanisms such as jet plasma instabilities (Figure 4.2), gravitational torques in a binary black hole system (Figure 4.3), magnetic torques (Figure 4.5), and accretion disk precession (e.g., Lobanov and Zensus, 2001; Lobanov and Roland, 2005; McKinney et al., 2013; Caproni et al., 2004). We discuss whether each physical mechanism can apply to the periodic motion of C3 or not in the following paragraphs.

First, as for jet plasma instabilities, Lobanov and Zensus (2001) analyzed parsec-scale radio jet in the quasar 3C273 observed with the 5 GHz VSOP (VLBI Space Observatory Programme), and found two threadlike patterns that formed a double helix inside the jet shown in Figure 4.2. They suggested that the double helical structure resulted from a Kelvin-Helmholtz (KH) instability, and that formation of KH instability needed an external periodic process (such as precession of jet axis, rotation of the accretion disk, or motion of the jet nozzle) supplying the initial perturbation of the jet plasma and controlling the basic instability modes. In the case of our results, the path of C3 indeed shows wobbling, but the jet transverse structure cannot be resolved due to the lack of spatial resolution. Thus, we cannot conclude that the periodic motion of C3 is not an indicator of KH instabilities, and we need to observe the transverse structure of the subparsec-scale jet with higher-resolution and high-sensitivity VLBI.

Second, as for precession induced by gravitational torques in a binary black hole (BBH) system, this mechanism acts when two black holes reside in the same system and then these black holes orbit the common center of mass shown in Figure 4.3. As a result, the jet nozzles precess since jets are believed to be launched around the accretion disks hosted by the black holes. Sometimes, this mechanism also induces light variations of the BBH system. The BL Lac objects OJ 287 is famous for showing periodic light variations with 12 yr intervals (see Figure 4.4). Sillanpaa et al. (1988) explained that periodic outbursts seen in a long-term V -band light curve of OJ 287 were related to tidally induced mass flows from accretion disks into the BBH system passing at pericenter, once every 12 yr orbital period. On the other hand, 3C 84 has not shown periodic light variations in radio band since 1970's shown in Figure 1.19. Therefore, we cannot conclude that gravitational torques caused by BBH system cannot explain the periodic motion of C3, since there is no evidence indicating BBH system.

Third, as for precession induced by magnetic torques, this mechanism acts in a twisted strong magnetic fields in the vicinity of the central spinning Kerr black hole. McKinney et al. (2013) showed that the axis of jet ejected at later time, that is, the jet axis near the jet base gradually coincide with the spin axis of black hole because the misaligned angular momentum is radiated away as a part of the electromagnetic outflow. If this is the case, we expect to detect toroidal magnetic field with polarization observations. However, the

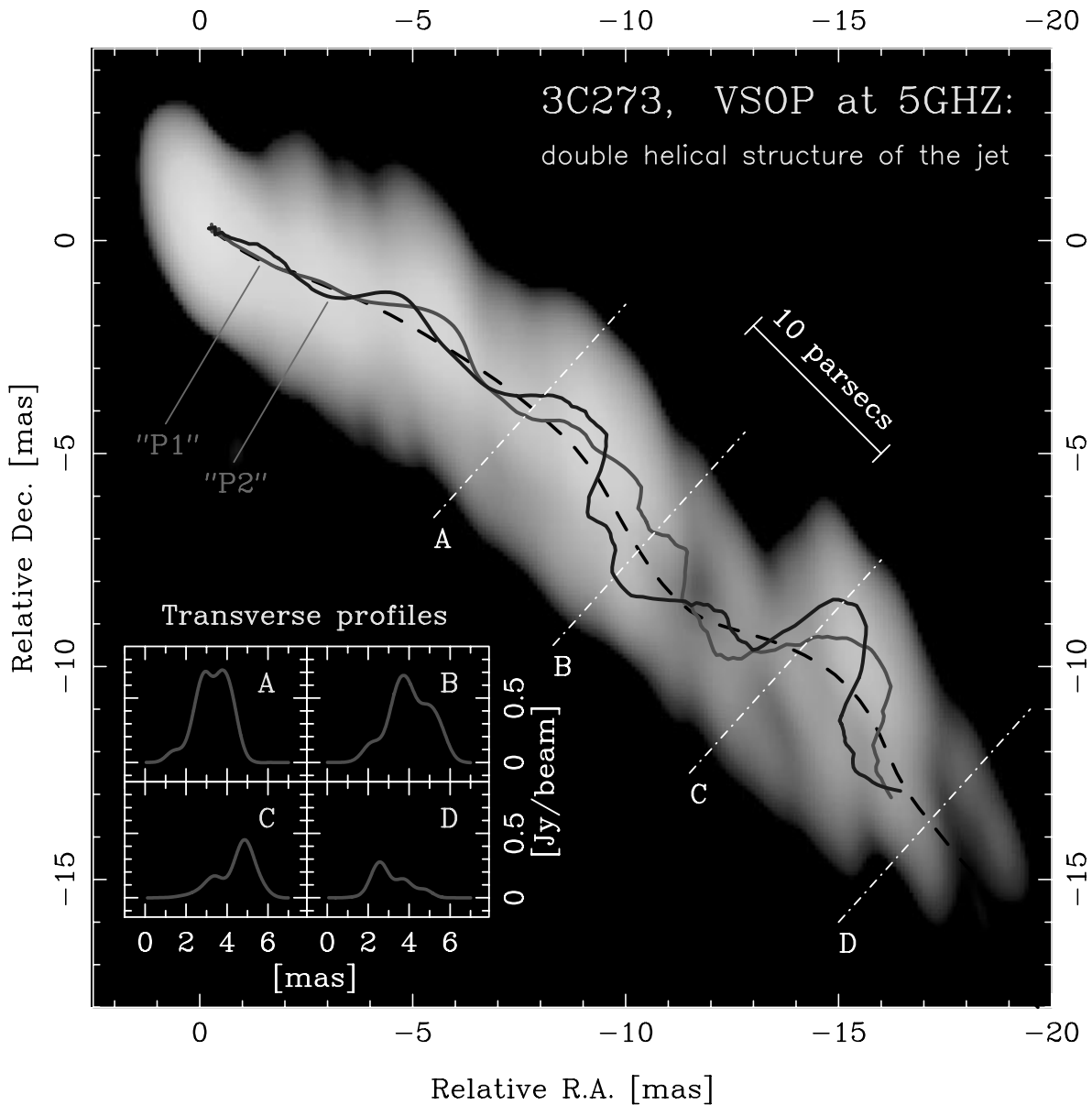


Figure 4.2. Parsec-scale radio jet in the quasar 3C273 imaged with the 5 GHz VSOP (VLBI Space Observatory Programme) from Lobanov and Zensus (2001). The image is restored with an elliptical Gaussian beam, which has major and minor axes of 2.1 mas and 0.5 mas, oriented at a position angle of 12.9 deg. The peak brightness in the image is $4.52 \text{ Jy beam}^{-1}$, and the noise level is $2.1 \text{ mJy beam}^{-1}$. The dot-dashed white lines indicate the locations of the four flux density profiles shown in the inset. Each of these profiles is centered on the smoothed ridge line (the dashed black line) and oriented perpendicular to it. Each of the measured profiles is fitted by two Gaussian components labeled as P1 and P2. The locations of the peaks of P1 and P2 are marked in the image by the light gray and dark gray lines, respectively. The double helical pattern formed by P1 and P2 suggests that they result from a Kelvin-Helmholtz instability developing in the jet.

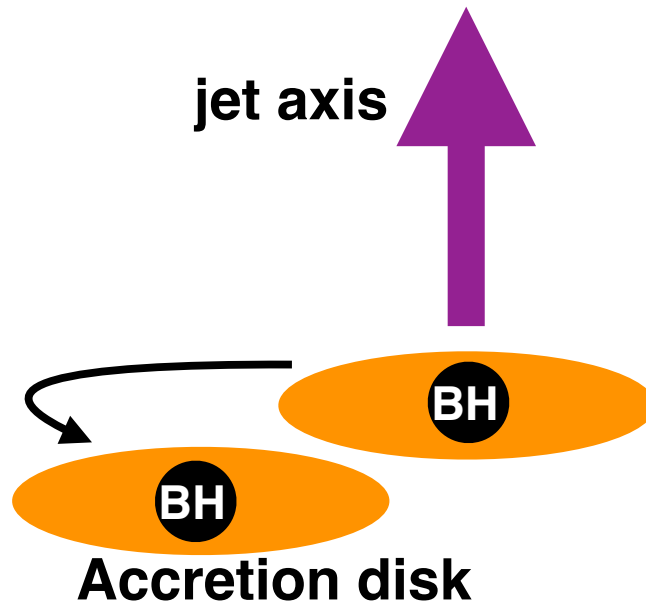


Figure 4.3. Schematic picture of precession induced by gravitational torques in a binary black hole system. This mechanism acts when two black holes reside in the same system and then these black holes orbit the common center of mass. As a result, the jet nozzles precess since jets are believed to be launched around the accretion disks hosted by the black holes.

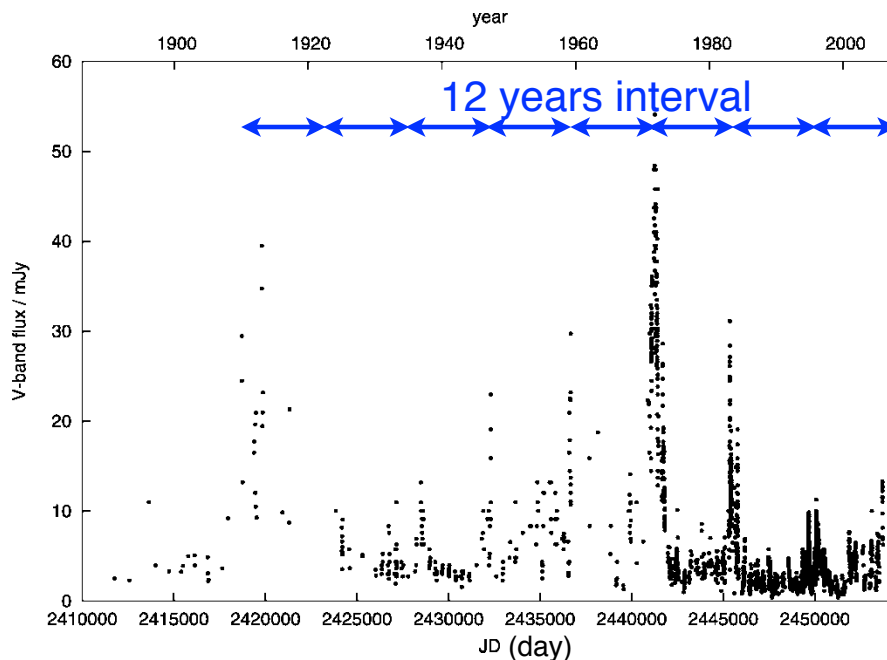


Figure 4.4. An optical V -band light curve of the BL Lac objects OJ 287 between 1891 and 2005 revised from Valtonen et al. (2006). OJ 287 has outbursts at 12 yr intervals, and each outburst consists of two sharp peaks. This periodicity is believed to be due to the binary system where the accretion disk of a primary black hole is tidally perturbed by the secondary black hole passing at pericenter, once every 12 yr orbital period shown in Figure 4.3.

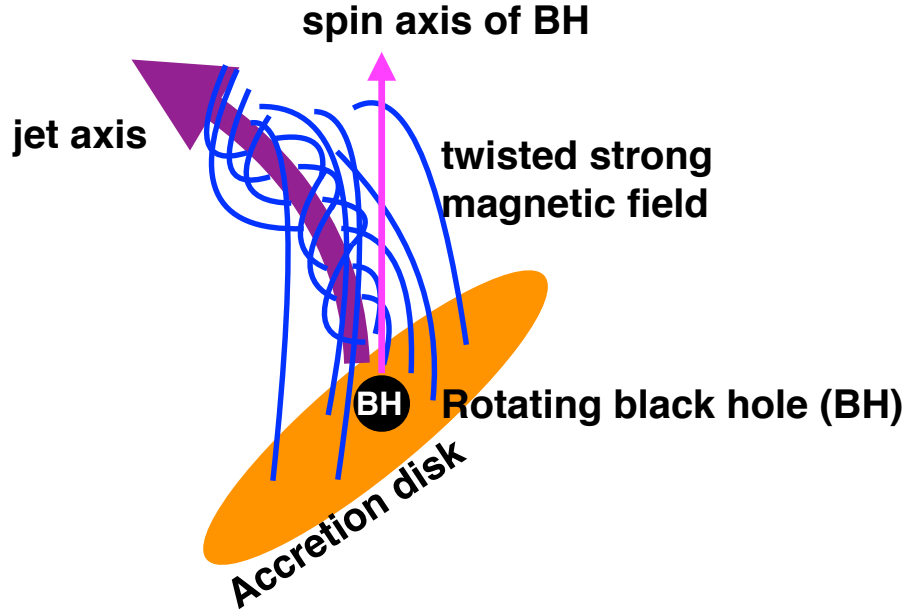


Figure 4.5. Schematic picture of precession induced by magnetic torques. This mechanism acts in a twisted strong magnetic fields in the vicinity of the central engine. The central black hole is spinning. The axis of jet ejected at later time gradually coincide with the spin axis of black hole because the misaligned angular momentum is radiated away as a part of the electromagnetic outflow.

emission from parsec-scale core of 3C 84 is unpolarized, and the degree of polarization of the core is $< 0.1\%$ for 5, 8 and 15 GHz except for 22 GHz (0.2%) (Taylor et al., 2006). This indicates high rotation measure (RM) on parsec scales. Recently, Plambeck et al. (2014) performed polarization observations of 3C 84 at wavelengths of 1.3 and 0.9 mm with the CARMA (Combined Array for Research in Millimeter Wavelength Astronomy) and with the SMA (Submillimeter Array) spanning the period from 2011 to 2013. They showed the RM, determined from the polarimetry, is $(8.7 \pm 2.3) \times 10^5 \text{ rad m}^{-2}$, among the largest ever measured. As described in § 1.1.4, polarization is easier to detect at millimeter wavelengths due to steep decrease of Faraday rotation at shorter wavelengths, and due to smaller millimeter emission region, that is, less problem in RM variations across the source. Thus, we expect to verify the the presence of toroidal magnetic field by measuring RM using millimeter VLBI less suffering from beam depolarization in the future.

Finally, the most probable origin inducing jet precession in 3C 84 is accretion disk precession by the Bardeen-Petterson (BP) effect (Bardeen and Petterson, 1975, see also Figure 4.6) acting on the viscous accretion disk that originates the jet, which is tilted with regard to the equatorial plane of the central spinning Kerr black hole, and inducing the alignment of the disk and the black hole angular momenta. On 10–100 kpc-scales at radio and X-ray band, there are misaligned morphology interpreted as a product by a precessing jet with a period of 3.3×10^7 years and semi-aperture angle of about 50 deg (Dunn et al., 2006, and references therein). Falceta-Gonçalves et al. (2010), using

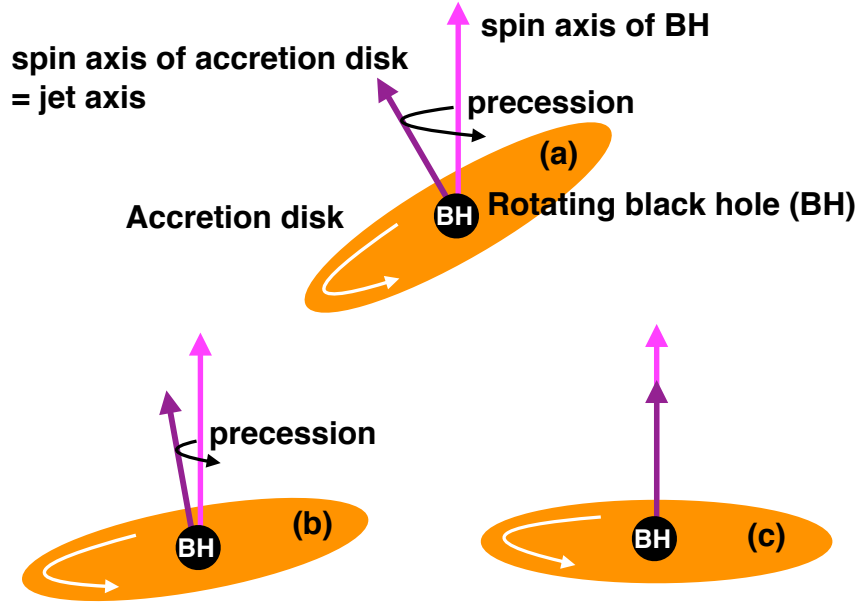


Figure 4.6. Schematic picture of precession and alignment of the disk and the black hole angular momenta induced by Bardeen Petterson effect. This mechanism acts due to the frame-dragging effect of a spinning black hole and the viscosity in an accretion disk. The precessional period and precession angle becomes shorter with time from (a) to (c) denoted in accretion disks.

three-dimensional numerical simulations considering the jet precession evolution by the BP effect, indeed showed that the observed morphology of 3C 84 on 10–100 kpc-scales can be well explained as the production by a precessing jet with a period of 5×10^7 years. They constrained the present precession angle to 30–40 deg, as well as the approximate age of the inflated cavities to 100–150 Myr.

Considering that 100–150 Myr has passed since observed structures on 10–100 kpc formed, the present precession cycle can be expected to be much shorter than 5×10^7 years. Then, it is intriguing to discuss when the misalignment angle is negligible and how much angle we detect five years later from the latest observation epoch by using the period and angle obtained in our study.

First, we calculate the time when the misalignment angle is negligible. We adopt the following model based on the BP effect to investigate them. Under the approximation of a flat accretion disk, that is, an accretion disk with constant surface density, the solution of equation (3) in Scheuer and Feiler (1996) gives an exponential time variation for the misalignment angle $\delta(t)$ between black hole spin and the jet direction, as well as for the precession cycle P_{prec} :

$$\delta(t) = \delta_0 e^{-(t-t_0)/T_{\text{align}}}, \quad (4.1)$$

$$P_{\text{prec}}(t) = P_0 e^{-(t-t_0)/T_{\text{align}}}, \quad (4.2)$$

where δ_0 and P_0 are, respectively, the misalignment angle and precession cycle at time t_0

when disk was formed, and T_{align} is the timescale for alignment between black hole spin and the jet direction. Scheuer and Feiler (1996) showed that $P_0 = T_{\text{align}}$, which we also take into account the equation in our approach. Then, by substituting this equation into Eq. (4.1), we obtain the following,

$$\delta(t) = \delta_0 e^{-(t-t_0)/P_0}. \quad (4.3)$$

Then,

$$\ln \frac{\delta(t)}{\delta_0} = -\frac{t-t_0}{P_0}. \quad (4.4)$$

It can be expressed as

$$\left(\frac{t}{\text{yr}}\right) = \left(\frac{t_0}{\text{yr}}\right) + \left(\frac{P_0}{\text{yr}}\right) \ln \left(\frac{\delta_0/\text{deg}}{\delta(t)/\text{deg}}\right). \quad (4.5)$$

Here, we quote the results from Falceta-Gonçalves et al. (2010) as $t_0 = -1.75 \times 10^8$ yr, $P_0 = 5 \times 10^7$ yr and $\delta_0 = 58$ deg. By substituting these value into Eq. (4.5) and assuming that the misalignment angle is negligible ($\delta(t) = 0.1$ deg), we obtain $t \sim 143$ Myr. Next, we calculate $\delta(t)$ in the latest observation epoch (2013 December 20) in order to obtain the time t corresponding to 2013 December 20. From the equation in Dunn et al. (2006) and Barker and Byrd (1981),

$$\tan \psi = \frac{\sin \delta \sin \phi}{\sin \gamma \cos \delta - \cos \gamma \sin \delta \cos \phi}, \quad (4.6)$$

where γ is viewing angle of precession axis and we assume 18 deg from recently reported in Tavecchio and Ghisellini (2014), and ϕ is phase angle of a counterclockwise (ccw) rotating jet seen from C1 ~ 110 deg on 2013 December 20, and ψ is angle between projected direction of the jet on the plane of the sky and the projected direction of the precession axis of 1 deg. Figure 4.7 shows geometry assumed here. Eq. (4.6) can be expressed as

$$\delta = \arctan \left(\frac{\tan \psi \sin \gamma}{\sin \phi + \tan \psi \cos \gamma \cos \phi} \right). \quad (4.7)$$

By substituting $\gamma = 18$ deg, $\phi = 110$ deg and $\psi = 1$ deg into Eq. (4.7), we obtain $\delta(t) \sim 0.3$ deg. Furthermore, by substituting $\delta(t) \sim 0.3$ deg, $t_0 = -1.75 \times 10^8$ yr, $P_0 = 5 \times 10^7$ yr and $\delta_0 = 58$ deg into Eq. (4.5), we obtain $t \sim 83$ Myr. Thus, we can neglect the precession inducing by BP effect, $(143 - 83) = 60$ Myr later from 2013 December 20, which corresponds to 61 Myr in the observer's frame.

Hence, if this is the case, we expect that the misalignment angle five years later from 2013 December 20 will show negligible change, because five years are much smaller than 61 Myr derived above. In order to obtain the robust result, we continue to monitor the subparsec-scale jet of 3C 84 with high resolution phase-referencing VLBI, since we can get the information on absolute positions of each component with phase-referencing VLBI.

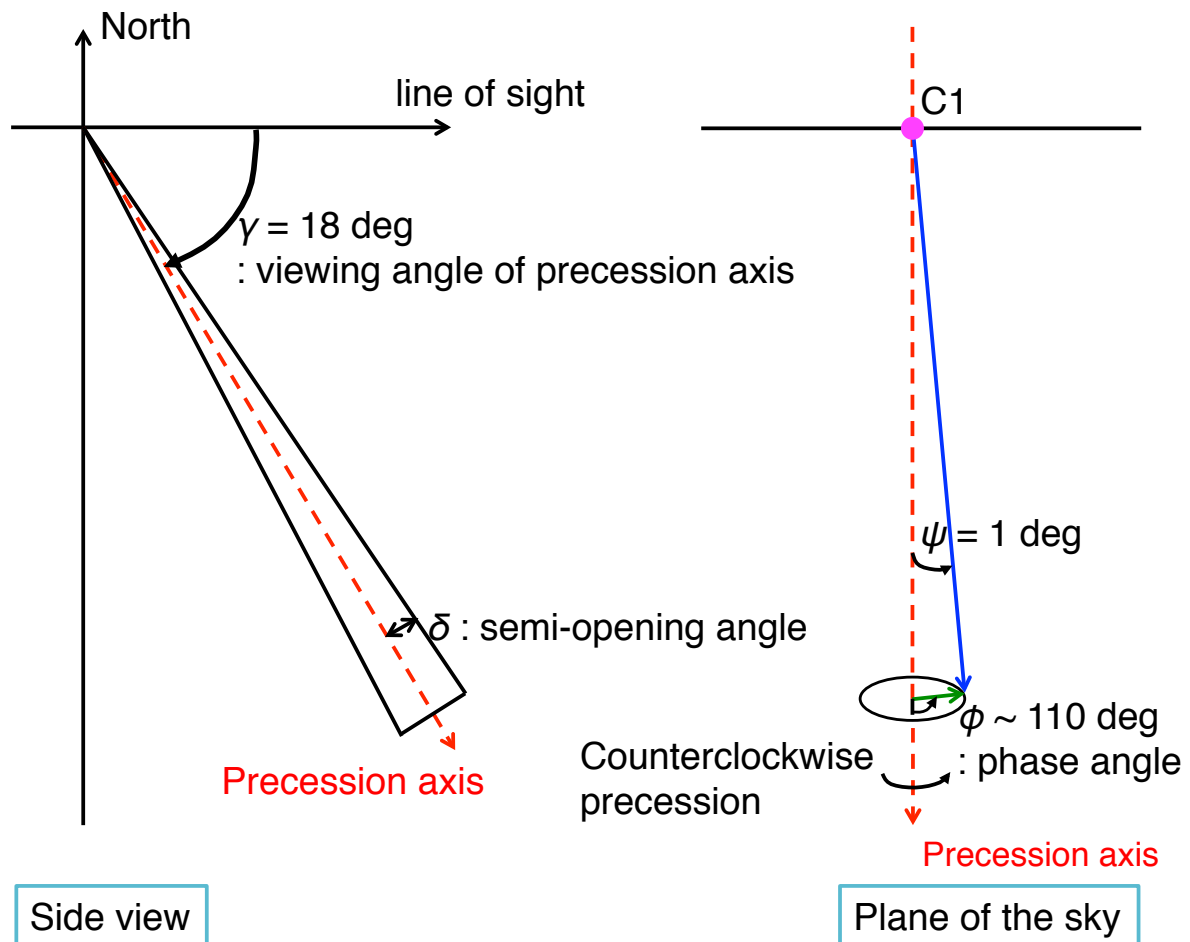


Figure 4.7. Geometry of precession induced by Bardeen Petterson effect. Left and right panels show the side view of a precessing jet and the precessing jet projected on plane of the sky, respectively. γ is viewing angle of precession axis and we assume 18 deg from recently reported in Tavecchio and Ghisellini (2014). ϕ is phase angle of a counterclockwise (ccw) rotating jet seen from C1 ~ 110 deg on 2013 December 20. ψ is angle between projected direction of the jet on the plane of the sky and the projected direction of the precession axis of 1 deg.

Conclusion

I tried to unveil the properties of subparsec-scale radio jet of the radio galaxy 3C 84/NGC 1275 by monitoring time variability of radio jet with the VLBI Exploration of Radio Astrometry (VERA) array. Radio galaxy 3C 84 shows intermittent jet activity, and the radio brightness has increased since 2005. Thus, 3C 84 is one of the best source to study formation and evolution of radio structure in the vicinity of SMBHs. Nagai et al. (2010) found that this activity was ascribed to the central subparsec-scale core, accompanying the ejection of a new bright component (C3) with VERA. Suzuki et al. (2012) found that C3 had emerged from a radio core before 2005, and traveled southward following a parabolic trajectory on the celestial sphere with VLBA at 43 GHz from 2003 November to 2008 November. In this study, we further explored the kinematics of C3 from 2007 October to 2013 December (80 epochs) using 22 GHz VERA data. Summary and discussions are as follows.

- I found that the apparent speed of C3 relative to the radio core is almost constant and sub-relativistic ($0.27 \pm 0.02c$) from 2007 October to 2013 December. This property suggests that C3 may be the head of mini-radio lobe including hotspots, rather than a relativistic knotty component formed as internal shock in underlying continuous jet flow. This result implies that the radio lobe in radio-loud AGNs might be already formed in subparsec-scale jets in the vicinity of SMBHs.
- I also noticed that C3 might follow a helical path with a period of about five years thanks to highly-frequent observations. Although I cannot reliably identify the origin causing the wobbling motion because of the insufficient time span of our dataset and the lack of the information of absolute reference position, the motion might reflect a precessing jet nozzle, induced by the Bardeen-Petterson effect. Based on the precession model induced by the effect, I estimated the precessional angle and period five years later from the latest observation epoch (2013 December 20), and I found that they will show little change even with the use of VLBI. In order to obtain the robust result, we continue to monitor the subparsec-scale jet of 3C 84 with high resolution phase-referencing VLBI.

As mentioned above, I found that hotspots in radio lobes in radio galaxies might be already formed in subparsec-scale jets close to the central SMBHs. I also found that hotspots in radio lobe may be precessed by a spinning SMBH. These results are achieved by unprecedented highly-frequent observations. It is important that the fact that hotspots might be formed in subparsec-scale jets near the central SMBH can constrains the physical state such as velocity, density and pressure in the vicinity of jet base when understanding the formation and evolution of hotspots. Those findings will contribute to constructing more sophisticated theoretical models in the future.

Acknowledgements

First of all, I express my deepest gratitude to Dr. Kazuo Sorai in Hokkaido University for suggestions, discussions and encouragement. I have learned a lot of things related with astronomy, and more general issues of research activities. In particular, we have spent much time on working on daily operation, maintenance and development of the Tomakomai 11-m telescope. I deeply regret that the operation of the telescope will close at the end of this fiscal year, but I really enjoyed working on the telescope and deeply thank him to give me such a wonderful experience.

I would like to appreciate the referees of this thesis, Professor Asao Habe, Professor Takashi Kozasa, Professor Naoki Watanabe and Dr. Yasuhiro Murata.

I express my sincere gratitude to Dr. Hiroshi Nagai and Dr. Motoki Kino. They invited me to GENJI program members, and gave me a lot of suggestions. I also express my deep gratitude to Dr. Kazunori Akiyama for a lot of supports on statistical analyses. I am grateful to all staff of the VERA stations for their assistance in observations.

I also thanks Mr. Yusuke Fujimoto and all members of the Astrophysical laboratory, Hokkaido University for encouragement to carry out this work.

Finally, I would like to thank my family for continuously supporting me through my Ph.D. program.

Bibliography

- A. A. Abdo et al. Fermi Discovery of Gamma-ray Emission from NGC 1275. *ApJ*, 699:31–39, July 2009a. doi: 10.1088/0004-637X/699/1/31.
- A. A. Abdo et al. Radio-Loud Narrow-Line Seyfert 1 as a New Class of Gamma-Ray Active Galactic Nuclei. *ApJ*, 707:L142–L147, Dec. 2009b. doi: 10.1088/0004-637X/707/2/L142.
- A. A. Abdo et al. A change in the optical polarization associated with a γ -ray flare in the blazar 3C279. *Nature*, 463:919–923, Feb. 2010. doi: 10.1038/nature08841.
- I. Agudo et al. Location of γ -ray Flare Emission in the Jet of the BL Lacertae Object OJ287 More than 14 pc from the Central Engine. *ApJ*, 726:L13, Jan. 2011. doi: 10.1088/2041-8205/726/1/L13.
- H. Akaike. A New Look at the Statistical Model Identification. *IEEE Trans. Autom. Control*, 19:716–723, 1974.
- K. Akiyama, R. Takahashi, M. Honma, T. Oyama, and H. Kobayashi. Multi-Epoch VERA Observations of Sagittarius A*. I. Images and Structural Variability. *PASJ*, 65:91, Aug. 2013. doi: 10.1093/pasj/65.4.91.
- P. Alexander and J. P. Leahy. Ageing and speeds in a representative sample of 21 classical double radio sources. *MNRAS*, 225:1–26, Mar. 1987. doi: 10.1093/mnras/225.1.1.
- R. Antonucci. Unified models for active galactic nuclei and quasars. *ARA&A*, 31:473–521, 1993. doi: 10.1146/annurev.aa.31.090193.002353.
- K. Asada and M. Nakamura. The Structure of the M87 Jet: A Transition from Parabolic to Conical Streamlines. *ApJ*, 745:L28, Feb. 2012. doi: 10.1088/2041-8205/745/2/L28.
- K. Asada, M. Inoue, Y. Uchida, S. Kameno, K. Fujisawa, S. Iguchi, and M. Mutoh. A Helical Magnetic Field in the Jet of 3C 273. *PASJ*, 54:L39–L43, June 2002. doi: 10.1093/pasj/54.3.L39.
- K. Asada, S. Kameno, Z.-Q. Shen, S. Horiuchi, D. C. Gabuzda, and M. Inoue. The Expanding Radio Lobe of 3C 84 Revealed by VSOP Observations. *PASJ*, 58:261–270, Apr. 2006. doi: 10.1093/pasj/58.2.261.
- K. Asada, M. Inoue, M. Nakamura, S. Kameno, and H. Nagai. Multifrequency Polarimetry of the NRAO 140 Jet: Possible Detection of a Helical Magnetic Field and Constraints on Its Pitch Angle. *ApJ*, 682:798–802, Aug. 2008. doi: 10.1086/588573.
- J. M. Bardeen and J. A. Petterson. The Lense-Thirring Effect and Accretion Disks around Kerr Black Holes. *ApJ*, 195:L65, Jan. 1975. doi: 10.1086/181711.
- B. M. Barker and G. G. Byrd. A method for determining the beam geometry of SS 433 using high-resolution radio observations. *ApJ*, 245:L67–L69, Apr. 1981. doi: 10.1086/183524.
- R. D. Blandford and A. Königl. Relativistic jets as compact radio sources. *ApJ*, 232:34–48, Aug. 1979. doi: 10.1086/157262.

- R. D. Blandford and M. J. Rees. A 'twin-exhaust' model for double radio sources. *MNRAS*, 169:395–415, Dec. 1974. doi: 10.1093/mnras/169.3.395.
- H. Boehringer, W. Voges, A. C. Fabian, A. C. Edge, and D. M. Neumann. A ROSAT HRI study of the interaction of the X-ray-emitting gas and radio lobes of NGC 1275. *MNRAS*, 264:L25–L28, Oct. 1993. doi: 10.1093/mnras/264.1.25L.
- A. H. Bridle and R. A. Perley. Extragalactic Radio Jets. *ARA&A*, 22:319–358, 1984. doi: 10.1146/annurev.aa.22.090184.001535.
- A. Caproni, H. J. Mosquera Cuesta, and Z. Abraham. Observational Evidence of Spin-induced Precession in Active Galactic Nuclei. *ApJ*, 616:L99–L102, Dec. 2004. doi: 10.1086/426863.
- C. L. Carilli, R. A. Perley, J. W. Dreher, and J. P. Leahy. Multifrequency radio observations of Cygnus A - Spectral aging in powerful radio galaxies. *ApJ*, 383:554–573, Dec. 1991. doi: 10.1086/170813.
- Y. Chikada, N. Kawaguchi, M. Inoue, M. Morimoto, H. Kobayashi, and S. Mattori. The VSOP Correlator. In H. Hirabayashi, M. Inoue, and H. Kobayashi, editors, *Frontiers of VLBI*, 1991.
- J. E. Conway. Compact symmetric objects—newborn radio galaxies? *NewA Rev.*, 46:263–271, May 2002. doi: 10.1016/S1387-6473(01)00191-9.
- L. Costamante and G. Ghisellini. TeV candidate BL Lac objects. *A&A*, 384:56–71, Mar. 2002. doi: 10.1051/0004-6361:20011749.
- V. Dhawan, K. I. Kellermann, and J. D. Romney. Kinematics of the Nucleus of NGC 1275 (3C 84). *ApJ*, 498:L111–L114, May 1998. doi: 10.1086/311313.
- R. J. H. Dunn, A. C. Fabian, and J. S. Sanders. Precession of the super-massive black hole in NGC 1275 (3C 84)? *MNRAS*, 366:758–766, Mar. 2006. doi: 10.1111/j.1365-2966.2005.09928.x.
- A. C. Fabian, J. S. Sanders, S. W. Allen, C. S. Crawford, K. Iwasawa, R. M. Johnstone, R. W. Schmidt, and G. B. Taylor. A deep Chandra observation of the Perseus cluster: shocks and ripples. *MNRAS*, 344:L43–L47, Sept. 2003. doi: 10.1046/j.1365-8711.2003.06902.x.
- A. C. Fabian, J. S. Sanders, G. B. Taylor, S. W. Allen, C. S. Crawford, R. M. Johnstone, and K. Iwasawa. A very deep Chandra observation of the Perseus cluster: shocks, ripples and conduction. *MNRAS*, 366:417–428, Feb. 2006. doi: 10.1111/j.1365-2966.2005.09896.x.
- D. Falceta-Gonçalves, A. Caproni, Z. Abraham, D. M. Teixeira, and E. M. de Gouveia Dal Pino. Precessing Jets and X-ray Bubbles from NGC 1275 (3C 84) in the Perseus Galaxy Cluster: A View from Three-dimensional Numerical Simulations. *ApJ*, 713:L74–L78, Apr. 2010. doi: 10.1088/2041-8205/713/1/L74.
- B. L. Fanaroff and J. M. Riley. The morphology of extragalactic radio sources of high and low luminosity. *MNRAS*, 167:31P–36P, May 1974.
- C. Fanti, R. Fanti, D. Dallacasa, R. T. Schilizzi, R. E. Spencer, and C. Stanghellini. Are compact steep-spectrum sources young? *A&A*, 302:317, Oct. 1995.
- D. C. Gabuzda, A. B. Pushkarev, and T. V. Cawthorne. Analysis of $\lambda=6\text{cm}$ VLBI polarization observations of a complete sample of northern BL Lacertae objects. *MNRAS*, 319:1109–1124, Dec. 2000. doi: 10.1046/j.1365-8711.2000.03932.x.
- G. L. Granato, G. De Zotti, L. Silva, A. Bressan, and L. Danese. A Physical Model for the Coevolution of QSOs and Their Spheroidal Hosts. *ApJ*, 600:580–594, Jan. 2004. doi: 10.1086/379875.
- K. Hada, A. Doi, M. Kino, H. Nagai, Y. Hagiwara, and N. Kawaguchi. An origin of the radio jet in M87

- at the location of the central black hole. *Nature*, 477:185–187, Sept. 2011. doi: 10.1038/nature10387.
- K. Hada, M. Kino, A. Doi, H. Nagai, M. Honma, Y. Hagiwara, M. Giroletti, G. Giovannini, and N. Kawaguchi. The Innermost Collimation Structure of the M87 Jet Down to ~ 10 Schwarzschild Radii. *ApJ*, 775:70, Sept. 2013. doi: 10.1088/0004-637X/775/1/70.
- J. A. Högbom. Aperture Synthesis with a Non-Regular Distribution of Interferometer Baselines. *A&AS*, 15:417, June 1974.
- D. C. Homan, R. Ojha, J. F. C. Wardle, D. H. Roberts, M. F. Aller, H. D. Aller, and P. A. Hughes. Parsec-Scale Blazar Monitoring: Proper Motions. *ApJ*, 549:840–861, Mar. 2001. doi: 10.1086/319466.
- V. Icke. Gas flow above an alpha disk. *AJ*, 85:329–347, Mar. 1980. doi: 10.1086/112678.
- S. Iguchi, T. Kkurayama, N. Kawaguchi, and K. Kawakami. Gigabit Digital Filter Bank: Digital Backend Subsystem in the VERA Data-Acquisition System. *PASJ*, 57:259–271, Feb. 2005. doi: 10.1093/pasj/57.1.259.
- S. G. Jorstad, A. P. Marscher, J. R. Mattox, A. E. Wehrle, S. D. Bloom, and A. V. Yurchenko. Multi-epoch Very Long Baseline Array Observations of EGRET-detected Quasars and BL Lacertae Objects: Superluminal Motion of Gamma-Ray Bright Blazars. *ApJS*, 134:181–240, June 2001. doi: 10.1086/320858.
- W. Junor, J. A. Biretta, and M. Livio. Formation of the radio jet in M87 at 100 Schwarzschild radii from the central black hole. *Nature*, 401:891–892, Oct. 1999. doi: 10.1038/44780.
- N. Kawakatu and M. Kino. On the dynamical evolution of hotspots in powerful radio-loud active galactic nuclei. *MNRAS*, 370:1513–1518, Aug. 2006. doi: 10.1111/j.1365-2966.2006.10574.x.
- N. Kawakatu, H. Nagai, and M. Kino. The Fate of Young Radio Galaxies: Decelerations Inside Host Galaxies? *ApJ*, 687:141–155, Nov. 2008. doi: 10.1086/591900.
- D. Kawata and B. K. Gibson. Self-regulated active galactic nuclei heating in elliptical galaxies. *MNRAS*, 358:L16–L20, Mar. 2005. doi: 10.1111/j.1745-3933.2005.00018.x.
- K. I. Kellermann, R. Sramek, M. Schmidt, D. B. Shaffer, and R. Green. VLA observations of objects in the Palomar Bright Quasar Survey. *AJ*, 98:1195–1207, Oct. 1989. doi: 10.1086/115207.
- A. King. Black Holes, Galaxy Formation, and the $M_{BH}-\sigma$ Relation. *ApJ*, 596:L27–L29, Oct. 2003. doi: 10.1086/379143.
- M. Kino and F. Takahara. Constraints on the energetics and plasma composition of relativistic jets in FR II sources. *MNRAS*, 349:336–346, Mar. 2004. doi: 10.1111/j.1365-2966.2004.07511.x.
- E. Komatsu et al. Five-Year Wilkinson Microwave Anisotropy Probe Observations: Cosmological Interpretation. *ApJS*, 180:330–376, Feb. 2009. doi: 10.1088/0067-0049/180/2/330.
- S. S. Komissarov, M. V. Barkov, N. Vlahakis, and A. Königl. Magnetic acceleration of relativistic active galactic nucleus jets. *MNRAS*, 380:51–70, Sept. 2007. doi: 10.1111/j.1365-2966.2007.12050.x.
- N. A. Kudryavtseva, S. Britzen, A. Witzel, E. Ros, M. Karouzos, M. F. Aller, H. D. Aller, H. Teräsranta, A. Eckart, and J. A. Zensus. A possible jet precession in the periodic quasar B0605-085. *A&A*, 526:A51, Feb. 2011. doi: 10.1051/0004-6361/201014968.
- R. A. Laing and A. H. Bridle. Rotation measure variation across M84. *MNRAS*, 228:557–571, Oct. 1987.
- M. L. Lister, M. H. Cohen, D. C. Homan, M. Kadler, K. I. Kellermann, Y. Y. Kovalev, E. Ros, T. Savolainen, and J. A. Zensus. MOJAVE: Monitoring of Jets in Active Galactic Nuclei with VLBA Experiments. VI. Kinematics Analysis of a Complete Sample of Blazar Jets. *AJ*, 138:1874–1892, Dec.

2009. doi: 10.1088/0004-6256/138/6/1874.
- A. P. Lobanov. Ultracompact jets in active galactic nuclei. *A&A*, 330:79–89, Feb. 1998.
- A. P. Lobanov and J. Roland. A supermassive binary black hole in the quasar 3C 345. *A&A*, 431: 831–846, Mar. 2005. doi: 10.1051/0004-6361:20041831.
- A. P. Lobanov and J. A. Zensus. A Cosmic Double Helix in the Archetypical Quasar 3C273. *Science*, 294:128–131, Oct. 2001. doi: 10.1126/science.1063239.
- N. R. Lomb. Least-squares frequency analysis of unequally spaced data. *Ap&SS*, 39:447–462, Feb. 1976. doi: 10.1007/BF00648343.
- A. P. Marscher et al. The inner jet of an active galactic nucleus as revealed by a radio-to- γ -ray outburst. *Nature*, 452:966–969, Apr. 2008. doi: 10.1038/nature06895.
- A. P. Marscher et al. Probing the Inner Jet of the Quasar PKS 1510-089 with Multi-Waveband Monitoring During Strong Gamma-Ray Activity. *ApJ*, 710:L126–L131, Feb. 2010. doi: 10.1088/2041-8205/710/2/L126.
- J. C. McKinney. General relativistic magnetohydrodynamic simulations of the jet formation and large-scale propagation from black hole accretion systems. *MNRAS*, 368:1561–1582, June 2006. doi: 10.1111/j.1365-2966.2006.10256.x.
- J. C. McKinney, A. Tchekhovskoy, and R. D. Blandford. Alignment of Magnetized Accretion Disks and Relativistic Jets with Spinning Black Holes. *Science*, 339:49–, Jan. 2013. doi: 10.1126/science.1230811.
- D. L. Meier, S. Koide, and Y. Uchida. Magnetohydrodynamic Production of Relativistic Jets. *Science*, 291:84–92, Jan. 2001. doi: 10.1126/science.291.5501.84.
- N. A. O. o. J. Mizusawa VLBI Observatory. VERA Status Report, 2011.
- N. Murray, E. Quataert, and T. A. Thompson. On the Maximum Luminosity of Galaxies and Their Central Black Holes: Feedback from Momentum-driven Winds. *ApJ*, 618:569–585, Jan. 2005. doi: 10.1086/426067.
- H. Nagai, M. Inoue, K. Asada, S. Kamenno, and A. Doi. The Kinematic and Spectral Ages of the Compact Radio Source CTD 93. *ApJ*, 648:148–157, Sept. 2006. doi: 10.1086/505793.
- H. Nagai, K. Asada, A. Doi, S. Kamenno, and M. Inoue. Kinematic and Synchrotron Ages of Compact Symmetric Objects. In T. A. Rector and D. S. De Young, editors, *Extragalactic Jets: Theory and Observation from Radio to Gamma Ray*, volume 386 of *Astronomical Society of the Pacific Conference Series*, page 290, June 2008.
- H. Nagai, K. Suzuki, K. Asada, M. Kino, S. Kamenno, A. Doi, M. Inoue, J. Kataoka, U. Bach, T. Hirota, N. Matsumoto, M. Honma, H. Kobayashi, and K. Fujisawa. VLBI Monitoring of 3C 84 (NGC 1275) in Early Phase of the 2005 Outburst. *PASJ*, 62:L11, Apr. 2010. doi: 10.1093/pasj/62.2.L11.
- H. Nagai, M. Orienti, M. Kino, K. Suzuki, G. Giovannini, A. Doi, K. Asada, M. Giroletti, J. Kataoka, F. D’Ammando, M. Inoue, A. Lähteenmäki, M. Tornikoski, J. León-Tavares, S. Kamenno, and U. Bach. VLBI and single-dish monitoring of 3C 84 for the period 2009–2011. *MNRAS*, 423:L122–L126, June 2012. doi: 10.1111/j.1745-3933.2012.01269.x.
- H. Nagai, M. Kino, K. Niinuma, K. Akiyama, K. Hada, S. Koyama, M. Orienti, K. Hiura, S. Sawada-Satoh, M. Honma, G. Giovannini, M. Giroletti, K. Shibata, and K. Sorai. The GENJI Programme: Gamma-Ray Emitting Notable AGN Monitoring by Japanese VLBI. *PASJ*, 65:24, Apr. 2013.
- H. Nagai, T. Haga, G. Giovannini, A. Doi, M. Orienti, F. D’Ammando, M. Kino, M. Nakamura, K. Asada,

- K. Hada, and M. Giroletti. Limb-brightened Jet of 3C 84 Revealed by the 43 GHz Very-Long-Baseline-Array Observation. *ApJ*, 785:53, Apr. 2014. doi: 10.1088/0004-637X/785/1/53.
- M. L. Norman, K.-H. A. Winkler, L. Smarr, and M. D. Smith. Structure and dynamics of supersonic jets. *A&A*, 113:285–302, Sept. 1982.
- R. Ojha, M. Kadler, M. Böck, R. Booth, M. S. Dutka, P. G. Edwards, A. L. Fey, L. Fuhrmann, R. A. Gaume, H. Hase, S. Horiuchi, D. L. Jauncey, K. J. Johnston, U. Katz, M. Lister, J. E. J. Lovell, C. Müller, C. Plötz, J. F. H. Quick, E. Ros, G. B. Taylor, D. J. Thompson, S. J. Tingay, G. Tosti, A. K. Tzioumis, J. Wilms, and J. A. Zensus. TANAMI: tracking active galactic nuclei with austral milliarcsecond interferometry . I. First-epoch 8.4 GHz images. *A&A*, 519:A45, Sept. 2010. doi: 10.1051/0004-6361/200912724.
- T. Okamoto, R. S. Nemmen, and R. G. Bower. The impact of radio feedback from active galactic nuclei in cosmological simulations: formation of disc galaxies. *MNRAS*, 385:161–180, Mar. 2008. doi: 10.1111/j.1365-2966.2008.12883.x.
- M. Orienti, D. Dallacasa, and C. Stanghellini. Constraining the nature of high frequency peakers. The spectral variability. *A&A*, 475:813–820, Dec. 2007. doi: 10.1051/0004-6361:20078105.
- D. E. Osterbrock. Seyfert galaxies with weak broad H alpha emission lines. *ApJ*, 249:462–470, Oct. 1981. doi: 10.1086/159306.
- I. Owsianik, J. E. Conway, and A. G. Polatidis. Renewed Radio Activity of Age 370 years in the Extragalactic Source 0108+388. *A&A*, 336:L37–L40, Aug. 1998.
- A. G. Pacholczyk. *Radio astrophysics. Nonthermal processes in galactic and extragalactic sources*. 1970.
- A. Pedlar, H. S. Ghataure, R. D. Davies, B. A. Harrison, R. Perley, P. C. Crane, and S. W. Unger. The Radio Structure of NGC1275. *MNRAS*, 246:477, Oct. 1990.
- A. Petrosian, B. McLean, R. J. Allen, and J. W. MacKenty. Markarian Galaxies. I. The Optical Database and Atlas. *ApJS*, 170:33–70, May 2007. doi: 10.1086/511333.
- L. Petrov, M. Honma, and S. M. Shibata. The KCAL VERA 22 GHz Calibrator Survey. *AJ*, 143:35, Feb. 2012. doi: 10.1088/0004-6256/143/2/35.
- R. L. Plambeck, G. C. Bower, R. Rao, D. P. Marrone, S. G. Jorstad, A. P. Marscher, S. S. Doeleman, V. L. Fish, and M. D. Johnson. Probing the Parsec-scale Accretion Flow of 3C 84 with Millimeter Wavelength Polarimetry. *ApJ*, 797:66, Dec. 2014. doi: 10.1088/0004-637X/797/1/66.
- A. Polatidis, P. N. Wilkinson, W. Xu, A. C. S. Readhead, T. J. Pearson, G. B. Taylor, and R. C. Vermeulen. Compact Symmetric Objects in a complete flux density limited sample. *NewA Rev.*, 43: 657–661, Nov. 1999. doi: 10.1016/S1387-6473(99)00073-1.
- A. G. Polatidis and J. E. Conway. Proper Motions in Compact Symmetric Objects. *PASA*, 20:69–74, 2003. doi: 10.1071/AS02053.
- A. C. S. Readhead, G. B. Taylor, T. J. Pearson, and P. N. Wilkinson. Compact Symmetric Objects and the Evolution of Powerful Extragalactic Radio Sources. *ApJ*, 460:634, Apr. 1996a. doi: 10.1086/176997.
- A. C. S. Readhead, G. B. Taylor, W. Xu, T. J. Pearson, P. N. Wilkinson, and A. G. Polatidis. The Statistics and Ages of Compact Symmetric Objects. *ApJ*, 460:612, Apr. 1996b. doi: 10.1086/176996.
- J. D. Scargle. Studies in astronomical time series analysis. II - Statistical aspects of spectral analysis of unevenly spaced data. *ApJ*, 263:835–853, Dec. 1982. doi: 10.1086/160554.

- L. Scheck, M. A. Aloy, J. M. Martí, J. L. Gómez, and E. Müller. Does the plasma composition affect the long-term evolution of relativistic jets? *MNRAS*, 331:615–634, Apr. 2002. doi: 10.1046/j.1365-8711.2002.05210.x.
- P. A. G. Scheuer. Models of extragalactic radio sources with a continuous energy supply from a central object. *MNRAS*, 166:513–528, Mar. 1974. doi: 10.1093/mnras/166.3.513.
- P. A. G. Scheuer and R. Feiler. The realignment of a black hole misaligned with its accretion disc. *MNRAS*, 282:291, Sept. 1996.
- M. Schmidt and R. F. Green. Quasar evolution derived from the Palomar bright quasar survey and other complete quasar surveys. *ApJ*, 269:352–374, June 1983. doi: 10.1086/161048.
- M. C. Shepherd, T. J. Pearson, and G. B. Taylor. DIFMAP: an interactive program for synthesis imaging. In *Bulletin of the American Astronomical Society*, volume 26 of *Bulletin of the American Astronomical Society*, pages 987–989, May 1994.
- A. Sillanpää, S. Haarala, M. J. Valtonen, B. Sundelius, and G. G. Byrd. OJ 287 - Binary pair of supermassive black holes. *ApJ*, 325:628–634, Feb. 1988. doi: 10.1086/166033.
- I. A. G. Snellen. GPS and CSS radio sources and space-VLBI. *ArXiv e-prints*, Feb. 2008.
- K. Suzuki, H. Nagai, M. Kino, J. Kataoka, K. Asada, A. Doi, M. Inoue, M. Orienti, G. Giovannini, M. Giroletti, A. Lähteenmäki, M. Tornikoski, J. León-Tavares, U. Bach, S. Kamenon, and H. Kobayashi. Exploring the Central Sub-parsec Region of the γ -Ray Bright Radio Galaxy 3C 84 with VLBA at 43 GHz in the Period of 2002-2008. *ApJ*, 746:140, Feb. 2012. doi: 10.1088/0004-637X/746/2/140.
- F. Tavecchio and G. Ghisellini. On the spine-layer scenario for the very high-energy emission of NGC 1275. *MNRAS*, 443:1224–1230, Sept. 2014. doi: 10.1093/mnras/stu1196.
- G. B. Taylor, J. M. Marr, T. J. Pearson, and A. C. S. Readhead. Kinematic Age Estimates for Four Compact Symmetric Objects from the Pearson-Readhead Survey. *ApJ*, 541:112–119, Sept. 2000. doi: 10.1086/309428.
- G. B. Taylor, N. E. Gugliucci, A. C. Fabian, J. S. Sanders, G. Gentile, and S. W. Allen. Magnetic fields in the centre of the Perseus cluster. *MNRAS*, 368:1500–1506, June 2006. doi: 10.1111/j.1365-2966.2006.10244.x.
- Y. Uchida and K. Shibata. Magnetodynamical acceleration of CO and optical bipolar flows from the region of star formation. *PASJ*, 37:515–535, 1985.
- C. M. Urry and P. Padovani. Unified Schemes for Radio-Loud Active Galactic Nuclei. *PASP*, 107:803, Sept. 1995. doi: 10.1086/133630.
- M. J. Valtonen, K. Nilsson, A. Sillanpää, L. O. Takalo, H. J. Lehto, W. C. Keel, S. Haque, D. Cornwall, and A. Mattingly. The 2005 November Outburst in OJ 287 and the Binary Black Hole Model. *ApJ*, 643:L9–L12, May 2006. doi: 10.1086/505039.
- R. C. Vermeulen, A. C. S. Readhead, and D. C. Backer. Discovery of a nuclear counterjet in NGC 1275: A new way to probe the parsec-scale environment. *ApJ*, 430:L41–L44, July 1994. doi: 10.1086/187433.
- R. C. Walker, J. D. Romney, and J. M. Benson. Detection of a VLBI counterjet in NGC 1275: A possible probe of the parsec-scale accretion region. *ApJ*, 430:L45–L48, July 1994. doi: 10.1086/187434.
- R. C. Walker, V. Dhawan, J. D. Romney, K. I. Kellermann, and R. C. Vermeulen. VLBA Absorption Imaging of Ionized Gas Associated with the Accretion Disk in NGC 1275. *ApJ*, 530:233–244, Feb. 2000. doi: 10.1086/308372.

P. N. Wilkinson, A. G. Polatidis, A. C. S. Readhead, W. Xu, and T. J. Pearson. Two-sided ejection in powerful radio sources: The compact symmetric objects. *ApJ*, 432:L87–L90, Sept. 1994. doi: 10.1086/187518.

R. J. Wilman, A. C. Edge, and R. M. Johnstone. The nature of the molecular gas system in the core of NGC 1275. *MNRAS*, 359:755–764, May 2005. doi: 10.1111/j.1365-2966.2005.08956.x.